Transverse phase space studies with the new CDS booster cavity at PITZ

Dissertation
zur Erlangung des Doktorgrades
des Departments Physik
der Universität Hamburg

vorgelegt von
Grygorii Vashchenko
aus Lugansk

Hamburg
2013

Gutachter der Dissertation: Prof. Dr. Jörg Roßbach
Dr. Ralph Aßmann

Gutachter der Disputation: Prof. Dr. Jörg Roßbach
PD Dr. Bernhard Schmidt

Datum der Disputation: 30.09.2013

Vorsitzende/Vorsitzender
des Prüfungsausschusses: Prof. Dr. Michael A. Rübhausen

Vorsitzende/Vorsitzender
des Promotionsausschusses: Prof. Dr. Peter Hauschildt

Leiter/Leiterin des Departaments Physik: Prof. Dr. Daniela Pfannkuche

Dekan der Fakultat für Mathematik,
Informatik und Naturwissenschaften: Prof. Dr. Heinrich Graener

Abstract

Light is one of the main tools for the investigation of natural phenomena. Light produced with the help of synchrotron machines serves to investigate many phenomena in natural sciences for many years. However the synchrotron light has a limited degree of spatial coherence, restriction on the minimum achievable pulse duration at the level of about 30 ps and not sufficient brilliance to perform a lot of experiments. With the invention of free electron lasers (FELs) new opportunities are opened as the light produced by the free electron lasers is spatially coherent, the pulse duration of the produced light can be in the order of 10 fs and below and the brilliance is much higher compared to synchrotron light. To produce high quality laser light with a short wavelength free electron lasers like the European XFEL and FLASH require electron beams with a high charge and low transverse emittance. The photo injector test facility at DESY, Zeuthen site, was built with the aim to develop and characterize electron sources for future usage at FLASH and the European XFEL. The emittance of the produced electron beam plays a key role as it influences the final brilliance and the minimum achievable wavelength of the produced laser light.

This work is devoted to investigations of the emittance of electron beams with different charges. The emittance of the electron beam depends on many machine parameters such as UV laser pulse shape and its size, solenoid focusing current and accelerating cavities settings. Methodical studies of the emittance dependencies on these parameters were done in simulations using a particle tracking code as well as experimentally.

Zusammenfassung

Licht ist eines der wichtigsten Werkzeuge zur Untersuchung von Naturphänomenen, von denen im Laufe der Jahre viele mit Licht untersucht wurden, das mit Hilfe eines Synchrotrons erzeugt wurde. Synchrotronlicht hat aber nur eine begrenzte räumliche Kohärenz, was die minimale Pulsdauer auf etwa 30 ps begrenzt und dazu führt, dass die maximal erreichbare Brillanz nicht ausreichend ist für eine Reihe von Experimenten. Mit der Erfindung des Freie Elektronen Lasers (FEL) wurden neue Forschungsmöglichkeiten eröffnet, da das von einem FEL erzeugte Licht eine Pulsdauer von etwa 10 fs oder weniger haben kann mit einer Brillanz, die viel höher ist als das von Synchrotronlicht. Um Laserlicht mit kurzen Wellenlängen und hoher Qualität mit einem Freie Elektronen Laser, wie dem European XFEL oder FLASH zu produzieren, werden Elektronenstrahlen mit hohen Ladungen und kleiner transversaler Emittanz benötigt. Der Photoinjektor Teststand bei DESY, Standort Zeuthen wurde aufgebaut mit dem Ziel Elektronenquellen für zukünftige Anwendungen bei FLASH und dem European XFEL zu entwickeln und zu charakterisieren. Die Emittanz der produzierten Elektronen spielt dabei eine Schlüsselrolle, da sie die zu erzielende Brillanz und minimal erreichbare Wellenlünge des produzierten Laserlichts entscheidend beeinflusst. Diese Arbeit behandelt Untersuchungen der Emittanz eines Elektronenstrahls mit verschiedenen Ladungen. Die Emittanz eines Elektronenstrahls hängt von vielen Maschinenparametern ab, z.B. der Form und Größe des UV Laser Pulses, des Fokussierstroms des Solenoiden und den Einstellungen der Beschleunigerkavitäten. Methodische Studien der Abhängigkeit der Emittanz von diesen Parametern wurden in Simulationen mit einem Teilchenstrahlverfolgungsprogramm als auch experimentell durchgeführt.

Supporting traditions, to my dear family, Nikita and Maryna

Contents

Chapter 1

Introduction

Many natural sciences are using the light of different wavelengths to investigate the phenomena of nature. In the range from the ultraviolet down to hard X-ray wavelengths great progress in natural sciences was achieved with using the light produced by electrons or positrons moving in circular accelerators via synchrotron radiation. However, the synchrotron radiation has a limited degree of spatial coherence and the typical pulse duration is not shorter than 30 ps. The brilliance of the radiation produced in circular machines is also not sufficient for a lot of experiments which can shine light on different phenomena of nature. These constraints led to investigations for obtaining coherent light sources with better magnitudes of the parameters mentioned above.

Free electron lasers (FELs) currently are the most powerful tool for producing brilliant coherent light in a wide range of a wavelengths from infrared to X-rays. The basic principles of the FEL were proposed by J. Madey in 1971 in terms of his PhD thesis at Stanford University [1]. In conventional laser systems the electrons bounded to the nuclei irradiate light at a given wavelength defined by the energy difference between atomic orbits. The FELs are based on the idea that the radiating electrons not necessary have to be bound to a nuclei. In 1976 Madey and his coworkers demonstrated first experiments with FEL radiation using an electron beam with an energy of 24 MeV and a 5 meter long undulator for amplifying the radiation. The power of this laser was only about 300 mW with an efficiency of 0.01 % [1]. This proof-of-principle work induced the development of the free electron lasers all over the world.

The free electron lasers can be divided in two groups: low-gain FELs and high-gain FELs. The low-gain FELs require an optical resonator like a conventional laser systems. That is why the minimum achievable wavelength for this kind of FELs is limited by the possibility to create mirrors for the given wavelength. The high-gain FELs use a single pass of the electrons through an undulator.

Nowadays there are several major high-gain FEL facilities in the world producing laser light in the hard X-ray region: the Linac Coherent Light Source (LCLS) at the SLAC National Accelerator Laboratory which can produce laser pulses with less than 10 fs pulse duration, wavelength down to 1.2 Å, 120 Hz repetition rate, 9 GW peak power and brilliance of about 10^{32} photons/s/mm^2/mrad^2/0.1%BW [2]; the SPring-8 Angstrom Compact free electron LAser (SACLA) produces laser pulses with less than 30 fs pulse duration, wavelength down to 0.6 Å, 10 Hz repetition rate, 10 GW peak power and brilliance of about 10^{30} photons/s/mm^2/mrad^2/0.1%BW [3]; Free electron LASer in Hamburg (FLASH) produces laser pulses with less than 70 fs pulse duration, wavelength down to 4.2 nm, 1 MHz repetition rate at 3 GW peak power and brilliance of about 10^{31} photons/s/mm^2/mrad^2/0.1%BW. Compared to the SACLA and LCLS facilities which are single shot machines, FLASH can produce laser pulse trains within 700 μs long RF pulses. In such a way up to 7000 laser pulses per second can be produced.

A new international research infrastructure, the European X-Ray Free-Electron Laser (XFEL) has the aim to generate extremely brilliant (peak brilliance $\sim 5 \cdot 10^{33}$ photons/s/mm^2/mrad^2/0.1%BW) and ultra-short (< 100 fs) pulses of spatially coherent X-rays with wavelengths down to 0.1 nm. The properties of European XFEL beams (coherence, ultra high brilliance and pulsed structure) and the development of appropriate detectors and instrumentation will allow completely new experiments. From this innovative user facility new fundamental results are expected in materials research, chemistry, biology and physics.

The short pulse durations of the produced laser radiation is important as atoms in molecules and solids oscillate around the equilibrium state with typical times of some hundreds femtoseconds. Using a coherent light with a high brilliance a diffraction pattern of not only crystals but also of large macromolecules, viruses or cells can be recorded in order to reconstruct their structure. The short duration of the produced laser light opens the possibility to perform pump-and-probe experiments in which for example conventional laser pulses (pump) are used to trigger chemical reactions and delayed to them FEL pulses (probe) are used to record the information about the evolution of the chemical reaction.

An electron beam passing through a dipole magnet is deflected and emits light under the influence of the Lorentz force:

$$\vec{F} = q_e(\vec{E} + \vec{v} \times \vec{B}), \tag{1.1}$$

where q_e is an elementary charge carried by the electron, $\vec{E}$ and $\vec{B}$ are the electric and magnetic fields acting on the electron moving with a speed of $\vec{v}$. In the bending magnets of storage rings when the electrons pass through the bending magnet they usually radiate independently and therefore produce incoherent radiation. The obtained continuous energy spectrum starts from zero and ends beyond the critical energy E_c defined by the following equation [4]:

$$E_c = \frac{3\hbar c \gamma^3}{2R}, \tag{1.2}$$

where R is the curvature radius in the bending magnet, ħ is the reduced Planck constant, c is the speed of light in vacuum and γ is the Lorentz factor defined as:

$$\gamma = \frac{1}{\sqrt{1 - v^2/c^2}}. \tag{1.3}$$

Most of the power radiated during this process is situated inside a cone with an opening angle of $1/\gamma$. For the energies above the critical energy the synchrotron radiation emission is negligible.

As it was mentioned there are two main components required to produce coherent radiation in high-gain FELs: a high quality electron beam and an undulator. The undulator consists of numerous dipole magnets with an alternating polarity periodically arranged along the electron beam direction. The electron passing through the undulator performs a sinusoidal motion under the influence of the Lorentz force Eq. 1.1. The total deflection angle of the electron beam at the exit of the undulator is zero. A schematic layout of a planar undulator with a passing electron beam is presented in Fig. 1.1

To produce coherent radiation by passing through the undulator, the radiating part of the electron beam must be shorter than the radiation wavelength. In FELs this is possible because of a self organization process of the electrons in the beam at the level of the radiation wavelength during its movement along the undulator. This process named microbunching is based on the following principle: the electrons in the beam losing energy for the radiation field move on sinusoidal trajectories with larger amplitudes than

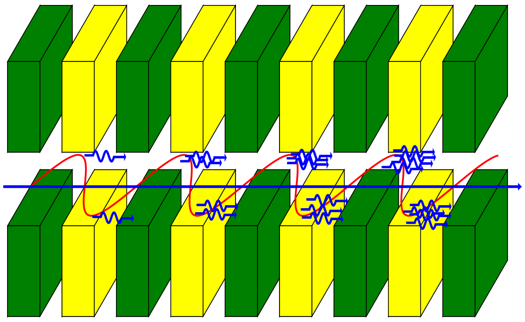

Figure 1.1: Schematic view of a planar undulator. The electron beam performs a sinusoidal motion along the undulator axis and emits photons. Yellow and green boxes are permanent magnets with alternating polarity. Red curve is an electron beam trajectory. Blue line is an undulator axis. Numerous blue waves are a light emitted by the electron beam.

electrons gaining energy from the radiation field. This leads to a modulation of the longitudinal velocity of the electrons inside the bunch and consequently to a concentration of the electrons in spatial slices shorter than the radiation wavelength. The electrons in such a microbunch radiate as a single particle with a charge of $\mathrm{N_e^{mb} q_e}$, where $\mathrm{N_e^{mb}}$ is an amount of electrons in a microbunch. In such conditions, compared to the incoherent radiation process in which the radiation power is proportional to the amount of the electrons $\mathrm{P_\gamma \sim N_e}$, the radiation power is proportional to the amount of the electrons squared $\mathrm{P_\gamma \sim (N_e^{mb})^2}$.

The strong radiation field created by the microbunches enhances the microbunching further and leads to an exponential growth of the radiated power. The traveling length in the undulator which the electron beam has to pass to increase the energy of the emitted FEL radiation by a factor of e is named FEL power gain length $\mathrm{L_g}$ and the radiation power can be written as $\mathrm{P(z) = P_0 e^{L_g/z}}$. The power gain length can be estimated by the following formula [5]:

$$L_g \simeq 2.26 \sqrt{\frac{\gamma^5 I_A}{K^2 B_n \left(1+K^2\right)}}, \tag{1.4}$$

where $\mathrm{I_A}$ is the Alfven current ($\mathrm{I_A}$ = 17kA for electrons) and $\mathrm{B_n}$ is the brightness of the electron beam defined as:

$$B_n = \frac{2 I_p}{\varepsilon_n^2}, \tag{1.5}$$

where $\mathrm{I_p}$ is the peak current of the electron beam and ε_n is the normalized transverse projected emittance of the electron beam (see more in Chapters 3, 4) and K is so-called undulator parameter defined as:

$$K = \frac{q_e B_0 \lambda_u^e}{2\pi m_e}, \tag{1.6}$$

where $\mathrm{m_e}$ is an electron rest mass, $\lambda_\mathrm{u}^\mathrm{e}$ is a period of the magnets arrangement in the undulator and B_0 is the peak magnetic field on the undulator axis. For the planar undulator the peak magnetic field is described as:

$$B_0 = B_m / cosh\left(\pi g_u / \lambda_u\right), \tag{1.7}$$

where $\mathrm{B_m}$ is the magnetic flux density in the middle of the pole face and $\mathrm{g_u}$ is the undulator gap height.

The exponential growth of the radiation power is limited by the decrease of the electron beam energy in the undulator due to the radiation. Moreover, the energy of the radiation can be pumped back to the electron beam. This leads to the oscillation of the FEL radiation power around its maximum mean value after a finite amount of FEL gain lengths passed by the electron beam in the undulator [4]. Summarizing, the evolution of the electron beam in the undulator can be considered as a three-step process: microbunching formation starting from shot noise, exponential growth of the FEL power, saturation regime. An example of the power gain dependence on the position in the undulator for typical FLASH conditions representing all the three processes is presented in Fig. 1.2 [4].

The radiation obtained from an undulator consists of narrow spectral lines and is situated in a narrow cone along the undulator axis. In first order consideration, assuming $\lambda_\mathrm{u}^\mathrm{l}$ as the undulator period in the laboratory system, the undulator period in the coordinate system of the electron beam moving close to the speed of light c can be estimated as $\lambda_\mathrm{u}^\mathrm{e} = \lambda_\mathrm{u}^\mathrm{l}/\gamma$ taking into account the Lorentz length contraction. As well the oscillation frequency in this system is defined as $\omega = 2\pi\mathrm{c}/\lambda_\mathrm{u}^\mathrm{e}$. For an observer located in the laboratory system the radiation wavelength is strongly shortened by the relativistic Doppler effect $\lambda_\gamma^\mathrm{l} \approx \lambda_\mathrm{u}^\mathrm{l}/2\gamma^2$. In second order consideration, taking into account the sinusoidal trajectory of the electron beam, the following formula describing the radiation wavelength can be found [4]:

$$\lambda_\gamma^l = \frac{\lambda_u^l}{2\gamma^2}\left(1 + \frac{K^2}{2}\right). \tag{1.8}$$

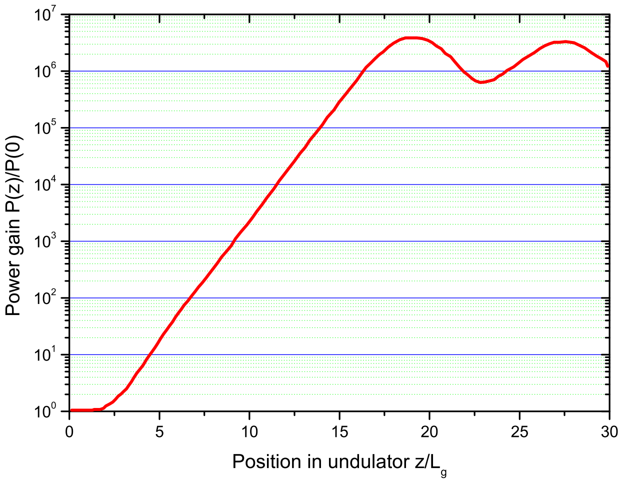

Figure 1.2: FEL power dependence on the position in the planar undulator for FLASH parameters.

From this equation it is seen that the wavelength of the undulator radiation can be varied by changing either the electron beam energy or the undulator gap height. The advantage of changing the undulator's gap height is that in this case one does not need to tune the accelerator optics upstream the undulator like in the case when the electron beam energy is changed. But often the radiation wavelength is changed by tuning the beam energy as it is technically hard to change the gap height of the undulator with the required precision. There is a fundamental limitation on the minimum achievable wavelength from the lasing process in FELs. In an one-dimensional approximation, operation of the FEL can be described in terms of the gain parameter Γ, space-charge parameter $\widehat{\Lambda}_p^2$, longitudinal velocity spread parameter $\widehat{\Lambda}_T^2$ and the efficiency parameter ρ (see [5] for more details). Detailed analysis of the influence of these parameters on the FEL lasing process shows that $\widehat{\Lambda}_T^2$ has the strongest impact. Defining the safety margin of the FEL operation by the condition that the relative loss in the field gain due to the spread of longitudinal velocities is less than 10% of the value at $\widehat{\Lambda}_T^2 = 0$ we can obtain the following relation defining the minimum achievable wavelength [5]:

$$\lambda^r_{min} \approx 18\pi\varepsilon_n\sigma_E\sqrt{\frac{\gamma I_A}{I_p}\frac{1+K^2}{K^2}}, \tag{1.9}$$

where σ_{E} is the relative energy spread of the electron beam.

As it can be seen from this relation there are three main parameters influencing the minimum achievable wavelength from the lasing process in FELs: electron beam energy spread, normalized transverse emittance of the electron beam and peak current of the electron beam. The minimum normalized transverse emittance of the electron beam which can be achieved at the entrance to the undulator is a property which is already defined at the injector and cannot be improved afterwards. That is why it is extremely important to optimize it already at the source.

The goal of this thesis is a systematical study of the transverse phase spaces of the electron beam in order to optimize its transverse emittance with a type of gun cavity which is used at FLASH and will be used at the future European XFEL facilities. In Chapter 2 the Photo Injector Test facility at DESY, Zeuthen Site (PITZ) setup, where the experimental investigations were performed, is introduced. One of the first emittance measurements was performed at PITZ in 2003. At that time RF photo gun was operated at on-axis peak fields of about 45 MV/m which is 15 MV/m less than currently used. In addition, no second accelerating structure was available. The measured emittance for the electron beams with a charge of 1 nC was about $1.5 - 1.7$ mm mrad [6]. Emittance dependencies on such machine parameters like gun launching phase, main and bucking solenoid currents were investigated. First measurements of the emittance for the electron beams with other charges were performed as well (see [6] for details). Later, in 2004-2005, the PITZ setup was upgraded with the new 10 MW multibeam klystron which allows to increase on-axis peak field in the gun up to 60 MV/m [7] and emittance decrease was expected (emittance dependence on gun on-axis peak field can be found, for example, in Chapter 6.2.1). Additionally, the second accelerating structure - TESLA type booster [7] - was installed. This cavity had the same geometry as TESLA type cavities used at FLASH and future European XFEL, but was made out of copper for normal conducting operation. The second acceleration structure plays a role in emittance compensation as well as in emittance conservation along the beamline which is necessary for electron beam characterization with different diagnostic devices. A number of measurements were performed yielding the emittance values of about 1.3 mm mrad for the electron beams with a charge of 1 nC. In addition to previous setup, emittance dependence on the booster accelerating gradient was obtained, some basic uncertainties and systematic errors in the emittance estimation were calculated, evaluation of the so-called core emittance was performed [8].

Compared to the previous PITZ setup the major difference is improvement of the low level RF regulation for the gun (see Chapter 2.2) and exchange of the second accelerating structure from TESLA to CDS type. This new booster cavity has significantly improved field distribution stability, better water cooling capacity which allows to operate at longer RF pulses and higher average accelerating gradients having a positive effect on the emittance conservation. In the following Chapter 3 the electron beam dynamics in the photo injector starting from the photoelectric effect is described. Additionally, different sources of the emittance growth are considered. In particular it is shown that the model previously used for the estimation of the emittance growth caused by the RF effects, see for example [8, 9], is not applicable for PITZ gun. The emittance measurement method together with a detailed description of the corresponding hardware which was used in the frame of this work are presented in Chapter 4. Possible systematic errors estimations from different sources are discussed in Chapter 5, in particular emittance overestimation due to the deviation of the machine parameters from their optimum values first time calculated in the frame of this work. The detailed simulations of the electron beam dynamics at PITZ are presented in Chapter 6. These simulations include a methodical studies of the emittance dependencies on a most sensitive machine parameters for electron beams with various charges. Comparison of the simulation results obtained with CDS and TESLA type booster cavities is performed as well. This is followed in Chapter 7 by the presentation of the experimentally measured emittance data for different electron beam charges. Significant emittance reduction was measured compared to the previous PITZ setups [6, 8]. Comparison of the measured emittance data to the simulation results is done as well as the comparison to the emittance measured with the TESLA type cavity. The work ends with a conclusions and outlook presented in Chapter 8.

Chapter 2

Overview of the PITZ facility

The Photo Injector Test facility at DESY, Zeuthen Site (PITZ) has the aim to develop and optimize high brightness electron sources for free electron lasers like FLASH and the European XFEL. The main goal at PITZ is the production of electron beams of 1 nC bunch charge with a normalized transverse projected emittance at the injector output of less than 0.9 mm mrad.

All the major components of the PITZ facility, such as the photocathode laser system, gun and booster cavities and their power sources, including regulation and diagnostic systems, are continuously improved and investigated. In the following sections the facility setup, which was used for emittance simulations and measurements presented in this thesis, is be described.

2.1 Photocathode laser system

The PITZ photocathode laser system consists of an unique UV laser developed and built by the Max Born Institute (MBI) [10], a laser imaging beamline delivering the UV beam to the photocathode and various diagnostic devices. As the laser used at PITZ is a prototype for the XFEL it has to fulfill the requirements of the XFEL photocathode laser system. The laser system must be able to produce pulse trains with up to 600 μs length and a repetition rate of 4.5 MHz of the laser pulses within the train. The pulse trains repetition rate is 10 Hz which gives average laser pulses frequency of about $3 \cdot 10^4$ Hz. Currently 1 MHz repetition rate of the bunches in the 650 μs long train is realized at PITZ. As the laser pulses will be used to produce photoelectrons from a Cs_2Te cathode, the laser wavelength must be in the

UV region. Currently, the wavelength of the laser which is used at PITZ is about 258 nm.

The UV laser beam distribution with some distortions due to a mirror charge and a space-charge translates to the electron beam. The electron beam emittance strongly depends on the transverse and temporal laser shapes, therefore the UV beam properties required to obtain the best electron beam characteristics must be fulfilled. As it was shown in simulations [11], to obtain the best emittance of the electron beam at the XFEL conditions, an UV laser beam with uniform transverse distribution and flat-top temporal distribution with Full Width at Half Maximum (FWHM) of about 20 ps and as short as possible rise and fall times must be used. The laser system used at PITZ is able to provide longitudinally flat-top laser pulses with FWHM up to 25 ps and rise/fall times of about 2 ps.

2.1.1 UV laser

A simplified schematic layout of the UV laser is presented in Fig. 2.1. At first, infrared (wavelength $\lambda \approx 1030$ nm) laser pulses with a FWHM of about 2 ps and Gaussian temporal shape are produced by the pulse train oscillator (PTO). Two different kinds of PTO were used during the experiments preformed in the run period 2011. The PTO based on the Yb:KGW crystal was replaced in April 2011 with a new one based on the Yb:YAG crystal.

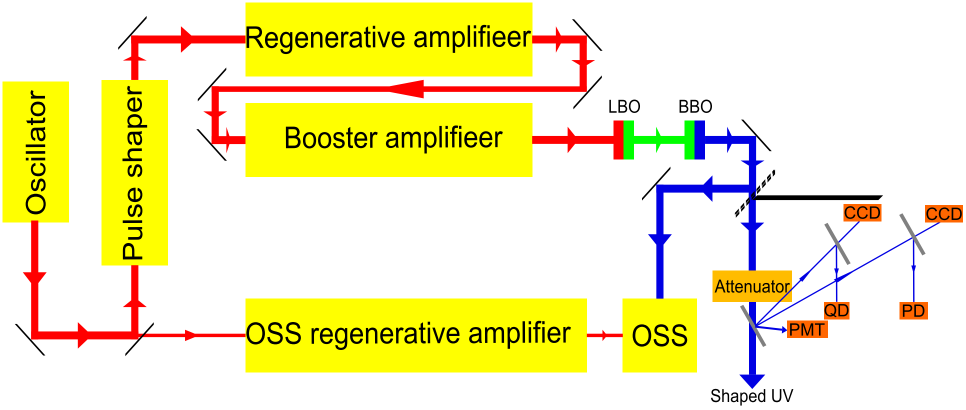

Figure 2.1: Schematic layout of the PITZ UV laser. Colored arrows - laser beam path: red - 1030 nm, green - 515 nm, blue - 258 nm.

The new oscillator brought better intensity and pointing stability of the produced laser beam. The energy of the produced pulses from the Yb:YAG PTO is approximately 0.2 nJ. The laser oscillator is synchronized to the master oscillator which provides the time triggering for the whole PITZ facility.

Formation of the flat-top temporal distribution (see Fig. 2.2) from the Gaussian pulse is done with the help of the pulse shaper, consisting of two polarizers and 13 birefringent crystals. At the entrance of the pulse shaper the incoming laser pulse is split into two pulses identical in all properties except their polarization. Passing through the birefringent crystals laser pulses are split once more and obtaining time delays [12]. In such a way a number of relatively delayed laser pulses are formed. At the output of the pulse shaper the second polarizer is used to equalize the polarization of the produced Gaussian pulses. After leaving the pulse shaper the laser beam passes through the regenerative amplifier and leaves it with an energy of about 2 μJ. The booster amplifiers increase the energy of the pulses further up to 10 μJ.

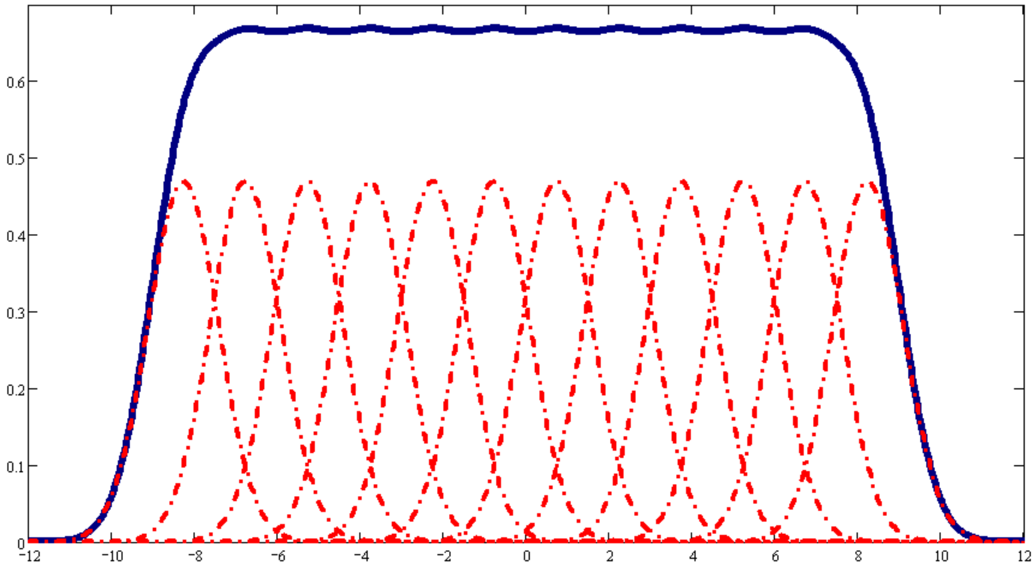

Figure 2.2: Scheme of producing a flat-top laser pulse from Gaussian pulses delayed to each other.

The final stage in the formation of the laser beam with the desired properties is the conversion of the infrared laser pulses with a wavelength of

1030 nm to UV laser pulses with a wavelength of 258 nm. In this two step procedure the laser beam with a wavelength of 1030 nm at first passes the LBO (Lithium triborate) crystal halving its wavelength. In the second step, the BBO (Beta-Barium Borate) crystal is halving the wavelength of the beam once more. In such a way UV laser pulses with a wavelength of about 258 nm are produced. Passing the conversion crystals the energy of the laser pulses reduces and the final UV pulses have an energy of about 1.5 μJ.

The produced laser beam is transported further to the accelerator tunnel and to different diagnostic systems like the Optical Sampling System (OSS) and a Hamamatsu C5680 streak camera [13] which allow to measure the longitudinal beam profile, CCD cameras for transverse profile measurements, a quadrant diode (QD) for beam position stability measurements, a photomultiplier (PMT) and a calibrated photodiode (PD) for energy measurements.

The OSS placed on the laser table is based on the cross-correlation of the final UV pulse with infrared Gaussian pulses produced by the laser oscillator and shortened with the help of an optical fiber. The probe infrared pulses are used for a temporal scan of the UV beam by changing subsequently the relative timing between a comb of UV pulses and a comb of IR pulses. The difference frequency generation [14] is used to produce UV pulses with a wavelength of about 343 nm, intensities of which will reproduce the temporal shape of the main UV pulses. The resolution of this system was estimated to be at the level of about 1 ps. Another way to measure the temporal shape of the produced UV beam is using the streak camera which has worse time resolution (more than 2 ps [15]) and is more difficult in use.

2.1.2 Laser beam transport system

The UV laser beam is transported to the tunnel with the help of an imaging system containing several mirrors and lenses. In the tunnel, the laser beam passes through a Beam Shaping Aperture (BSA) which determines its transverse beam size. In the frame of this work two different kinds of apertures were used during the experimental emittance studies. The simple and more robust one was a metal plate with drilled holes of different diameter. The disadvantage of this aperture plate is that only some predefined laser beam sizes can be chosen. If one needs another laser beam size an additional plate with a hole of the corresponding diameter has to be produced. Another disadvantage is that when the diameter of the laser beam needs to be changed the whole aperture plate has to be moved. As the properties of the electron beam produced at the photocathode strongly depend on the position of the laser on the photocathode, it must be checked that the laser beam position at the cathode is kept the same after moving the plate to the position of another hole. This checking procedure named Beam Based Alignment (BBA) is relatively time consuming (about 2-3 hours). The second kind of aperture is an aperture with a variable diameter. The diameter of this aperture can be chosen in a wide range of values with good precision. As only the diameter of the aperture is changed, the laser beam position is kept the same on the photocathode during this procedure. A disadvantage of this kind of aperture, since it consists of multiple leafs, is that the edges of the beam are distorted, especially for the small diameters.

Finally, the transversely and temporally shaped UV beam is transported to the cathode and different diagnostics as it is shown in Fig. 2.3. The mirrors M5 and M6 are remotely controllable and are used to adjust the laser beam position on the in-vacuum mirror and on the cathode by changing their orientation with respect to the laser beam. To measure the laser transverse shape expected on the photocathode, the CCD camera named Virtual Cathode 2 (VC2) is installed at the equivalent position. A quadrant diode (QD), a photomultiplier (PMT) and an energy meter (EM) are used in the same meaning as described in Chapter 2.1.1. A PCO camera is used to monitor the transverse profile. This intensified CCD camera is capable to measure the single laser pulse inside a pulse train. In such a way the dependence of the laser pulse transverse shape on its position inside the pulse train can be investigated [9]. In addition several achromatic lenses are used at different positions along the laser beamline to focus the laser beam.

2.2 Gun section

The PITZ gun section consists of an 1.6-cell L-band RF gun cavity operated at about 60 MV/m maximum accelerating gradient at the cathode and main and bucking solenoids surrounding it as it is shown in Fig. 2.4. A 10 MW multi-beam klystron with two power outputs from Thales [16] was used to get such high accelerating gradients. Later it was replaced with a 10 MW Toshiba E3736 multi-beam klystron which has better reliability [17]. The RF power is delivered further with the help of waveguides filled with SF_6. To compensate phase differences in the waveguides a phase shifter is installed in one of the waveguides. Finally, the RF power reaches the in-vacuum T-

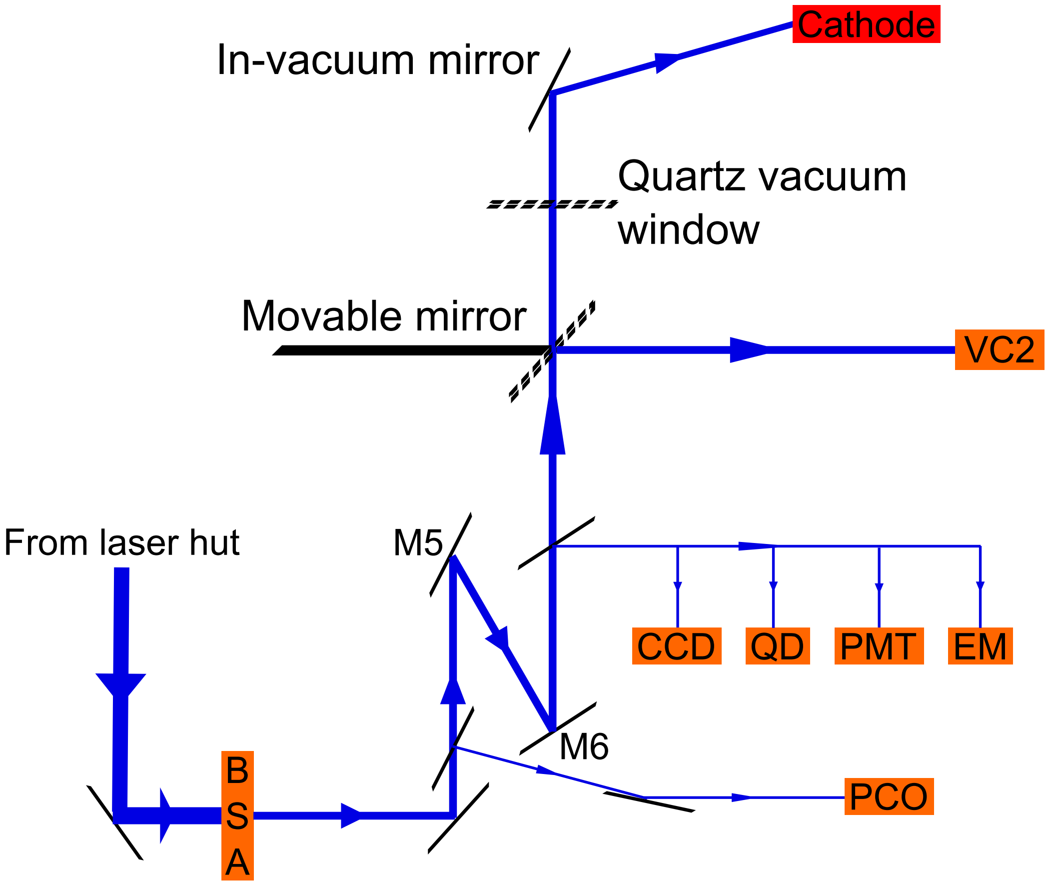

Figure 2.3: Schematic layout of the PITZ laser beamline.

combiner which merges these two waves into one. On each arm in the front of the T-Combiner 5 MW directional couplers are installed. Additionally, between the T-Combiner and the gun input a 10 MW in-vacuum directional coupler is installed. All of them are used for the control of the incoming RF power by analyzing forward and reflected wave signals. Until spring 2010 PITZ was equipped only with the two 5 MW couplers. The disadvantage of such setup was that the forward and reflected waves could not be measured precisely because of the cross-talk between the waveguides through the T-combiner. Therefore, no efficient RF feedback regulation system could be realized. This led to fairly high phase jitter and unstable phase and power along the RF pulse. Since spring 2010 the 10 MW in-vacuum directional coupler is installed. Installation of this coupler gave the possibility of direct

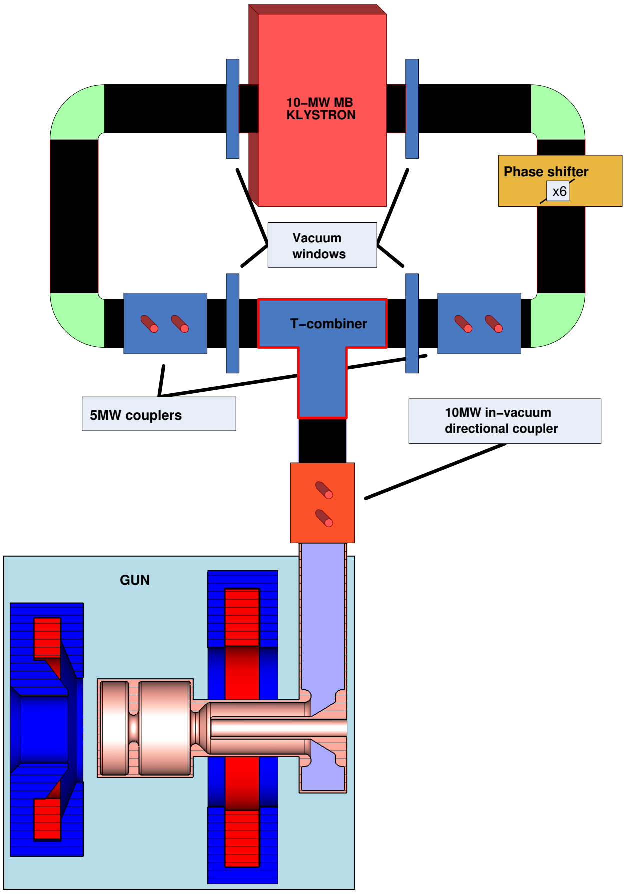

Figure 2.4: Schematic layout of the PITZ gun section.

measurements of the forward and reflected waves from the gun. A feedback loop regulating the klystron parameters based on the data obtained from the 10 MW in-vacuum directional coupler was realized [18]. For the first time this system gave the possibility to correct the phase and power slope along the RF pulse. Another improvement brought by this system is the reduced pulse to pulse phase jitter: from about $2-2.5$ deg rms without the feedback down to $0.2-0.3$ deg rms with feedback switched on. As the main operation of the gun is done around the maximum mean momentum gain phase, the region with a strong dependence of extracted charge on gun launching phase, the beam quality was improved significantly [19].

Cs_2Te semiconductor cathodes are used at PITZ to produce the photoelectrons. The photocathode is inserted in the gun from the back side with the help of a special in-vacuum cathode exchange system which consists of two actuators and a cathode box with several photocathodes [20].

The electric fields of the gun and the CDS booster (see Chapter 2.3) cavities together with the superimposed magnetic fields of the main and bucking solenoids are shown in Fig. 2.5. The main solenoid is located at 0.276 m downstream the cathode and is used for the beam focusing and emittance compensation. As the main solenoid field is not equal to zero at the cathode, an additional bucking solenoid located behind the gun cavity and with opposite polarity to the main solenoid is used. Using of this additional solenoid is necessary to avoid any initial angular momentum of the electrons emitted from the photocathode. Superposition of the fields of the main and bucking solenoid gives zero magnetic field at the cathode. The main gun parameters are presented in Table 2.1.

Parameter	**Value**	**Unit**
Operating frequency	1300	MHz
Maximum accelerating gradient E_0	≈ 60.0	MV/m
Maximum momentum gain	≈ 7	MeV/c
Maximal RF pulse power	≈ 7	MW
Maximal RF pulse length	700	μs
Usual repetition rate	10	Hz
Aperture diameter (cell/iris/exit)	180/50/33.5	mm
Number of cells	1.6	
Q-factor	20472	
Operating temperature	≈ 78	°C
Residual gas pressure	$< 10^{-9}$	mbar

Table 2.1: PITZ gun parameters.

2.3 CDS Booster cavity

After leaving the gun the electron beam accelerated up to ≈ 7 MeV/c reaches the second accelerating cavity. Further acceleration of the electron beam is mandatory to conserve the beam emittance. The normal conducting 14 cell L-band CDS (Cut Disk Structure, see Fig. 2.6) booster cavity is installed at PITZ since July 2010 and replaced the 9 cell normal conducting copper

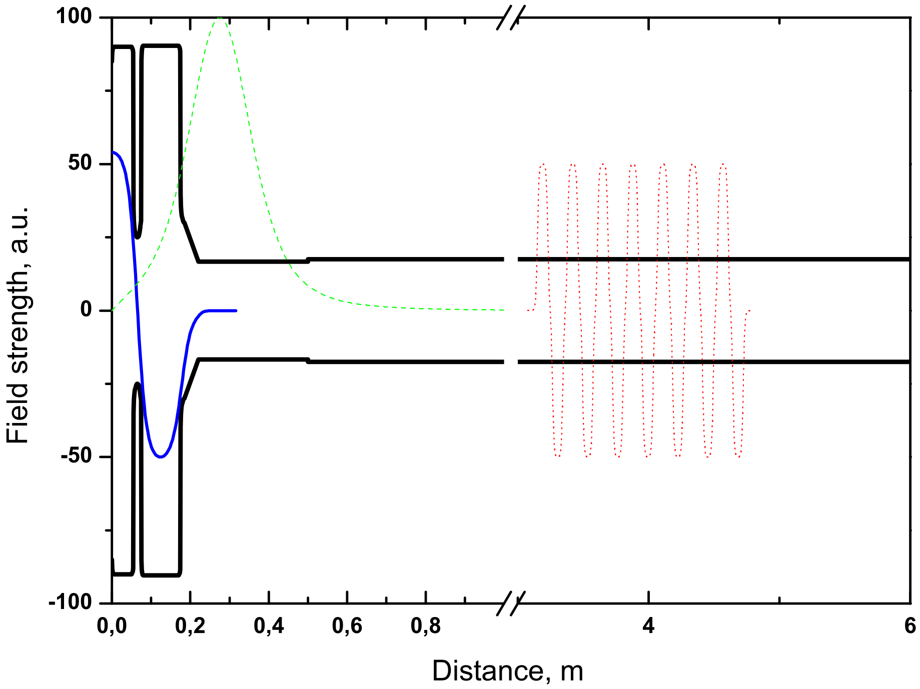

Figure 2.5: Fields distribution along the PITZ beamline. The black line shows the aperture borders, the blue line is the gun electric field distribution, the green dashed line is the superimposed magnetic field distribution of the main and bucking solenoids, and the red dotted line shows the booster electric field distribution.

L-band TESLA type booster cavity. The 3-D model of the CDS cavity is shown in Fig. 2.7. This multi-cell cavity is based on a compensated accelerating structure with improved coupling coefficient value. The new cavity has significantly improved field distribution stability, better water cooling capacity which allows to operate at longer RF pulses (up to 900 μs, compared to 100 μs for the TESLA type cavity) and higher average accelerating gradients. In addition, the CDS booster cavity is equipped with field probes. This gives the possibility to realize a feedback loop using direct field measurements inside the cavity. The maximum electron beam momentum after booster acceleration is about 28 MeV/c. The cavity parameters are presented in Table 2.2.

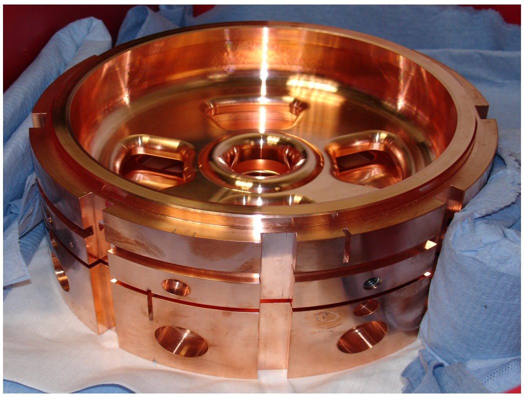

Figure 2.6: Single Cut Disk Structure cell.

Parameter	**Value**	**Unit**
Operating frequency	1300	MHz
Maximum accelerating gradient E_0	14.0	MV/m
Nominal energy gain	20.18	MeV/c
Maximal RF pulse power	8.6	MW
Maximal RF pulse length	900	μs
Usual repetition rate	10	Hz
Aperture diameter	30.0	mm
Number of cells	14	
Q-factor	20100	
Operating temperature	44	°C
Residual gas pressure	$< 10^{-7}$	mbar

Table 2.2: CDS booster parameters.

2.4 Diagnostics

A schematic view of the PITZ diagnostics is shown in Fig. 2.8. The PITZ beamline contains a lot of diagnostic devices used for the electron beam characterization which includes the measurements of different parameters such as beam charge, beam transverse and longitudinal distributions at different locations etc. In the following sections different diagnostics devices are described in more detail.

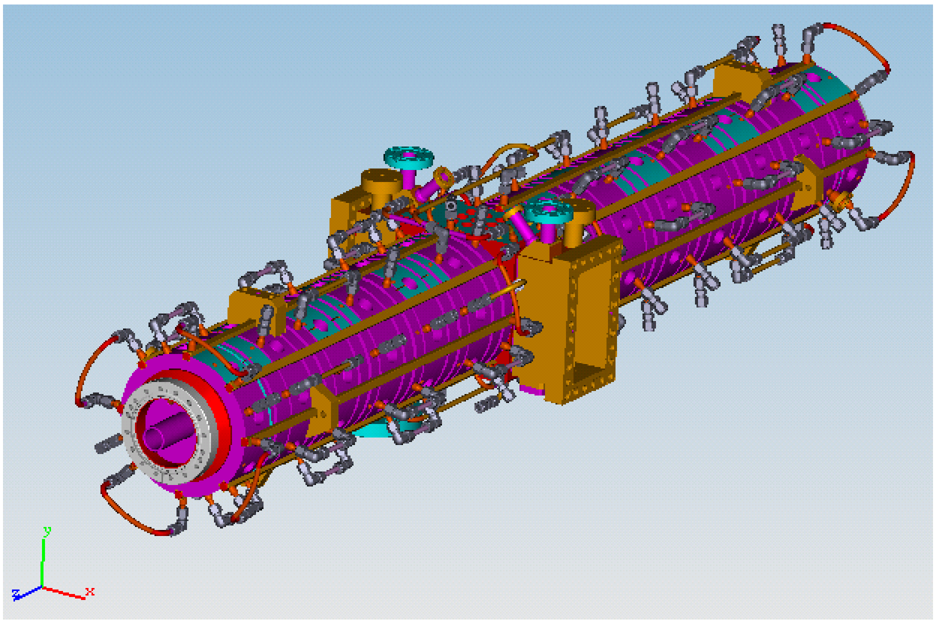

Figure 2.7: 3D model of the CDS booster cavity.

2.4.1 Charge measurement

There are two kinds of devices used at PITZ to measure the beam charge - integrated current transformers (ICT) and Faraday cups. The major difference between them is that the ICTs are non-destructive diagnostics devices contrary to the Faraday cups. The PITZ beamline has 4 ICTs installed at different places which were produced and calibrated by Bergoz [21]. All of them have approximately the same calibration factor equal to 0.8 nC/nVs. The ICTs used at PITZ can reliably measure beam charges from 100 pC upwards and are especially tuned for 1 nC charge measurements. For lower charges home-made Faraday cups are used. A Faraday cup is a metal cup designed to collect all the electrons hitting it when it is inserted in the beamline. The produced current is proportional to the number of impinging electrons and can be measured with an oscilloscope. The measured signal is translated into a charge with a calibration factor of 0.02 nC/nVs. Compared to the ICTs, Faraday cups can measure charges down to fractions of fC.

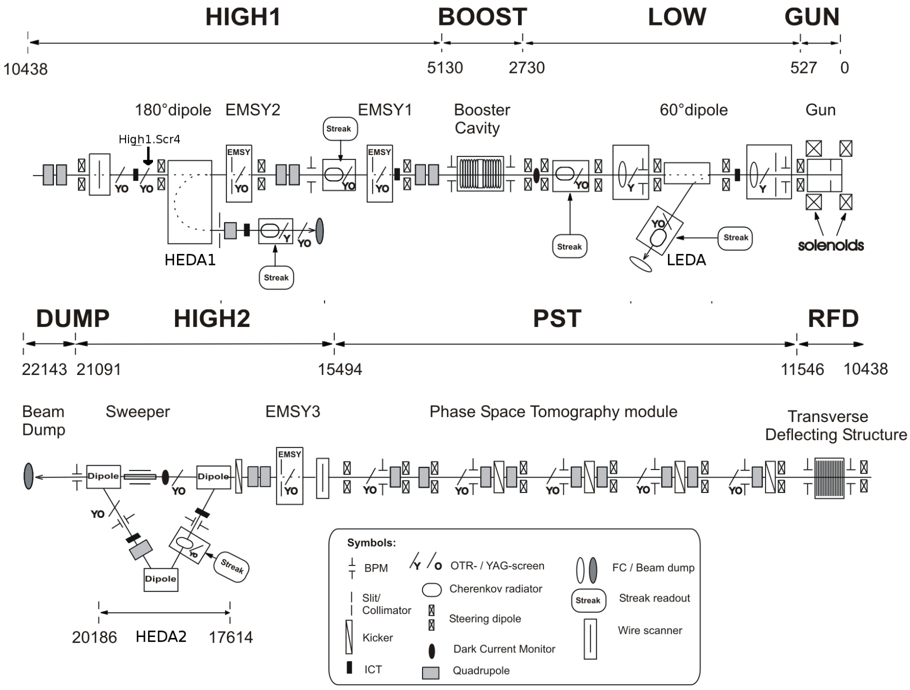

Figure 2.8: Schematic layout of the PITZ facility including gun and booster cavities and available diagnostics.

2.4.2 Momentum distribution measurement

For measuring the longitudinal momentum distribution of the electron beam three magnetic spectrometers are used at PITZ. One is installed between the gun and the CDS booster (LEDA in Fig. 2.8) and gives the possibility to measure the momentum distribution after the gun acceleration. Another one is installed downstream the CDS booster (HEDA1 in Fig. 2.8), and in addition to the momentum distribution measurements it can be used for slice emittance studies [22]. The third one was recently installed at the end of the beamline (HEDA2 in Fig. 2.8) and will be used for high resolution beam momentum measurements, longitudinal phase space measurements with a slice momentum spread down to 1 keV/c and, in combination with a transverse deflecting cavity, for transverse slice emittance measurements [23]. The electron beam passing through a dipole is deflected under the influence of the Lorentz force (Eq. 1.1). The deflection angle θ which determines the trajectory of the electrons is inversely proportional to the beam momentum $\mathrm{p_z}$:

$$p_z = \frac{q_e \cdot B \cdot L_{eff}}{\theta \cdot c}, \tag{2.1}$$

where B is the dipole magnetic field, $\mathrm{L_{eff}}$ is the effective length of the dipole. The dispersed beam distribution is monitored by a scintillating screen and captured by a CCD camera and represents the momentum distribution of the electron beam.

2.4.3 Temporal distribution and longitudinal phase space measurement

The temporal distribution of the beam as well as the longitudinal phase space have been measured with a streak camera [13] up to now. The beam interacting with an OTR screen or with a Cherenkov radiator installed in the straight section creates a visible light distribution equivalent to the longitudinal distribution of the electron beam. This light is transmitted to the streak camera in which the temporal distribution is measured with a resolution of about 2 ps [15]. The longitudinal phase space is measured in the same manner using an OTR screen or Cherenkov radiator installed in the dispersive sections. In these measurements the light distribution in the dispersive direction is imaged onto the entrance slit of the streak camera so, that the temporal sweep of the streak camera generates the longitudinal phase space distribution.

2.4.4 Transverse distribution and transverse phase space measurement

The transverse distribution of the electron beam can be measured at many different positions using an observation screen and a camera. Two different types of screens are used at PITZ. At first, scintillating YAG:Ce powder screens which produce broadband light in the visible spectrum. The intensity of the produced light is proportional to the amount of electrons hitting the screen and their energy. Another type of screen is an OTR (Optical Transition Radiation) screen. The optical transition radiation is produced by relativistic electrons when they pass through the boundary of two media with different dielectric constants [24].

The transverse phase space of the electron beam produced at PITZ can be measured with various methods. The tomographic reconstruction technique based on the reconstruction of a multidimensional function from its projections is used at PITZ since 2010. The electron beam imaged on the observation screen gives a two-dimensional spatial projection of the six-dimensional phase space. A number of such projections is collected at different positions along the beamline. The reconstruction quality depends on the amount of projections. Currently four projections are used at PITZ to reconstruct the transverse phase space of the electron beam. The key point of the tomographic reconstruction used at PITZ is that the beta-functions of the electron beam at the positions, where projections are taken, are the same. This is achieved with the help of FODO cells which are installed between the several observation screens. Consequently, the phase advance between the observation screens is fixed. The tomographic reconstruction technique gives the possibility to reconstruct the X and the Y transverse phase spaces simultaneously. In addition, this method is sensitive for low bunch charges when using short bunch trains or even individual pulses [25].

Another way to measure the transverse phase space distribution is the well established slit scan technique. Three Emittance Measurement Systems (EMSY) are used for this kind of measurement and are installed along the PITZ beamline [8]. An EMSY consists of two orthogonal actuators driven by stepper motors and two rotational stepper motors. Position set precision of the orthogonal actuators is $5\,\mu$m and 0.01 deg for the rotational stages. Each of the actuators contains two slit masks with 10 and $50\,\mu$m openings, and one observation screen. The slit mask opening is made of two tungsten plates of 1 mm thickness along the beam direction. At one of the actuators a YAG powder screen is installed and on the other an OTR screen. Two rotational stepper motors are used to maximize the angular acceptance of the slits with respect to the electron beam direction. The local divergence of the beam is estimated by cutting the electron beam into thin slices and measuring their transverse distribution after the propagation in a drift space. By knowing the position of the slit corresponding to the captured beamlet the transverse phase space of the electron beam can be reconstructed. More details about EMSY design and slit scan emittance measurement technique used at PITZ can be found in Chapter 4 and [8].

Chapter 3

Electron beam dynamics in the photo injector

In this chapter the electron beam dynamics in the photo injector starting from the electron emission from the cathode surface is described with a special focus on its transverse projected emittance. An introduction to the emittance, acceleration and focusing processes is given. Several sources of emittance growth in the photo injector, like RF-induced emittance and space-charge induced emittance are considered for the PITZ setup.

3.1 Photoelectric effect

The electron beam dynamics in the photo injector starts with the formation of the electron beam based on the photoelectric effect. In the photoelectric effect electrons disposed in liquids, gases or solids gaining energy from the light may be emitted. In the accelerator technologies metal and semiconductor cathodes are widely used to produce electron beams. An advantage of the metal cathodes (for example copper) is that they may be operated at worse vacuum level than semiconductor cathodes. On the other hand, the quantum efficiency of the metal cathodes is usually several orders of magnitude lower than quantum efficiency of semiconductor cathodes. As it was mentioned in Chapter 2.1, Cs_2Te semiconductor cathodes are used at PITZ to produce the electron beam. The UV laser produces a light with a wavelength of 258 nm which corresponds to a photon energy of about 4.81 eV and illuminates the cathode surface. According to the three-step emission model of Spicer [26–

28], electron which absorbs this energy leaves its binding environment and starts to drift to one of the maxima of the density states in the conduction band of Cs_2Te. The first maximum of the density states is located at 4.05 eV as shown in Fig. 3.1. Electrons located at this energy state may escape the photocathode disposing a part of their energy for penetrating the band gap with a width of 3.3 eV and the surface potential barrier with a width of 0.2 eV. In such a way the electrons leave the photocathode with a mean kinetic energy of $E_k = (4.05 - 3.3 - 0.2)\,\mathrm{eV} = 0.55\,\mathrm{eV}$ [29]. As the response time of the Cs_2Te is short, the ensemble of the emitted photoelectrons has about the same spatial and temporal distributions as the laser beam pulse. When the density of the extracted charge is high enough the space-charge forces modify the beam distributions.

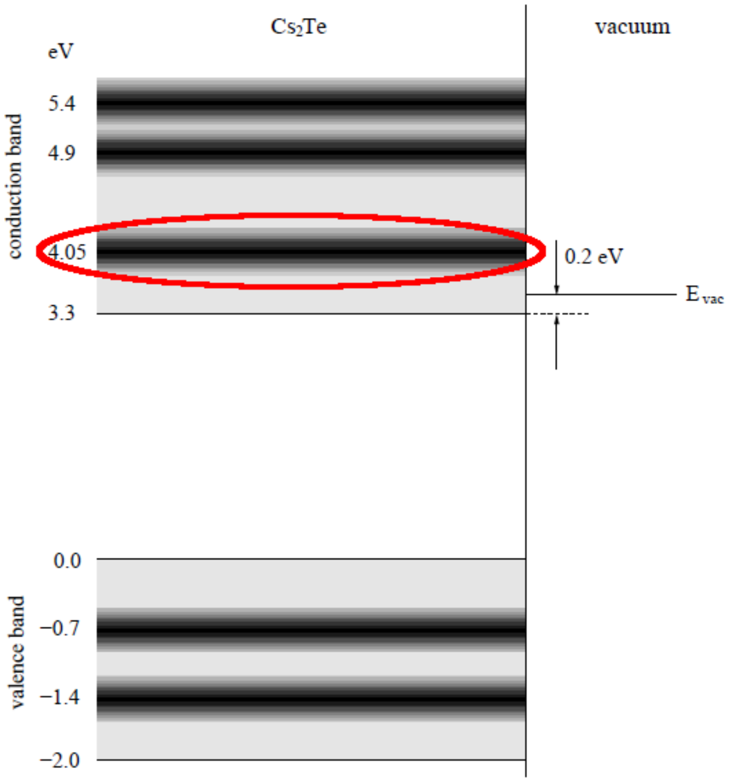

Figure 3.1: Schematic structure of the energy levels of Cs_2Te according to Powell [29]. The maxima of density of states are shown in black, see text.

3.2 Phase space and emittance

As it was mentioned in the previous section, the photoelectrons extracted from the cathode have a certain mean energy and energy spread. In other words, each electron is emitted from the cathode with a different magnitude and direction of the velocity vector. This intrinsic thermal velocity spread stays present at any position of the electron beam downstream the cathode. The emittance provides a figure of merit to describe the quality of the electron (or any other kind of) beam. The transverse projected emittance is related to the projection of the volume occupied by the electron ensemble in a six-dimensional phase space defined by a set of canonical coordinates $\mathrm{q_i}, \mathrm{p_i}$. The evolution of the physical system after time t depends only on its state at this time. The equation of motion described in the Hamiltonian form can be written as follows:

$$\begin{cases} \dot{q}_i = \partial H/\partial p_i \\ \dot{p}_i = -\partial H/\partial q_i \end{cases} \tag{3.1}$$

where q_i and p_i are the coordinates and conjugate momenta of the particle, respectively and the Hamiltonian $H = H(q_i, p_i, t)$ represents the total energy of the system and in case of a closed system $H = T + U$, where T and U are kinetic and potential energies of the system, respectively. The phase space of the system is the space in which all possible states of the system are represented. The phase space of the electron beam can be described with all its possible values of coordinates and conjugate momenta. Often the longitudinal motion along the beam axis can be decoupled from the transverse motion. Therefore one can split the 6-dimensional phase space into a 2-dimensional longitudinal phase space (z, p_z) and a 4-dimensional transverse phase space (x, y, p_x, p_y). Often also the transverse motion can be decomposed into two independent motions along two orthogonal transverse directions which leads to decoupling of the 4-dimensional transverse phase space to two 2-dimensional phase spaces (x, p_x), (y, p_y). As the measurement of the transverse components of the momenta is not practical, it is convenient to switch to the so-called trace spaces (x, x'), (y, y') where the x', y' are the divergences of the beam in corresponding directions and are defined as $x' = dx/dz = p_x/p_z$ and $y' = dy/dz = p_y/p_z$.

The geometric emittance can be defined as an area A occupied by the beam in the trace space divided by π, e.g. for (x, x') we obtain $\varepsilon_g = A_x/\pi$ [30]. The disadvantage of such a definition is that it does not take into account the distortions of the trace space produced by nonlinear forces. This may be illustrated by the following example: let's take the trace space in which the divergence at any coordinate is given by the following equation: $x' = Cx^n$. Then the trace spaces will be represented as a line of zero width in case of $n = 1$ and some curved line (of zero width as well) for higher orders as shown in Fig. 3.2a and Fig. 3.2b. As one can see the areas, and therefore a geometric emittance, occupied by both trace spaces are zero. In such a way the geometric emittance cannot describe the difference of the beam quality in such cases. Another, more comprehensive example of trace spaces having the same area and therefore the same value of geometric emittance is shown in Fig. 3.2c and Fig. 3.2d. Again the geometric emittance definition cannot distinguish the difference between the trace spaces. Therefore a more reliable emittance definition is necessary. This leads to introduction of the rms emittance. To compare the quality of beams with arbitrary distribution Lapostolle and Sacherer have introduced the rms emittance and the concept of equivalent beams [31,32] where two different beams of the same species and having the same current and kinetic energy are considered to be equivalent if the second moments of their distributions are the same. Considering the discrete distribution of the particles in two-dimensional trace space (x, x') the second moments are defined by the following equations:

$$\begin{aligned}
\langle x^2 \rangle &= \frac{1}{N}\sum_{i=1}^{N} x_i^2 - \left(\frac{1}{N}\sum_{i=1}^{N} x_i\right)^2 \\
\langle x'^2 \rangle &= \frac{1}{N}\sum_{i=1}^{N} x'^2_i - \left(\frac{1}{N}\sum_{i=1}^{N} x'_i\right)^2 \\
\langle xx' \rangle &= \frac{1}{N}\sum_{i=1}^{N} \left(x_i - \frac{1}{N}\sum_{i=1}^{N} x_i\right)\left(x'_i - \frac{1}{N}\sum_{i=1}^{N} x'_i\right) \qquad (3.2)
\end{aligned}$$

The total or 100% rms emittance is then defined as:

$$\varepsilon_x = \sqrt{\langle x^2 \rangle \langle x'^2 \rangle - \langle xx' \rangle^2} \qquad (3.3)$$

and the normalized one as:

$$\varepsilon_{n,x} = \beta\gamma\sqrt{\langle x^2 \rangle \langle x'^2 \rangle - \langle xx' \rangle^2}. \qquad (3.4)$$

Applying the rms emittance definition for the distributions presented in Fig. 3.2a and Fig. 3.2b one can find that the rms emittance is still zero for

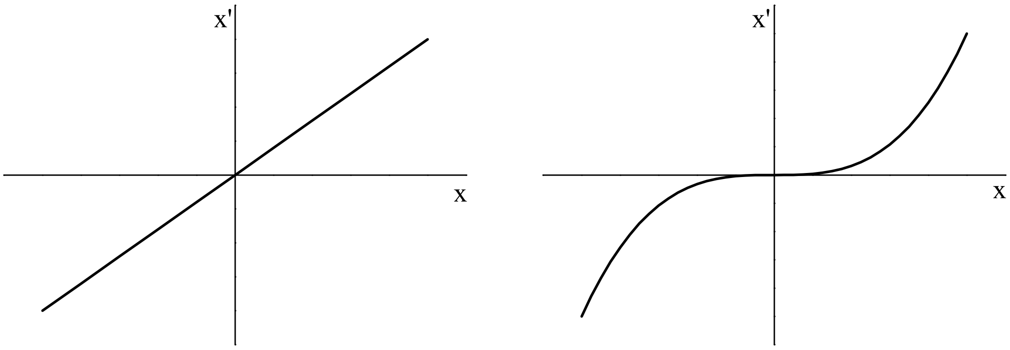

(a) Example of ideal trace space for a case $x' = Cx^n$, n=1.

(b) Example of ideal trace space for a case $x' = Cx^n$, n=3.

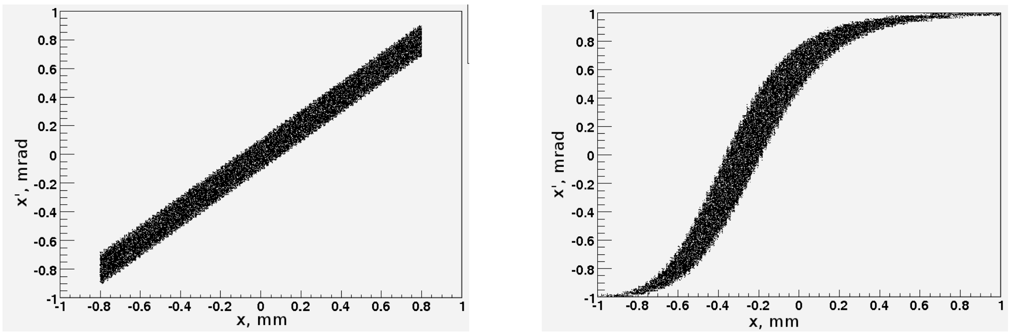

(c) Example of linear trace space distribution.

(d) Example of nonlinear trace space distribution.

Figure 3.2: Two examples of trace spaces occupying the same area (Fig. 3.2a and Fig. 3.2b; Fig. 3.2c and Fig. 3.2d) and correspondingly having the same geometric emittance ε_g. Different properties of the trace spaces in each pair can be taken into account applying the rms emittance definition, see text.

the case $n = 1$ but for the case $n = 3$ it is in general not zero. For the second example presented in Fig. 3.2c and Fig. 3.2d emittance values according to the new definition are different as well. As one can see the emittance described by Eq. 3.3 depends on the energy of the beam. To compare qualities of the beams with different energies the normalized emittance introduced by Eq. 3.4 has to be used. A slit scan technique was used during the experiments in order to measure the rms normalized emittance of the electron beam. The details of the slit scan procedure and emittance calculation procedures are presented in Chapter 4.

3.3 Beam focusing, acceleration and emittance growth

An ensemble of particles forms a beam if their longitudinal momentum component is much larger than the transverse momentum components. Leaving the surface of the photocathode, the electrons ensemble is accelerated in the RF gun cavity. The pair of solenoids shown in Fig. 2.4 is used at PITZ to focus the electron beam. The focusing of the electron beam in the axisymmetric solenoid field follows from the Busch theorem which states about the conservation of the canonical angular momentum in such fields [30]. The particles entering the solenoid field start to rotate with a Larmor frequency, the centrifugal force is half of the Lorentz force and there is a net focusing force towards the solenoid axis. In addition to the focusing, the solenoid helps with the compensation of emittance growth due to linear space-charge forces as described in [33].

The electric field in the RF cavity along the Z axis in the simple case may be described by the following equation:

$$E_z = E_0 \cos{(kz)} \sin{(\omega t + \phi_0)}, \tag{3.5}$$

where $\mathrm{E_0}$ is the maximum on-axis peak field, $\mathrm{k} = 2\pi/\lambda_{\mathrm{RF}}$, with the RF wavelength λ_{RF}, is the wave number, $\omega = \mathrm{ck}$ is the RF field frequency and ϕ_0 is the RF field phase at the time when the electron leaves the cathode surface: $\mathrm{z} = 0$ and $\mathrm{t} = 0$. As we can notice, Eq. 3.5 describes the field in the RF cavity operated in π-mode. The equation of motion can then be written in the following form [34]:

$$\frac{d\gamma}{dz} = \frac{q_e E_0}{2 m_e c^2} (\sin{(\phi)} + \sin{(\phi + 2kz)}), \tag{3.6}$$

where $\phi = \omega t - kz + \phi_0$. The electron beam acceleration process in the cavity is completely described by the pair of equations 3.5 and 3.6. Following the assumptions described in [34] one can estimate the optimum gun launching phase ϕ_0 at which the transverse emittance is minimized using the following formula [34]:

$$(\frac{\pi}{2} - \phi_0) \sin{(\phi_0)} = \frac{1}{2\alpha}, \tag{3.7}$$

where $\alpha = \frac{q_e E_0}{2 m_e c^2 k}$ is a dimensionless parameter representing the strength of the RF electric field. Calculation of the optimum gun launching phase for the PITZ nominal parameters results in $\phi_0 = 76.4\,\mathrm{deg}$. This value is much higher than the result obtained from the particle tracking code ASTRA (see Chapter 6) which is $\phi_0 = 44.8\,\mathrm{deg}$ as well as from the experimentally measured $\phi_0 = 52\,\mathrm{deg}$ as it is shown in [35]. Therefore we have to assume that the simplified model of the electric field in the gun described by Eq. 3.5 is not appropriate for our case. This can be explained by significant differences of the RF field in the PITZ gun compared to the proposed model described by Eq. 3.5 as shown in Fig. 3.3 where both fields are depicted for $\mathrm{t} = 0$ and $\phi_0 = 90\,\mathrm{deg}$. As a consequence of this strong discrepancy one cannot use the estimation of the RF induced emittance based on the electric field distribution described by Eq. 3.5 which for a cylindrically shaped electron beam is estimated as shown in [34]:

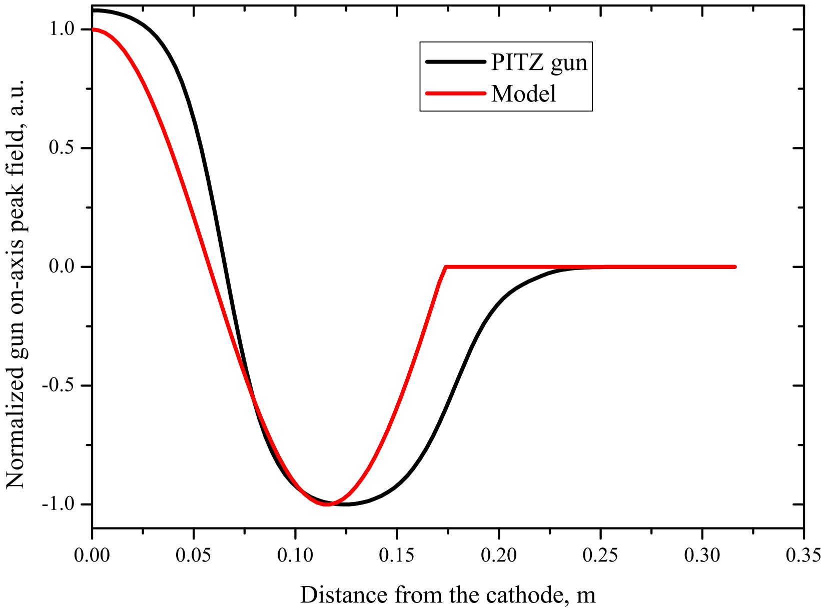

Figure 3.3: Measured longitudinal component of the RF field of the PITZ gun and the electric field of the model described by Eq. 3.5 as a functions of the longitudinal coordinate.

$$\varepsilon_{RF} = \frac{\alpha r^2 k^3 l^2}{4\sqrt{6!}}, \tag{3.8}$$

where r and l are the radius and the length of the electron beam, respectively. For a usual operation with electron beam of $1\,\mathrm{nC}$ charge, gun on-axis peak field of $\mathrm{E}_0 = 60.5\,\mathrm{MV/m}$ and flat-top laser pulse with the length of 21.5 ps at FWHM, result of the simulations (see Chapter 6) shows the emittance minimum value of $\varepsilon_\mathrm{n} = 0.61\,\mathrm{mm\,mrad}$ for the rms laser spot size on the cathode of 0.4 mm. Inserting this conditions to Eq. 3.8 we obtain $\varepsilon_\mathrm{RF} = 0.011\,\mathrm{mm\,mrad}$.

To proper estimate the RF induced emittance one can use the particle tracking code ASTRA. The radial component of the electric field can be estimated using the Maxwell equation in vacuum div $\overrightarrow{E} = 0$. In the cylindrical coordinate system one gets:

$$\frac{1}{r}\frac{\partial}{\partial r}(rE_r(r,z)) + \frac{1}{r}\frac{\partial E_\theta}{\partial \theta} + \frac{\partial E_z}{\partial z} = 0. \tag{3.9}$$

Assuming that the field is independent on θ this simplifies to the following:

$$\frac{\partial}{\partial r}(rE_r(r,z)) = -r\frac{\partial E_z}{\partial z}. \tag{3.10}$$

In a paraxial ray approximation one can show that for a cylindrically symmetric TM standing wave mode the radial component of the electric field can be expanded to the following form [30,36]:

$$E_r(0,z) = -\frac{r}{2}\frac{\partial E_z}{\partial z} + \frac{r^3}{16}\left(\frac{\partial^3 E_z}{\partial z^3} + \frac{\omega^2}{c^2}\frac{\partial E_z}{\partial z}\right). \tag{3.11}$$

One can easily show that the first term does not contribute to the emittance growth. In such a way the obtained emittance difference from the particle tracking code with and without taking into account the second term represents the emittance contribution due to the radial electric field in the gun. The simulations performed for the electron beam with 1 nC charge and the same machine parameters as described above show that this contribution is less than 10^{-3} mm mrad which is at least factor of 10 less than predicted by Eq. 3.8.

As the duration of the laser beam and therefore the produced electron beam is about 21.5 ps, different parts of the beam are accelerated at different phases. As well as the contribution of the radial component of the electric field, the emittance growth due to the finite laser beam length can be estimated from simulations. For this purpose the simulations of the electron beam dynamics were done including the space-charge forces to about 8 mm downstream the cathode. At this distance the effect of the mirror beam field at the cathode is below 1 ‰ and further tracking is performed without the space-charge fields to obtain emittance growth due to RF effects. In such a way the obtained emittance number difference to the thermal emittance will represent the RF contribution upper limit to the emittance growth (except the contribution caused by space-charge, including mirror charge, during the electron extraction process). Thermal emittance of the electron ensemble is a measure of the temperature of the electrons emitted from the cathode. The thermal emittance of an electron beam generated by a cathode imposes a lower limit for the emittance that can be generated by an injector. As there is no correlation between momentum and position of electrons in their initial distribution the Eq. 3.4 reduces to

$$\varepsilon_{n,x} = \beta\gamma\sqrt{\langle x^2\rangle\langle x'^2\rangle}. \tag{3.12}$$

The results of the simulations for the aforementioned conditions yield an emittance growth of 0.01 mm mrad which is about 2.5% of the thermal emittance. The remaining part of the emittance growth is caused by the space-charge forces. Taking into account the small emittance growth due to RF field effects, the total estimated emittance growth caused by the space-charge forces is 0.2 mm mrad, which is about 50% of the thermal emittance.

3.4 Summary

As it was mentioned in previous chapters the operation of such facilities like FLASH and the European X-FEL requires electron beams with a small transverse emittance. As the electron beam has a complex longitudinal structure the transverse phase space distribution changes along the beam. Dividing the electron beam longitudinally on several slices one can also estimate the transverse emittance of each slice separately. Each of such beam slices has a different current and emittance magnitudes. For the FEL lasing process only the slices within the high-current region, and consequently the transverse emittance of these slices, are important [4]. More details about slice emittance and slice emittance measurement methods can be found in [22]. To fulfill the requirements of the European X-FEL the electron beam slice emittance should not exceed 1.4 mm mrad at the entrance of the undulator for the electron beam of 1 nC charge. Taking into account the dilution budget from the injector to the undulator one gets the upper limit in terms of the normalized transverse projected emittance after the injector of $\varepsilon_{\mathrm{n,xy}} < 0.9$ mm mrad for the electron beams with 1 nC charge [11]. In the following chapters we will see that with the current PITZ setup it was possible to satisfy this requirement with a good margins.

Chapter 4

Emittance measurement technique

In this chapter the details of the emittance measurement setup and the emittance measurement method which was used in the frame of this work are described.

4.1 Single slit scan technique

As it was mentioned in Chapter 2.4.4 there are several emittance measurement methods available at PITZ. A tomography reconstruction method of the emittance measurement is widely described in [25]. In the frame of this work a single slit scan method based on the direct measurement of the electron beam size and the beam angular spread was used. The main idea of this method is a measurement of the angular spread of emittance dominated beamlets created from the electron beam with the help of an aperture having a narrow slit shape. This method allows to measure emittance for a certain transverse plain during the certain time by scanning the electron beam with the help of a slit. Therefore it requires a high stability of the machine parameters during this procedure, so-called short term stability. Moreover as the switching between the measurements for different transverse planes at the same machine parameters needs some preparation, the so-called long term stability of the machine parameters is required as well.

The divergence of the beamlet produced with the help of the slit can be measured after its propagation in the drift space using the so-called observation screen installed at the distance $\mathrm{L_d}$ downstream the position of the slit. Assuming the absence of space-charge forces in the produced beamlets the local divergence $\langle x'^2 \rangle$ of the each beamlet at the slit position can be estimated from simple geometry as follows:

$$\langle x'^2 \rangle_i = \frac{\langle x^2 \rangle_{bi}}{L_d^2}, \tag{4.1}$$

where $\sqrt{\langle x^2 \rangle_{bi}}$ is the rms size of the $\mathrm{i^{th}}$ beamlet at the position of the observation screen. In addition, the covariance term $\langle xx' \rangle$ can be calculated as the position of the slit is known at any moment of time with a high precision as it was mentioned in Chapter 2.4.4. The rms electron beam size at the slit position $\sqrt{\langle x^2 \rangle}$ is reconstructed by using the intensity of each beamlet ratio to the intensity over all beamlets as a weight for the certain slit position. Assuming that the rms divergence after the removing of the linear covariance $\langle xx' \rangle$ gives an uncorrelated divergence, the not normalized rms emittance of the electron beam along the given plane can be estimated using Eq. 3.3.

Due to limitations of the optical readout system and sensitivity of the YAG/OTR screens which are used to record the beamlet images, the rms electron beam size reconstructed at the slit position from the measured beamlets is typically less than the rms beam size obtained from a direct measurement with the help of the YAG/OTR screen inserted at the position of the slit. To take into account this difference during the calculation of the emittance the following correction factor is used:

$$f_{xc} = \frac{\sigma_x}{\sqrt{\langle x^2 \rangle}}, \tag{4.2}$$

where σ_x is the rms electron beam size at the position of the slit obtained during a direct measurement with the help of YAG/OTR screen. To obtain the normalized emittance value according to Eq. 3.4 an additional factor $\beta\gamma$ has to be included. As $\beta\gamma = \langle p \rangle / m_0 c$ and $\langle p \rangle \approx \langle p_z \rangle$ it can be calculated during the experiment using $\langle p_z \rangle$ measured with the help of HEDA1 (see Chapter 2.4.2).

Finally taking into account all the previous statements we can derive the equation for the 100 % normalized transverse projected emittance for a given plane as follows:

$$\varepsilon_{n,x} = \beta\gamma \frac{\sigma_x}{\sqrt{\langle x^2 \rangle}} \sqrt{\langle x^2 \rangle \langle x'^2 \rangle - \langle xx' \rangle^2}. \tag{4.3}$$

The transverse projected emittance of the electron beam for both planes then can be calculated as a geometrical average:

$$\varepsilon_{n,xy} = \sqrt{\varepsilon_{n,x} \cdot \varepsilon_{n,y}}. \tag{4.4}$$

4.2 Layout of the emittance measurement stations

The first EMSY station was developed jointly by DESY and the Institute for Nuclear Research and Nuclear Energy in Sofia (INRNE) in 2000-2001 [37]. Later on it was successfully commissioned and several successful emittance measurements were done [6, 38]. The major upgrade of the PITZ facility which in particular brought a booster cavity and new more powerful 10 MW klystron cause a necessity to upgrade the design of the EMSY stations [8]. The current design of the EMSY stations together with one of the actuators is shown in Fig. 4.1 as a 3D view.

The main components of the EMSY stations are two orthogonal actuators driven with stepper motors and containing different elements which can interact with the electron beam. A 3D view of the horizontal actuator is presented in Fig. 4.1b. As it can be seen, it contains two slit masks which have openings of 10 and 50 μm, and a YAG screen installed at 90 deg with respect to the electron beam direction. Behind the YAG screen a mirror which deflects light produced by the screen to a viewport window is installed at 45 deg with respect to the electron beam direction. The vertical actuator has exactly the same structure except that instead of the YAG screen with a mirror, an OTR screen is installed at 45 deg with respect to the electron beam direction. Additionally, to adjust the angular acceptance of the slits, the whole station can be rotated around the transverse axes with the help of two independent rotational stepper motors. As only a small fraction of the electron beam should pass through the slit mask one must ensure that the slit mask thickness is enough to stop the rest of the electrons. On the other hand one cannot build it too thick as this would reduce its angular acceptance. The thickness of 1 mm of tungsten (which is capable of high thermal load and has a small radiation length of about 0.35 cm) was chosen after the estimation of the signal to noise ratio as a function of the drift length. As it is shown in [8] for the beam parameters used at PITZ, the signal to noise ratio is higher than 500 for $\mathrm{L_d} > 0.5$ m.

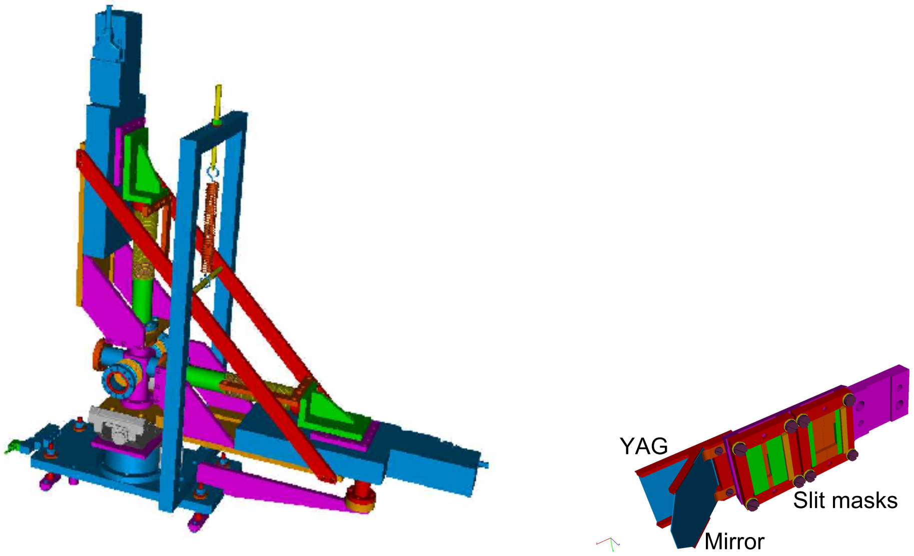

(a) The EMSY station containing two orthogonal actuators and four stepper motors used to move the actuators and rotate them around their axes.

(b) Horizontal actuator containing two slits with different openings and a YAG screen installed at 90 deg with respect to the electron beam direction.

Figure 4.1: 3D view of the EMSY station and the horizontal actuator.

Several effects influencing the estimation of the emittance were taken into account while designing new EMSY stations and described in more details in Chapter 5: e.g. influence of the finite slit opening and space-charge effects. The systematic error in the emittance estimation caused by both effects depends on the drift length L_d which beamlets pass from the EMSY station to the observation screen. Moreover, the systematic error caused by the finite slit opening decreases with increasing of the drift length L_d while the systematic error caused by the space-charge effects increases. In such a way choosing of the optimum drift length L_d is a compromise between this two effects. Based on the results presented in [8], the drift length of $L_d = 2.65\,\mathrm{m}$ was chosen to install the observation screen. The corresponding observation screen for the EMSY1 station is installed at this distance and named High1.Scr4 as shown in Fig. 2.8.

Chapter 5

Systematic errors estimation

In this chapter the systematic errors in the emittance estimation caused by different effects are evaluated.

5.1 Systematic errors due to a finite slit opening and space-charge forces

The finite width of the slit opening leads to the systematic increase of the measured emittance. The rms size of a beamlet created with an infinitely thin slit and having uniform distribution is estimated as $\sigma_{\mathrm{x}} = \mathrm{d}/\sqrt{12}$, where d is the width of the slit opening. Propagating the beamlet for the drift length $\mathrm{L_d}$ to the observation screen its rms size is described as $\sigma_{\mathrm{x}}^{\mathrm{o}} = \sqrt{(\mathrm{d}/\sqrt{12})^2 + \mathrm{L_d^2}\sigma_{\mathrm{x'}}^2}$, where $\sigma_{\mathrm{x'}}$ is the rms divergence of the beamlet. From this relation we can derive that the contribution of the finite slit opening can be neglected if $\mathrm{L_d} \gg \mathrm{d}/\left(\sigma_{\mathrm{x'}}\sqrt{12}\right)$. Estimations based on the machine parameters during the design of the EMSY stations resulted in $\mathrm{L_d} \gg 9\,\mathrm{cm}$ and $\mathrm{L_d} \gg 45\,\mathrm{cm}$ for the 10 and 50 μm slits, respectively [8]. Recalculating the numbers for the actual parameters for 1 nC bunch charge operation (emittance of $\varepsilon = 0.6\,\mathrm{mm\,mrad}$, mean momentum of $\langle \mathrm{p_z} \rangle = 25\,\mathrm{MeV/c}$, rms laser spot size on the cathode $\sigma_{\mathrm{L}} = 0.4\,\mathrm{mm}$) we get $\mathrm{L_d} \gg 12$ and 60 cm for 10 and 50 μm slits, respectively. Since the drift length at PITZ for the EMSY1 station is about 2.6 m the effect of the slit opening is negligible.

Unlike the influence of the finite slit opening on the systematic error in the emittance calculation which decreases with increasing of the drift length, the systematic errors caused by the space-charge effects increases with increasing of the drift length. The calculation of the space-charge effect based on the numerical calculation of the evolution of the beam size during its propagation in the drift space was carefully done in [8]. It was shown that for an initial electron beam at EMSY1 having $\varepsilon = 0.9\,\mathrm{mm\,mrad}$, $\langle \mathrm{p_z} \rangle = 30\,\mathrm{MeV/c}$ and $\sigma_\mathrm{x} = 0.2\,\mathrm{mm}$ the emittance overestimation after $\mathrm{L_d} > 2.5\,\mathrm{m}$ saturates at the level of about 15 % and 4 % for 50 and 10 μm slits, respectively. Summarizing the obtained results it was decided to use 10 μm slit for the measurements. Nevertheless, it was also decided to install the 50 μm slit, instead of a multi slit mask used in the past, with the aim to increase the intensity of the beamlets on the observation screen in cases of electron beams with higher emittance that leads to reduced contribution of the finite slit opening and space-charge effects [8]. All emittance measurements presented in Chapter 7 were done using the 10 μm slit.

5.2 Systematic errors due to the finite size of camera pixels and digitalization of the signal

The finite size of camera pixels and digitalization of the signal introduce systematic errors in the estimation of the rms electron beam size, divergence and covariance term between them at the position of the emittance measurement. The systematic error on the estimation of the rms electron beam size and covariance term at the position of EMSY1 for different charges can be estimated using simulation results. For this purpose the transverse electron beam distribution at the position of EMSY1 is imaged according to the spatial discretisation of the camera. Also the intensity of the signal is digitized according to the digital resolution of the camera. For the estimation, lets take the parameters of the Prosilica-GC1350 camera [39] used in 2x2 binning mode together with a magnification lens with a focal length of 250 mm which are mostly used during the emittance measurements at PITZ. Results of the emittance calculation from transverse trace spaces obtained from the simulations, taking into account a finite pixel size of the CCD camera and its digital signal structure, together with emittance directly calculated from the transverse trace spaces are presented in Table 5.1 for different electron beam charges. As we can see, a systematic overestimation of the emittance

Beam charge, nC	**Raw simulation data**			
	$\sigma^{\mathrm{s}}_{\mathrm{x}}$, mm	$\sigma^{\mathrm{s}}_{\mathrm{x'}}$, mrad	$\sigma^{\mathrm{s}}_{\mathrm{xx'}}$ mm mrad	$\varepsilon^{\mathrm{s}}_{\mathrm{x}}$, mm mrad
2	0.797619	0.179929	0.141839	1.13748
1	0.526439	0.140105	0.0730336	0.609874
0.25	0.258289	0.0742614	0.0183617	0.261844
0.1	0.162083	0.0584483	0.00869369	0.177727
0.02	0.247868	0.136919	0.0339129	0.0615554
	Pixel size included			
	$\sigma^{\mathrm{c}}_{\mathrm{x}}$, mm	$\sigma^{\mathrm{c}}_{\mathrm{x'}}$, mrad	$\sigma^{\mathrm{c}}_{\mathrm{xx'}}$ mm mrad	$\varepsilon^{\mathrm{c}}_{\mathrm{x}}$, mm mrad
2	0.79762	-	0.141838	1.13786
1	0.526457	-	0.072961	0.628226
0.25	0.25831	-	0.0183759	0.259857
0.1	0.162128	-	0.00867634	0.179921
0.02	0.247892	-	0.0337892	0.151565
	Error			
	$\frac{\sigma^{\mathrm{c}}_{\mathrm{x}}}{\sigma^{\mathrm{s}}_{\mathrm{x}}} - 1$	-	$\frac{\sigma^{\mathrm{c}}_{\mathrm{xx'}}}{\sigma^{\mathrm{s}}_{\mathrm{xx'}}} - 1$	$\frac{\varepsilon^{\mathrm{c}}_{\mathrm{x}}}{\varepsilon^{\mathrm{s}}_{\mathrm{x}}} - 1$
2	$< 1\%$	-	$> -1\%$	$< 1\%$
1	$< 1\%$	-	$> -1\%$	3%
0.25	$< 1\%$	-	$< 1\%$	$> -1\%$
0.1	$< 1\%$	-	$> -1\%$	1.22%
0.02	$< 1\%$	-	$> -1\%$	146%

Table 5.1: Systematic errors caused by the finite size of camera pixels for electron beams with different charges. σ_{x}, $\sigma_{\mathrm{xx'}}$, $\sigma_{\mathrm{xx'}}$ are rms size, rms divergence and covariance of the electron beam at the position of EMSY1. Index "s" states for results obtained from raw simulations data, index "c" for the results obtained from simulations data taking into account camera properties.

values by less than 3% is expected for electron beams with 1 nC and 100 pC charges. For an electron beam with a 250 pC and 2 nC charges the systematic errors in the emittance estimation is negligible. A special case is the overestimation of the emittance value more than twice for an electron beam with 20 pC charge. As for this charge the divergence and the size of the beam at the position of EMSY1 are quite small, the modification of the original distribution according to the camera nature cause a severe calculation errors.

5.3 Systematic errors due to machine parameters deviation from their optimum values

The detuning of such parameters like rms the laser spot size on the cathode, main solenoid current, gun and booster launching phases and booster accelerating gradient from their optimum values results in a systematic increase of the measured emittance values. The following estimations are done based on the simulation results presented in Chapter 6 and experimental data presented in Chapter 7. According to simulation results the booster launching phase has only a minor impact on the emittance values as it is described in [35]. Therefore this parameter was excluded in further estimations. Analyzing the emittance dependencies for different charges on the CDS booster accelerating gradient and taking into account that the momentum measurement error at PITZ is much less than 0.85 MeV/c which corresponds to a change of the CDS booster on-axis peak field of 1 MV/m used in simulations, one can remove this parameter from further estimations as well. Despite that the measurement error of the rms laser spot size on the cathode is less than 10 μm one cannot precisely determine its optimum value during the experiments due to a lack of run time. The step width with which the rms laser spot size on the cathode was scanned during the experimental measurements depends on the electron beam charge and is presented in Table 5.2. The determination of the maximum mean momentum gain gun launching phase, hereinafter MMMG gun launching phase, from the LEDA momentum scans gives a possible error of $\Delta\phi = 1$ deg. Nevertheless due to a lack of run time the emittance dependence on the gun launching phase was

Charge, nC	$\Delta\sigma_{\mathrm{L}}$, mm
2	0.05 - 0.08
1	0.05 - 0.075
0.25	0.05 - 0.075
0.1	0.0125 - 0.025
0.02	0.0125 - 0.025

Table 5.2: Step width used for the rms laser spot size on the cathode during the experimental measurements.

only studied with a step width of 3 deg for electron beams with a charge of 1 nC (see Chapter 7.1.2). Despite that emittance dependencies on the gun launching phase were not measured for electron beams with other charges one can take the step width of 3 deg during the estimation of the systematic error in the emittance values for other electron beam charges as well. The emittance dependence on the main solenoid current is studied using 1 A step width during the experiments. Taking into account estimations of possible deviation of machine parameters from their optimum values one can estimate the systematic errors based on the simulation data for different electron beam charges. The results of these estimations are presented in Table 5.3. As we can see for all electron beam charges the systematic errors are about 10 %.

Charge, nC	$\varepsilon^{\mathrm{d}}/\varepsilon^{\mathrm{s}} - 1$
2	8%
1	12%
0.25	13%
0.1	8%
0.02	10%

Table 5.3: Systematic errors caused by deviation of the machine parameters from their optimum values for different electron beam charges. ε^{s} corresponds to the minimum emittance value obtained during the simulation, ε^{d} corresponds to the maximum emittance value during the simulation with a certainly limited range of machine parameters, see text.

Chapter 6

Simulations results

In this chapter the emittance simulations performed with a particle tracking code which includes the emission process from the photocathode and space-charges force are presented. The simulations were done for different beam charges varying such parameters like the transverse and longitudinal size of the laser beam, gun and booster accelerating gradients and their launching phases as well as the main solenoid current. In the following sections emittance dependencies on these parameters for different beam charges are described in detail. Hereinafter to the end of the chapter, the word "emittance" is used for normalized transverse projected emittance calculated according to the Eq. 3.4.

6.1 Prerequisites for the emittance simulations

A Space Charge TRacking Algorithm ASTRA [36] was used to perform the emittance simulations for the PITZ setup. This code is based on the tracking of particles through user defined external fields, such as electromagnetic RF fields in the gun and CDS booster, solenoid field, dipole and quadrupole fields, and taking into account the space-charge field of the particle ensemble. The space-charge field can be calculated in 3D or in 2D-cylindrical symmetry. For the simulations presented in the following sections only 2D-cylindrical symmetry was used as all input components are cylindrically symmetrical. Therefore X and Y transverse trace spaces are nearly identical for each simulation case and only X transverse trace spaces are presented in the following sections. The tracking process is based on a non-adaptive Runge-Kutta integration up to 4th order. In such a way the tracking time directly depends on the amount of tracked particles. As an electron beam with a charge of 1 nC contains about 10^{10} electrons, the calculation time of such a huge particle ensemble would be in the order of years. To overcome this problem the amount of particles tracked by ASTRA is limited by the user and the defined charge is distributed between these particles. In such a way the tracking is performed not for single electrons but for macroparticles. Each macroparticle represents an ensemble of particles. During the simulations presented in this work $2 \cdot 10^5$ macroparticles were used.

A conventional right-hand axis coordinate system is used in ASTRA. The electron beam propagates along the Z axis. The beamline elements are set with respect to this coordinate system. Except the user-defined beamline elements and their fields, an initial electrons distribution at the cathode is necessary to perform simulations with ASTRA. This distribution contains all the information necessary for the tracking process: momentum distributions, transverse and time distributions. There are several particle distributions at the cathode which can be generated by an additional tool named "generator". In our case cylindric symmetrical uniform transverse distributions, which are closest to the experimentally measured ones, of different rms sizes were used. During the experimental studies only a flat-top longitudinal laser distribution with a fixed length of about 21.5 ps at FWHM and fixed rise/fall times of about 2 ps was used. In the simulations flat top time distributions with different lengths and fixed rise/fall times of 2 ps were used. Uniform transverse momentum distribution and longitudinal momentum distribution with isotropic emission angles into a half sphere were used. The width of the momentum distribution of the electrons at the cathode can be estimated as explained in Chapter 3.1. According to the experimental setup the following fields were used in the simulations: gun field, solenoid field and booster field (see Fig. 2.5). The aperture of the beamline elements was included as well. Particle tracking was done up to 15 m from the cathode, while the emittance values presented in the following sections were obtained at the position of EMSY1 located 5.74 m downstream the cathode.

6.2 1 nC charge simulations

The initial point for the matching of simulations for electron beams with different charges to the experimental data is a reproduction of the experimentally measured electron beam momentum. During the experimental study of the electron beam with 1 nC charge a mean electron beam momentum of $6.742 \pm 0.023\,\mathrm{MeV/c}$ at MMMG phase was measured using LEDA (see Chapter 2.4.2). Flat-top laser temporal profile with a FWHM of about 21.5 ps and 2 ps rise/fall times was used during these measurements. As the electron beam momentum at MMMG phase is defined mainly by the gun accelerating gradient and laser pulse length, a set of simulations with different gun accelerating gradients for a fixed laser pulse length of 21.5 ps at FWHM was done and is described in the following section. An electron beam momentum of 6.7 MeV/c was obtained for the gun on-axis peak field value of $\mathrm{E_g^p} = 60.5\,\mathrm{MV/m}$ which is in a good agreement with 60 MV/m estimated from the experimentally measured power in the gun. During all the simulations except the ones presented in Chapter 6.2.1 a gun on-axis peak field of $\mathrm{E_g^p} = 60.5\,\mathrm{MV/m}$ was used. As it was shown in [35] the emittance dependence on the booster launching phase is quite weak and delivers the minimum emittance value at phase far from MMMG phase and therefore is out of practical interest due to a large energy spread. Therefore the booster launching phase was fixed to MMMG phase during all simulations.

Taking into account the aforementioned conditions the following set of the machine parameters was varied in order to obtain the minimum emittance value: gun launching phase, main solenoid current, booster accelerating gradient and rms laser spot size on the cathode. The multi parameter scan on these parameters yields a minimum emittance value of $\varepsilon_\mathrm{n} = 0.61\,\mathrm{mm\,mrad}$ at the main solenoid current of $\mathrm{I_{main}} = 386\,\mathrm{A}$, rms laser spot size on the cathode of $\sigma_\mathrm{L} = 0.4\,\mathrm{mm}$, gun launching phase of $\Phi_\mathrm{g} = 0\,\mathrm{deg}$ with respect to MMMG phase and CDS booster on-axis peak field of $\mathrm{E_b^p} = 19\,\mathrm{MV/m}$. The mean electron beam momentum at these conditions is estimated to be about $\langle \mathrm{p_z} \rangle = 23.3\,\mathrm{MeV/c}$ which is close to the experimentally measured (see Chapter 7). The corresponding transverse trace space and transverse distribution of the electron beam are presented in Fig. 6.1. The slice peak current is estimated to be $\mathrm{I^p} = 43.1\,A$. This result gives a starting point for further investigations of the electron beam emittance dependencies on different machine parameters.

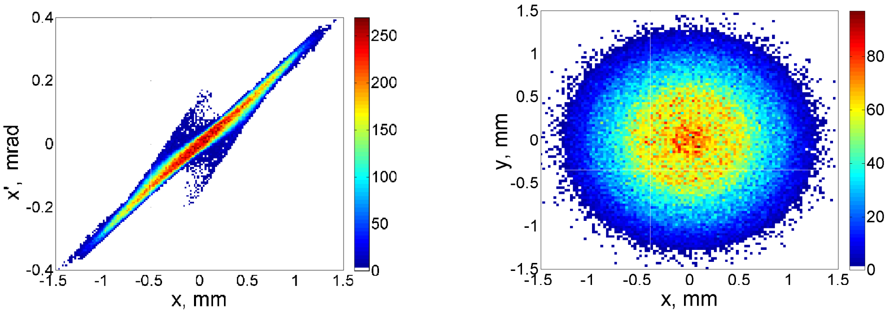

(a) Trace space. (b) Distribution.

Figure 6.1: Simulated transverse trace space and transverse distribution of the electron beam with 1 nC charge delivering the minimum emittance value at fixed laser pulse length with FWHM of 21.5 ps and 2 ps rise/fall times and fixed gun on-axis peak field of $E_g^p = 60.5$ MV/m. Colorbars represent the intensity in arbitrary units. Electron beam momentum is about $\langle p_z \rangle = 23.3$ MeV/c.

6.2.1 Emittance dependence on the gun accelerating gradient

As it was mentioned the nominal working gradient of the PITZ gun corresponds to an on-axis peak field value of about 60 MV/m which is the designed operating point for the future European XFEL [40]. The current FLASH setup operates at a reduced gun on-axis peak field of about 45 MV/m. The emittance simulations for different gun on-axis peak fields were performed in order to study the dependence of the different machines parameters delivering the minimum emittance value and estimate the possible emittance improvement by changing the FLASH operation to the 60 MV/m regime and exchange of its photocathode laser system. The main result of the simulations, the emittance dependence on the gun on-axis peak field, is presented in Fig. 6.2. Two dedicated red squares corresponds to the simulations with the current FLASH laser system which produces longitudinally Gaussian pulses with FWHM of about 15.3 ps [41]. As it will be shown later in this chapter the minimum achievable emittance does not depends on the type of the booster cavity. Therefore the emittance reduction by a factor of 1.33 can be expected with an exchange of the FLASH photocathode laser system to the PITZ type. With a simultaneous increase of gun on-axis peak field to the 60 MV/m used at PITZ the emittance reduction by a factor 2.33 can be expected. To obtain the emittance data presented in Fig. 6.2, for each gun accelerating gradient the following machine parameters were optimized: main solenoid current, gun launching phase, booster accelerating gradient and rms laser spot size on the cathode. Other machine parameters were kept as described above. Analyzing the machine parameters at which the minimum emittance value for each gun on-axis peak field value was found, the following dependencies of the rms laser spot size on the cathode and the main solenoid current on the gun on-axis peak field were calculated and are presented in Fig. 6.3. Growth of the optimum laser rms transverse beam

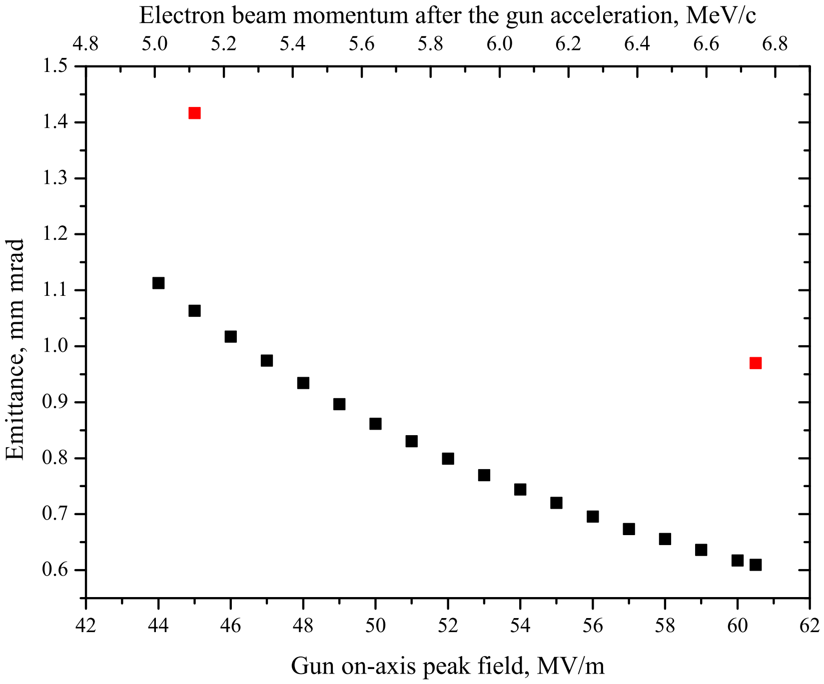

Figure 6.2: Emittance dependence on the gun on-axis peak field for the electron beam with a charge of 1 nC. The top abscissa represents the momentum values of the electron beam after the gun acceleration at MMMG phase for the corresponding gun on-axis peak field value. Black squares represent the simulations for longitudinally flat-top laser pulse with the length of 21.5 ps at FWHM and 2 ps rise/fall times used at PITZ. Red squares represent the simulations for the FLASH type laser for longitudinally Gaussian laser pulses with the length of 15.3 ps at FWHM.

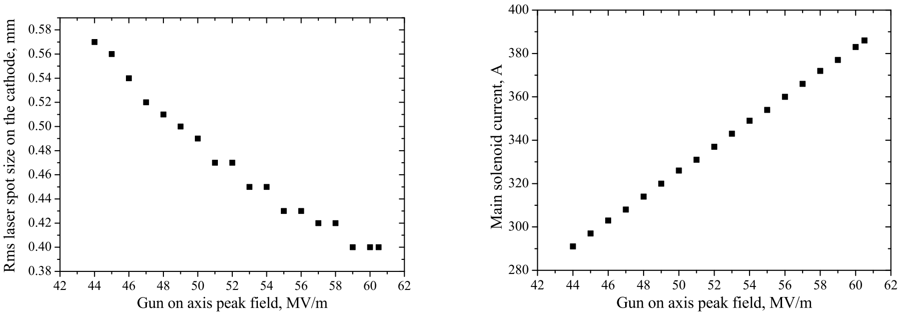

(a) Rms laser spot size on the cathode.

(b) Main solenoid current.

Figure 6.3: Rms laser spot size and main solenoid current, at which minimum emittance values were found, dependencies on the gun on-axis peak field for the electron beam with a charge of 1 nC and fixed laser pulse length with FWHM of 21.5 ps and 2 ps rise/fall times.

size on the cathode towards lower gradients is caused by the relative growth of the nonlinear space-charge forces due to decreasing of the electron beam energy. The gun accelerating gradient is proportional to the final energy of the electron beam after acceleration and the main solenoid current depends linearly on the gun on-axis peak field in the simulations.

Booster on-axis peak field and gun launching phase dependencies delivering the minimum emittance value as a function of the gun accelerating gradient are presented in Fig. 6.4. The optimum booster on-axis peak field value fluctuates around 17.75 MV/m. It can be assumed that the optimum booster on-axis peak field value is not changing while varying the gun on-axis peak field and its fluctuation obtained in simulations is caused by too rough steps on the other parameters during their optimization. We can consider some weak trend on the optimum gun launching phase towards negative direction meaning relative growth of the space-charge induced emittance compared to the RF-induced emittance as the electron beam is more compressed for the positive phases.

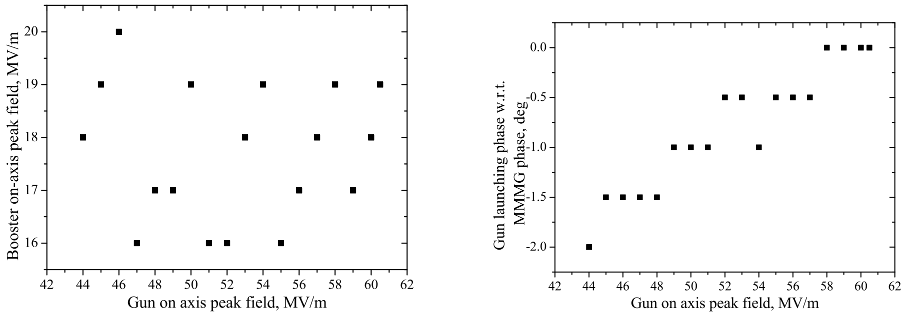

(a) Booster on-axis peak field. (b) Gun launching phase.

Figure 6.4: Booster on-axis peak field and gun launching phase, at which minimum emittance values were found, dependencies on the gun on-axis peak field for the electron beam with a charge of 1 nC and fixed laser pulse length with FWHM of 21.5 ps and 2 ps rise/fall times.

6.2.2 Emittance dependencies at fixed gun accelerating gradient

Emittance dependencies on such machine parameters like main solenoid current, gun launching phase, booster on-axis peak field and rms laser spot size on the cathode were studied for the gun on-axis peak field of $E_g^p = 60.5\,\mathrm{MV/m}$ and fixed laser pulse length with FWHM of 21.5 ps with rise/fall times of 2 ps. The results of these studies are presented in Fig. 6.5a-6.5d. As it was mentioned the gun on-axis peak field of $E_g^p = 60.5\,\mathrm{MV/m}$ corresponds to experimentally used at PITZ and also will be used at the future European XFEL facility. The electron beam momentum after the gun acceleration at these conditions is about $\langle p_z \rangle = 6.7\,\mathrm{MeV/c}$ at MMMG gun launching phase. Additionally, emittance dependence on the laser pulse length was simulated and is presented in Fig. 6.5e. The emittance dependence on the booster on-axis peak field is presented in Fig. 6.5a and shows the minimum emittance value at a booster on-axis peak field of $E_b^p = 19\,\mathrm{MV/m}$. As we can see the emittance value stays rather constant for booster on-axis peak fields higher than $E_b^p = 14\,\mathrm{MV/m}$. The black dots represent optimized emittance values for each booster on-axis peak field value while the rest of the machine parameters (main solenoid current, rms laser spot size on the cathode and gun launching phase) where varied in order to obtain the minimum emittance value. The curve represented by the red dots was obtained by fixing the

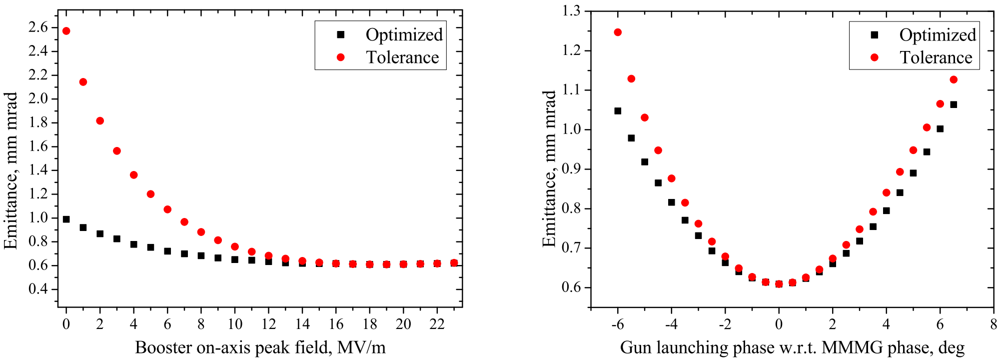

(a) Emittance dependence on the booster on-axis peak field.

(b) Emittance dependence on the gun launching phase.

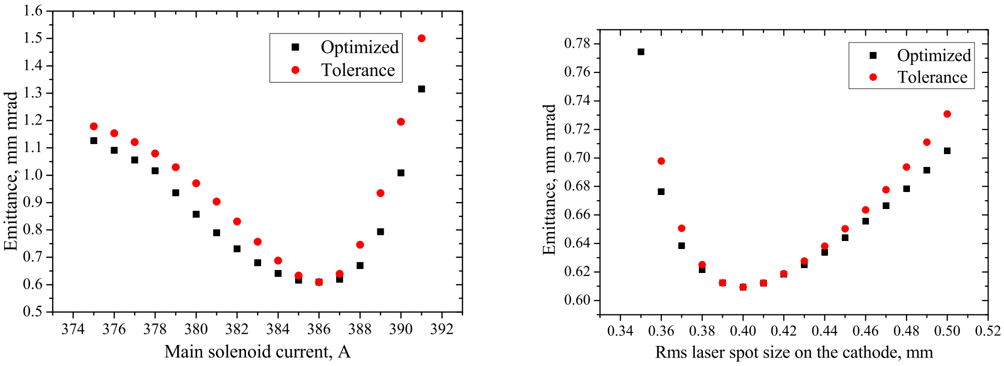

(c) Emittance dependence on the main solenoid current.

(d) Emittance dependence on the rms laser spot size on the cathode.

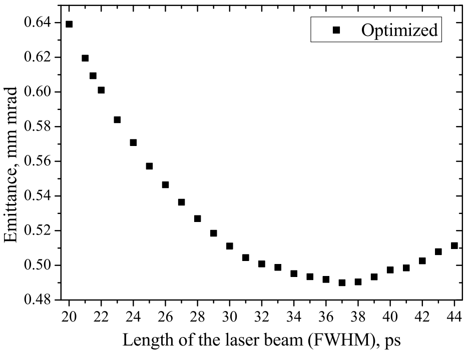

(e) Emittance dependence on the laser pulse length.

Figure 6.5: Emittance dependencies on different machine parameters for 1 nC electron beam charge, gun on-axis peak field of $E_g^p = 60.5$ MV/m and fixed laser pulse length (except last subfigure) with FWHM of 21.5 ps and 2 ps rise/fall times.

rms laser spot size on the cathode, main solenoid current and gun launching phase to the values which deliver the global minimum emittance value at a booster on-axis peak field of $\mathrm{E_b^p} = 19\,\mathrm{MV/m}$ and varying only booster on-axis peak field. In such a way it represents the emittance deviation from the minimum value in case of the detuning of booster on-axis peak field from its optimum value. The values of the main solenoid current, laser spot size on the cathode and gun launching phase at which minimum emittance values were found for each booster on-axis peak field value are presented in Fig. 6.6a-6.6c. As it can be seen all the parameters are slowly changing in the whole range of the simulated booster on-axis peak fields. There is no change in the optimum parameters for the booster on-axis peak fields values in a range of $[17; 22]\,\mathrm{MV/m}$.

The emittance dependence on the gun launching phase is presented in Fig. 6.5b and shows the minimum emittance value at $\Phi_\mathrm{g} = 0\,\mathrm{deg}$ with respect to MMMG phase. Both curves presented in this plot were obtained in the same manner as described above. Also, the red dotted curve represents the emittance dependence on gun launching phase while the main solenoid current, rms laser spot size on the cathode and booster on-axis peak field values are fixed to the values delivering the minimum emittance. The black filled squares represents the emittance dependence on the gun launching phase while the aforementioned parameters were varied as well for each gun launching phase. As we can see there is a quite strong dependence of the emittance on the gun launching phase: a phase offset of 6 deg in any direction from the optimum phase (which is MMMG phase) almost doubles the emittance value. The emittance growth for the emittance dependence on the gun launching phase at the right side from the optimum emittance value is caused by an increasing of the RF-induced emittance due to a stretching of the electron beam. For negative phases the beam compresses and space-charge forces dominate. Also we can notice that the difference between optimized and tolerant curves values is not so big, especially for positive phases, that gives the possibility to neglect the other parameters optimization during the experimental studies. As it was mentioned the data presented by the black filled squares in Fig. 6.5b were obtained by varying the main solenoid current, rms laser spot size on the cathode and booster on-axis peak field for each gun launching phase. Therefore one can build the dependencies of the aforementioned parameters delivering the minimum emittance value at each gun launching phase. These dependencies are presented in Fig. 6.6d-6.6f. As we can see there are quite small changes of the optimum solenoid current and

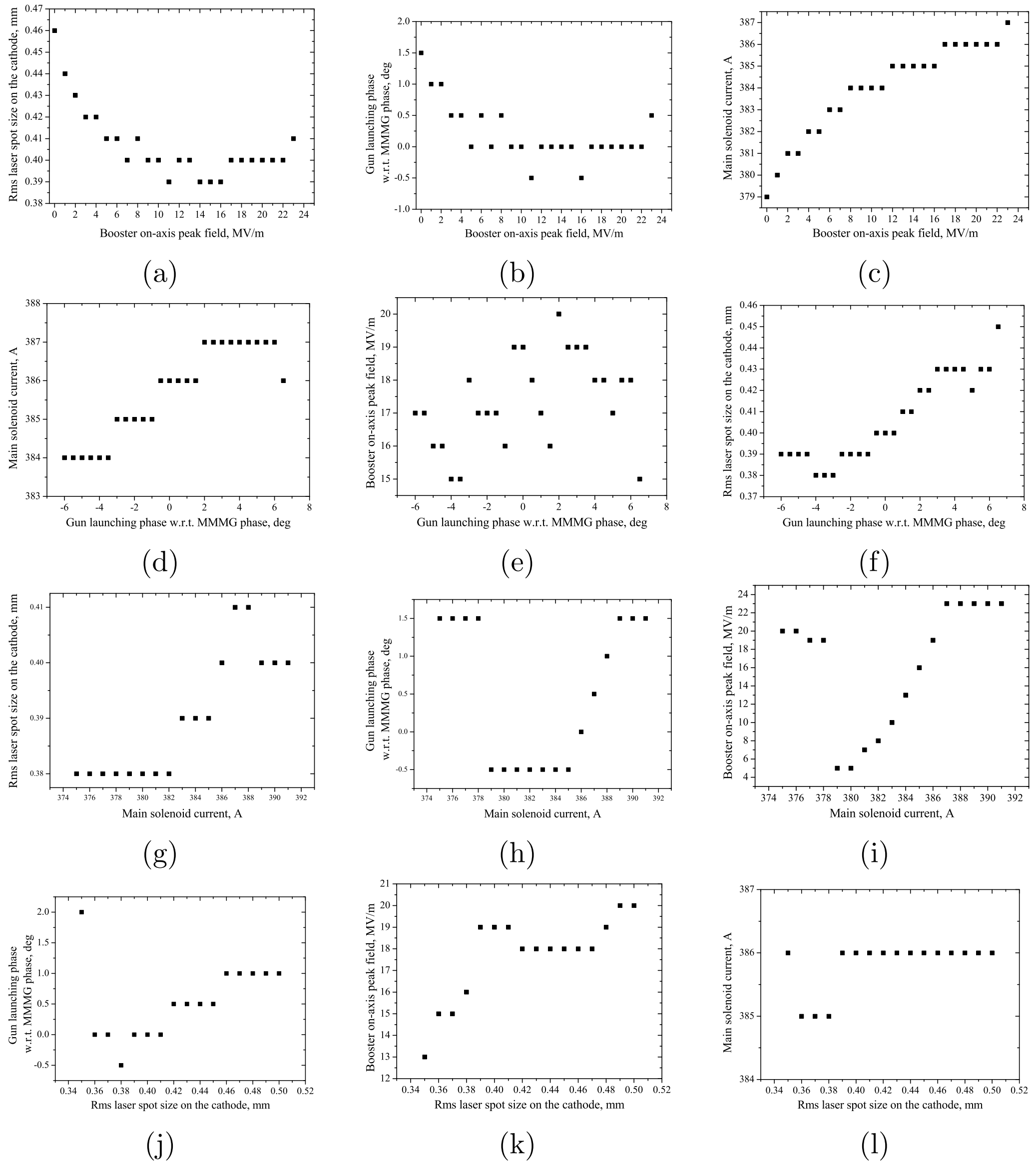

(a) (b) (c)

(d) (e) (f)

(g) (h) (i)

(j) (k) (l)

Figure 6.6: Dependencies of different parameters on a certain parameter delivering the minimum emittance value. Each triplet of plots corresponds to a certain plot from Fig. 6.5.

booster on-axis peak field values over the tested range of phases while the variation of the optimum rms laser spot size on the cathode is significant.

The emittance dependence on the main solenoid current is presented in Fig. 6.5c and shows the minimum emittance value at the main solenoid current of $\mathrm{I}_{\mathrm{main}} = 386\,\mathrm{A}$. The meaning of the red and black curves are the same to described above except that varying parameters set is changed to rms laser spot size on the cathode, booster on-axis peak field and gun launching phase. The values of the booster on-axis peak field, laser spot size on the cathode and gun launching phase at which minimum emittance values were found for each main solenoid current value are presented in Fig. 6.6g-6.6i. The variation of the optimum gun launching phase and rms laser spot size on the cathode is quite moderate while the optimum value of the booster on-axis peak field changes significantly. For the high solenoid currents the optimum booster peak field is artificially saturated as experimentally it is not possible to achieve higher fields at the current PITZ setup.

The emittance dependence on the rms laser spot size on the cathode is presented in Fig. 6.5d and shows the minimum emittance value at $\sigma_{\mathrm{L}} = 0.4\,\mathrm{mm}$. The meaning of the red and black curves is the same as described above except that the varying parameters set is changed to booster on-axis peak field, main solenoid current and gun launching phase. The emittance growth for the emittance dependence on the rms laser spot size on the cathode at the left side from the optimum emittance value is caused by approaching space-charge limited extraction of the electrons from the cathode and an increased contribution of the space-charge forces to the emittance, while on the right side the thermal emittance (see Chapter 3.3) increases. The emittance dependence on this parameter is much weaker towards larger spot sizes from the optimum value. As well as in the previous cases the deviation between optimized and tolerance emittance curves is small in a wide range of the tested rms laser spot sizes. Dependencies of the rms laser spot size on the cathode on other parameters are built in the same manner as described above and presented in Fig. 6.6j-6.6l. As we can see there is a quite small change of the optimum gun launching phase for whole range of rms laser spot sizes on the cathode. The optimum booster on-axis peak field changes quite slowly on the right side from the optimum rms laser spot size on the cathode value while on the left side decreases significantly. This decrease is caused by stronger mixing of the slices while approaching space-charge dominated regime. There is no changes of the optimum main solenoid current almost for the whole range of the laser spot sizes. Nevertheless one may not exclude some weak dependence as the step size at which the main solenoid current was scanned during the simulation was 1 A.

The emittance dependence on the length of the UV laser pulse is presented in Fig. 6.5e. As it can be seen the minimum emittance value of 0.49 mm mrad was found at a laser pulse length with FWHM of 37 ps including rise/fall times of 2 ps which is quite far from the usual 21.5 ps used at PITZ. Despite that the emittance value obtained for a laser pulse length with FWHM of 37 ps is about 20% smaller than for a laser pulse length of 21.5 ps one should take into account the general feature of any RF gun - the coupling between transverse and longitudinal emittance. As an increasing of the laser pulse length leads to an increasing of the longitudinal emittance the capabil-

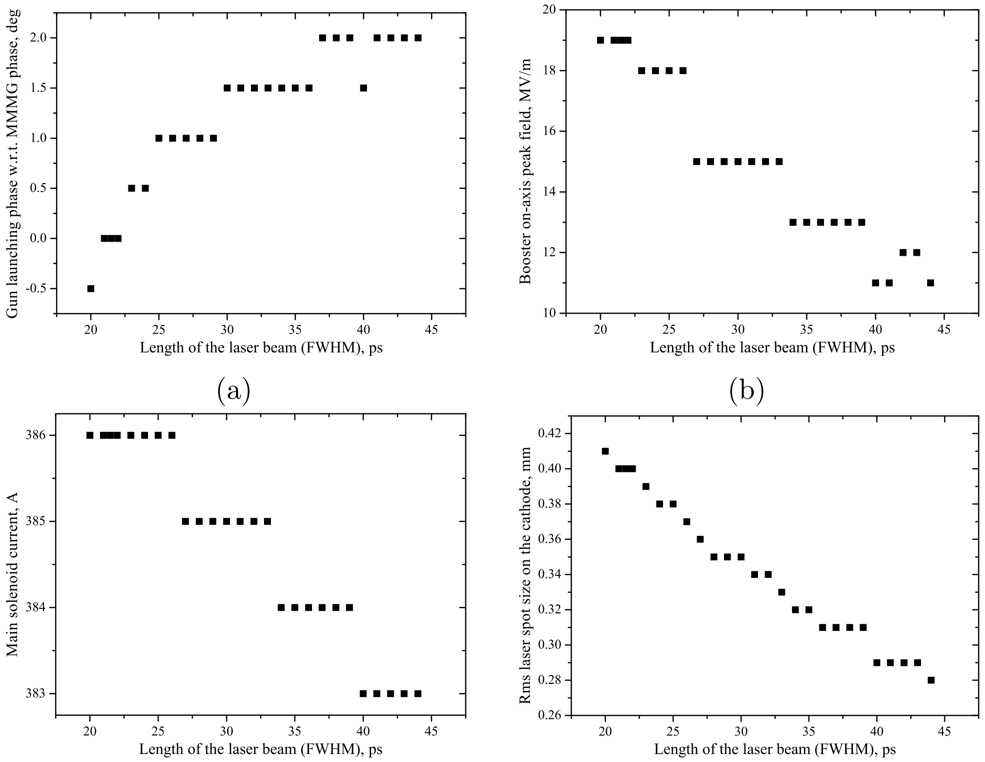

(a) (b)

(c) (d)

Figure 6.7: Rms laser spot size, gun launching phase, main solenoid current and booster on-axis peak field, at which minimum emittance values were found, dependencies on the laser pulse length.

ity of the beam compression is reduced that leads to a reduced beam peak current which is proportional to the final brightness of the electron beam and consequently the laser light brilliance [11]. Additionally, a 3^{rd} harmonic accelerating cavity is used to compensate the nonlinearities introduced by the RF at FLASH as well as at the future European XFEL. The capability of this cavity to correct the nonlinearities in the longitudinal phase space depends on the electron beam length (which implies the UV laser pulse length) and as shown in [11] is optimized for a UV laser pulse length with FWHM of 20 ps. Dependencies of the other parameters delivering the minimum emittance values at each laser pulse length are presented in Fig. 6.7. One can see that the optimum gun lunching phase and main solenoid current almost do not change for the whole range of tested laser pulse lengths while the booster on-axis peak field and rms laser spot size on the cathode decreases quite fast. Additionally, from Fig. 6.7d one can see that the rms beam volume is invariant for a given charge. For a 1 nC beam charge calculating the charge density as $\rho_{\mathrm{Q}} = \mathrm{Q}_{\mathrm{beam}}/\mathrm{V}_{\mathrm{rms}}$ one gets $\rho_{\mathrm{Q}} = 0.311 \pm 0.009\,\mathrm{nC}/(\mathrm{mm}^2\,\mathrm{ps})$.

6.3 250 pC charge simulations

Emittance studies for the electron beams with 250 pC charge have a practical interest as this charge is the nominal charge for the electron beam at LCLS [42]. For the PITZ setup and electron beam with 250 pC charge the minimum emittance value of $\varepsilon_{\mathrm{n}} = 0.236\,\mathrm{mm\,mrad}$ was found for a fixed gun on-axis peak field of $\mathrm{E}_{\mathrm{g}}^{\mathrm{p}} = 60.5\,\mathrm{MV/m}$ corresponding to an electron beam momentum after the gun acceleration of about 6.7 MeV/c and fixed length of the initial laser beam with FWHM of 21.5 ps and 2 ps rise/fall times. As well as for the 1 nC simulations the CDS booster launching phase was kept constant at the MMMG phase. The values of rms laser spot size on the cathode, main solenoid current, gun launching phase and booster on-axis peak field at which minimum emittance value was found are $\sigma_{\mathrm{L}} = 0.18\,\mathrm{mm}$, $\mathrm{I}_{\mathrm{main}} = 381\,\mathrm{A}$, $\Phi_{\mathrm{g}} = 1.5\,\mathrm{deg}$ with respect to MMMG phase and $\mathrm{E}_{\mathrm{b}}^{\mathrm{p}} = 7\,\mathrm{MV/m}$, respectively. The corresponding transverse trace space and transverse distribution are presented in Fig. 6.8. As we can see the minimum emittance value was found at reduced booster on-axis peak field compared to a 1 nC case and is not a practical case as one has to accelerate the beam to higher energies. Therefore additional simulations were done at fixed booster on-axis peak field $\mathrm{E}_{\mathrm{b}}^{\mathrm{p}} = 20\,\mathrm{MV/m}$ which roughly corresponds to the experimentally

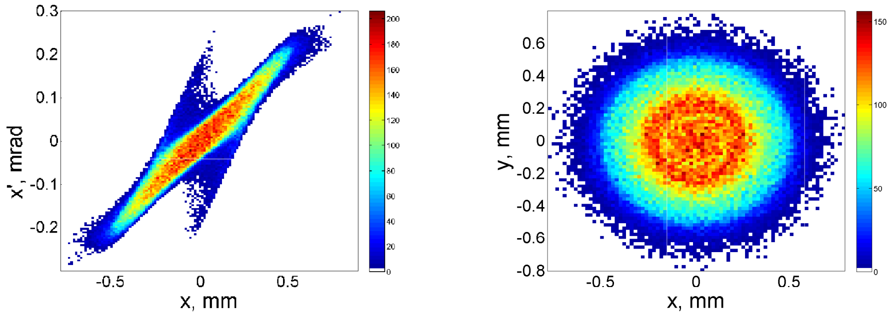

(a) Trace space. (b) Distribution.

Figure 6.8: Simulated transverse trace space and transverse distribution of the electron beam with 250 pC charge delivering the minimum emittance value at fixed laser pulse length with FWHM of 21.5 ps and 2 ps rise/fall times and fixed gun on-axis peak field of $\mathrm{E_g^p} = 60.5\,\mathrm{MV/m}$. Colorbars represent the intensity in arbitrary units. Electron beam momentum is about $\langle \mathrm{p_z} \rangle = 12.8\,\mathrm{MeV/c}$.

highest available field and was used during the experimental studies (see Chapter 7). The results of this additional simulations are described in Chapter 6.3.2

6.3.1 Emittance dependencies on various machine parameters including varied booster on-axis peak field

Dependencies of the emittance on the aforementioned parameters were studied in more details. Additionally, the emittance dependence on the length of the laser beam was studied. All of them are presented in Fig. 6.9. The emittance dependence on the booster on-axis peak field is presented in Fig. 6.9a and shows the minimum emittance value at the booster on-axis peak field value of $\mathrm{E_b^p} = 7\,\mathrm{MV/m}$ which is far away from the value used during the experimental measurements (see Chapter 7.2 for details). Nevertheless the emittance growth is only about 10% for the whole range of the booster on-axis peak field values right-side from the optimum value. A big difference between optimized and tolerance curves indicates about significant parameters changes for not optimum booster peak fields. The detailed dependencies

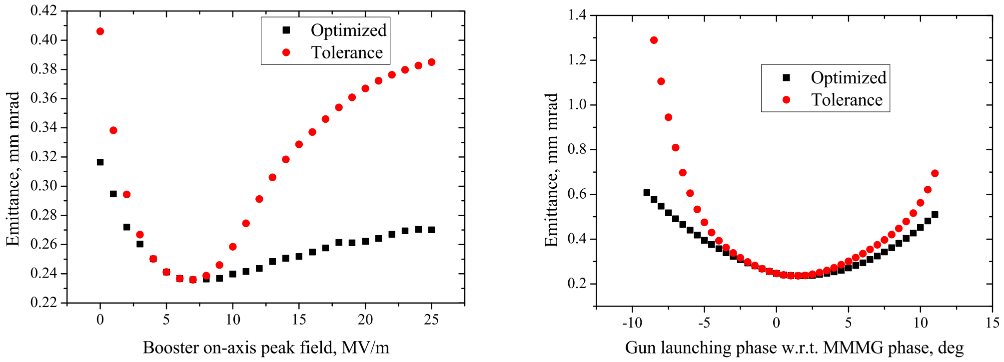

(a) Emittance dependence on the booster on-axis peak field.

(b) Emittance dependence on the gun launching phase.

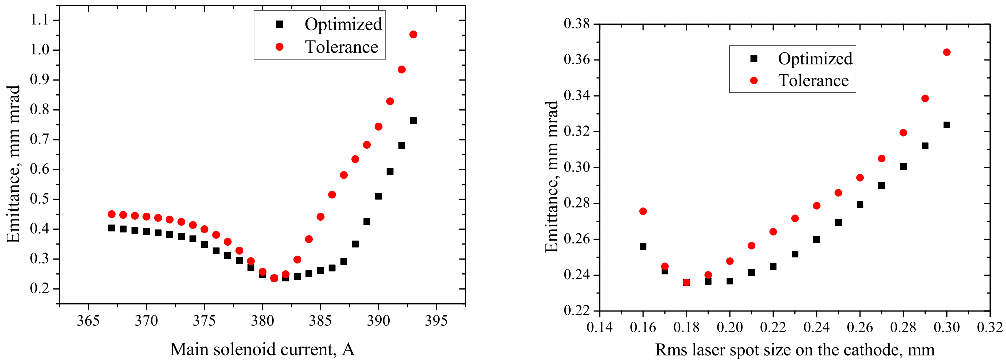

(c) Emittance dependence on the main solenoid current.

(d) Emittance dependence on the rms laser spot size on the cathode.

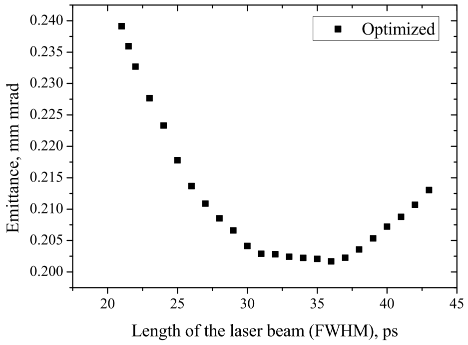

(e) Emittance dependence on the laser pulse length.

Figure 6.9: Emittance dependencies on different machine parameters for 250 pC electron beam charge, gun on-axis peak field of $E_g^p = 60.5\,\mathrm{MV/m}$ and fixed laser pulse length (except last subfigure) with FWHM of 21.5 ps and 2 ps rise/fall times.

of the other machine parameters on the booster on-axis peak field were built in the same way as described in the previous section and are presented in Fig. A.1a-A.1c in Appendix A. As well as for the electron beam with a charge of 1 nC quite small variation of the gun launching phase can be observed for the whole range of the booster on-axis peak field values while the main solenoid current and rms laser spot size on the cathode change significantly.

The emittance dependence on the gun launching phase is presented in Fig. 6.9b. As well as in the case of 1 nC electron beam charge the emittance growth is quite fast with a detuning of the gun launching phase from its optimum value of $\Phi_{\mathrm{g}} = 1.5\,\mathrm{deg}$ with respect to MMMG phase. The dependencies of other parameters on the gun launching phase at which minimum emittance values were found are presented in Fig. A.1d-A.1f. We can observe a strong growth of the optimum booster on-axis peak field and rms laser spot size on the cathode values in both directions from the optimum gun launching phase value while the optimum main solenoid current changes only by $\Delta \mathrm{I}_{\mathrm{main}} = \pm 2\,\mathrm{A}$ for the whole range of tested gun launching phases.

The emittance dependence on the main solenoid current is presented in Fig. 6.9c and yields the minimum emittance value at the main solenoid current of $\mathrm{I}_{\mathrm{main}} = 381\,\mathrm{A}$. Quite strong growth of the emittance can be observed on the right side from the optimum value as well as a strong difference between optimized and tolerance curves. On the left-hand side the emittance growth and difference between optimized and tolerant values are more moderate. The sharp bend at $\mathrm{I}_{\mathrm{main}} = 387\,\mathrm{A}$ is caused by limiting the maximum available booster on-axis peak field to 25 MV/m which is already a bit higher than what can be obtained during experiments. The detailed dependencies of the main solenoid current on the other machine parameters are presented in Fig. A.1g-A.1i. A strong dependence of the optimum booster peak field can be observed. Nevertheless the variation of the optimum booster on-axis peak field around the optimum solenoid current of $\mathrm{I}_{\mathrm{main}} = 381\,\mathrm{A}$ is moderate. As it was mentioned, the maximum on-axis peak field was limited to $\mathrm{E}_{\mathrm{b}}^{\mathrm{p}} = 25\,\mathrm{MV/m}$ which is seen in Fig. A.1i. As well as for simulations of the electron beam with 1 nC bunch charge, gun launching phase variation is quite small in the whole range of the tested main solenoid currents.

The emittance dependence on the rms laser spot size on the cathode is presented in Fig. 6.9d and shows the minimum emittance value at the rms laser spot size on the cathode of $\sigma_{\mathrm{L}} = 0.18\,\mathrm{mm}$. As well as in the 1 nC case the minimum emittance value was found at the rms laser spot size on the cathode close to the space-charge limited extraction and the difference between optimized and tolerance curves is quite small. Dependencies for other machine parameters on the rms laser spot size on the cathode are presented in Fig. A.1j-A.1l. As we can see the variation of the gun launching phase is quite small in the whole range of rms laser spot sizes on the cathode. The optimum booster on-axis peak field increases quite fast with an increasing of the rms laser spot size on the cathode while the main solenoid current variation is only $\Delta \mathrm{I}_{\mathrm{main}} = \pm 2\,\mathrm{A}$ and has a clear plateau part in the range of $\sigma_{\mathrm{L}} = [0.21; 0.29]\,\mathrm{mm}$.

The emittance dependence on the length of the UV laser pulse is presented in Fig. 6.9e. As well as for the 1 nC case the minimum emittance value of $\varepsilon_{\mathrm{n}} = 0.2\,\mathrm{mm\,mrad}$ was found far from the nominal laser pulse length with FWHM = 21.5 ps at the laser pulse length with FWHM = 36 ps. As well as for the simulations with an electron beam of 1 nC charge one can notice about 20% difference between the emittance values at these two laser pulse lengths. Additionally, one has to mention that in the laser pulse length range of [31; 37] ps the emittance stays rather constant. Detailed dependencies of the other machine parameters are presented in Fig. A.2. One can see that optimum booster on-axis peak field stays rather constant in a whole range of optimized laser pulse lengths. The main solenoid current and gun launching phase have a weak dependence and change by $\Delta \Phi_{\mathrm{g}} = \pm 1$ deg and $\Delta \mathrm{I}_{\mathrm{main}} = \pm 1\,\mathrm{A}$ in a whole range of laser pulse durations, respectively. The rms laser spot size on the cathode decreases with an increasing of the laser pulse length as it is expected. As well as for the 1 nC case one can see that the beam volume delivering the minimum emittance value is invariant. Due to the rough steps on the rms laser spot size on the cathode in the simulations one has to fit the obtained data to calculate the charge density more precisely. The obtained charge density value of $\rho_{\mathrm{Q}} = 0.360 \pm 0.012\,\mathrm{nC/(mm^2\,ps)}$ is higher than the corresponding value obtained for the electron beam with 1 nC charge.

6.3.2 Emittance dependencies on various machine parameters at fixed booster on-axis peak field

Simulations for electron beams with a charge of 250 pC, fixed laser pulse length with FWHM = 21.5 ps and 2 ps rise/fall times, fixed gun on-axis peak field of $\mathrm{E}_{\mathrm{g}}^{\mathrm{p}} = 60.5\,\mathrm{MV/m}$ delivering an electron beam momentum after the gun acceleration of about 6.7 MeV/c at MMMG gun launching phase and fixed booster on-axis peak field of $E_b^p = 20\,\mathrm{MV/m}$ delivering an electron beam momentum after the gun and booster acceleration at MMMG phases of about 24.1 MeV/c were performed. The minimum emittance value of $\varepsilon_n = 0.262\,\mathrm{mm\,mrad}$ was found at $\sigma_L = 0.23\,\mathrm{mm}$, $I_{main} = 385\,\mathrm{A}$, $\Phi_g = 1.5\,\mathrm{deg}$ with respect to MMMG phase. The obtained emittance value is about 11 % higher than for the optimum case discussed in the previous section. The electron beam peak current is estimated to be about $I^p = 12.3\,\mathrm{A}$. The corresponding transverse trace space and transverse beam distribution are presented in Fig. 6.10. Emittance dependencies on the remaining machine parameters e.g. gun launching phase, main solenoid current and rms laser spot size on the cathode were studied in more detail. The results of these studies are presented in Fig. 6.11. As we can see the optimized and tolerance curves coincide in a wider ranges than in the case of optimized booster on-axis peak field which shows less sensitivity of the emittance to a possible detuning of the machine parameters from their optimum values during experiments. Additional dependencies of the other parameters are moved to the Appendix A as well as in the previous case and are presented in Fig. A.3. As we can see the dependencies of the other parameters are weaker than in the case of varied

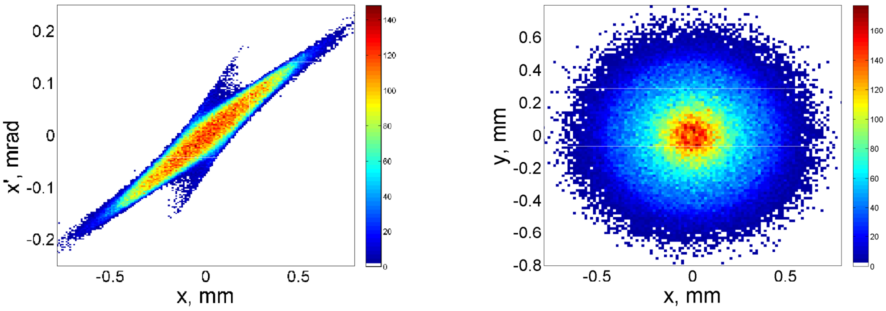

(a) Trace space.

(b) Distribution.

Figure 6.10: Simulated transverse trace space and transverse distribution of the electron beam with 250 pC charge delivering the minimum emittance value at fixed laser pulse length with FWHM of 21.5 ps and 2 ps rise/fall times, fixed gun on-axis peak field of $E_g^p = 60.5\,\mathrm{MV/m}$ and fixed booster on-axis peak field of $E_b^p = 20\,\mathrm{MV/m}$. Colorbars represent the intensity in arbitrary units. Electron beam momentum is about $\langle p_z \rangle = 24.1\,\mathrm{MeV/c}$.

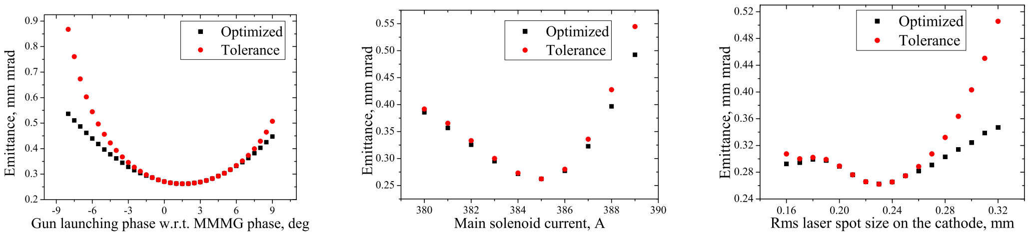

(a) Emittance dependence on the gun launching phase.

(b) Emittance dependence on the main solenoid current.

(c) Emittance dependence on the rms laser spot size on the cathode.

Figure 6.11: Emittance dependencies on different machine parameters for 250 pC electron beam charge, gun on-axis peak field of $E_g^p = 60.5$ MV/m, fixed laser pulse length with FWHM of 21.5 ps and 2 ps rise/fall times and fixed booster on-axis peak field of $E_b^p = 20$ MV/m.

booster on-axis peak field. The optimum laser spot size on the cathode stays constant for a wide range of the gun launching phases of $[-6;8]$ deg while the optimum main solenoid current stays constant in a range of $[-1;6]$ deg as can be seen from Fig. A.3a, A.3b. As we can see from Fig. A.3c, A.3d by changing the main solenoid current the optimum rms laser spot size on the cathode changes significantly up to 20% while the optimum gun launching phase stays almost constant. The optimum gun launching phase and main solenoid current also do not change significantly for the whole range of tested rms laser spot sizes on the cathode as shown in Fig. A.3e, A.3f.

6.4 100 pC charge simulations

For an electron beam with a charge of 100 pC, fixed laser pulse length with FWHM = 21.5 ps including 2 ps rise/fall times and fixed gun on-axis peak field of $E_g^p = 60.5$ MV/m the minimum emittance value of 0.128 mm mrad was found at the main solenoid current of $I_{main} = 379$ A, rms laser spot size on the cathode of $\sigma_L = 0.1$ mm, CDS booster on-axis peak field of $E_b^p = 3$ MV/m and gun launching phase of $\Phi_g = 2$ deg with respect to MMMG phase. The corresponding transverse trace space and transverse beam distribution are presented in Fig. 6.12.

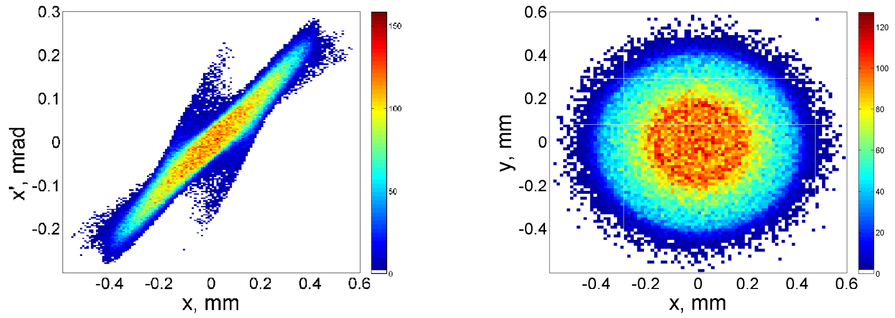

(a) Trace space.

(b) Distribution.

Figure 6.12: Simulated transverse trace space and transverse distribution of the electron beam with 100 pC charge delivering the minimum emittance value at fixed laser pulse length with FWHM of 21.5 ps and 2 ps rise/fall times and fixed gun on-axis peak field of $E_g^p = 60.5\,MV/m$. Colorbars represent the intensity in arbitrary units. Electron beam momentum is about $\langle p_z \rangle = 9.3\,MeV/c$.

6.4.1 Emittance dependencies on various machine parameters including varied booster on-axis peak field

Dependencies of the emittance on the booster accelerating gradient, gun launching phase, main solenoid current and rms laser spot size on the cathode were studied in the same manner as for the other electron beam charges. As usual, dependence on the laser pulse length duration was simulated additionally. The results of the simulations are presented in Fig. 6.13. As the minimum emittance value was found for the booster on-axis peak field of $E_b^p = 3\,MV/m$ an additional set of simulations was done for a fixed booster on-axis peak field of $E_b^p = 20\,MV/m$ as well as in case of 250 pC electron beam charge and is presented in Chapter 6.4.2. As we can see the emittance dependencies on different machine parameters have similar behavior to the results of the simulations for an electron beam with 250 pC charge. One has to notice the further shift of the optimum booster on-axis peak field, main solenoid current and optimum laser pulse length to the smaller values while the optimum gun launching phase moves in positive direction corresponding to a more stretched beam. The detailed dependencies of other parameters

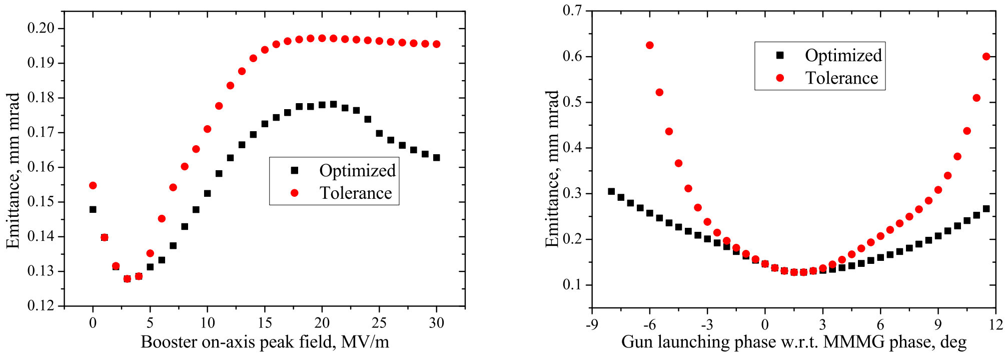

(a) Booster on-axis peak field. (b) Gun launching phase.

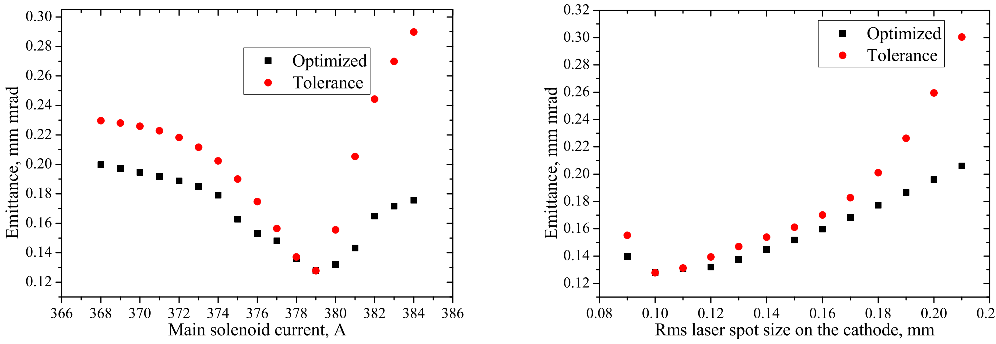

(c) Main solenoid current. (d) Rms laser spot size on the cathode.

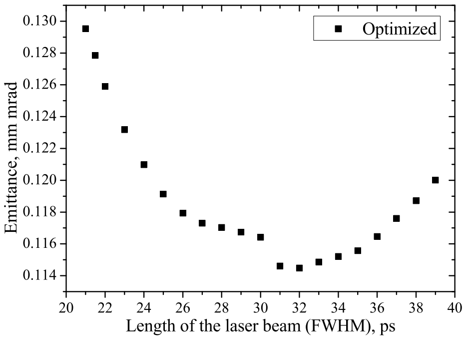

(e) Laser pulse length.

Figure 6.13: Emittance dependencies on different machine parameters for 100 pC electron beam charge, gun on-axis peak field of $E_g^p = 60.5\,\mathrm{MV/m}$, fixed laser pulse length (except last subfigure) with FWHM of 21.5 ps and 2 ps rise/fall times.

are presented in Fig. A.4. As we can see all of them have similar behavior to the corresponding dependencies for 250 pC case which are presented in Fig. A.1. The emittance dependence on the UV laser pulse length is presented in Fig. 6.13e. We can see that the optimum laser pulse length value is shifted further to the left compared to value obtained in the simulations for an electron beam with 250 pC charge. A sudden decrease of the emittance value at the laser pulse length of 31 ps most probably caused by the not precise simulations of the laser pulse length in the range of about [27; 30] ps. Nevertheless the minimum emittance value is expected at laser pulse length with the FWHM of 31 ps. As well as in case of 250 pC bunch charge the variation of other parameters like booster on-axis peak field, gun launching phase and main solenoid current are presented in Fig. A.5 is small while the changing of the rms laser spot size on the cathode is significant. Calculating the optimum beam volume delivering the minimum emittance values in terms of charge density one gets $\rho_{\mathrm{Q}} = 0.483 \pm 0.023\,\mathrm{nC/(mm^2\,ps)}$.

6.4.2 Emittance dependencies on various machine parameters at fixed booster on-axis peak field

As it was mentioned, additional simulations were done for a fixed booster on-axis peak field of 20 MV/m yielding the emittance value of $\varepsilon_{\mathrm{n}} = 0.174\,\mathrm{mm\,mrad}$ which is almost 40 % higher than the emittance value obtained for optimized booster on-axis peak field and presented in previous section. The gun on-axis peak field and laser pulse length were fixed to $\mathrm{E}_{\mathrm{g}}^{\mathrm{p}} = 60.5\,\mathrm{MV/m}$ and 21.5 ps including 2 ps rise/fall times, respectively during these simulations. The other machine parameters delivering the minimum emittance value were found as follows: $\sigma_{\mathrm{L}} = 0.1\,\mathrm{mm}$, $\mathrm{I}_{\mathrm{main}} = 385\,\mathrm{A}$, $\Phi_{\mathrm{g}} = 2.0\,\mathrm{deg}$ with respect to MMMG phase. At this machine setup the electron beam momenta after the gun and booster acceleration at MMMG phases are 6.7 MeV/c and 24.1 MeV/c, respectively. The electron peak current is $\mathrm{I}^{\mathrm{p}} = 5.1\,\mathrm{A}$. The corresponding transverse trace space and transverse beam distribution are presented in Fig. 6.14. Emittance dependencies on the gun launching phase, main solenoid current and rms laser spot size on the cathode were studied in the same manner as described in Chapter 6.3.2. The results of these simulations are presented in Fig. 6.15. As well as for the simulations for the electron beams with 250 pC charge the optimized and tolerance curves coincide in wide range of the rms laser spot sizes on the cathode and main solenoid currents while for the gun

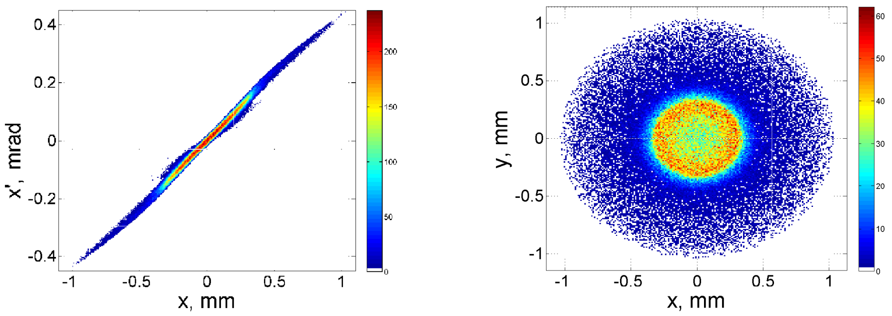

(a) Trace space.

(b) Distribution.

Figure 6.14: Simulated transverse trace space and transverse distribution of the electron beam with 100 pC charge delivering the minimum emittance value at fixed laser pulse length with FWHM of 21.5 ps and 2 ps rise/fall times, fixed gun on-axis peak field of $E_g^p = 60.5\,MV/m$ and fixed booster on-axis peak field of $E_b^p = 20\,MV/m$. Colorbars represent the intensity in arbitrary units. Electron beam momentum is about $\langle p_z \rangle = 24.1\,MeV/c$.

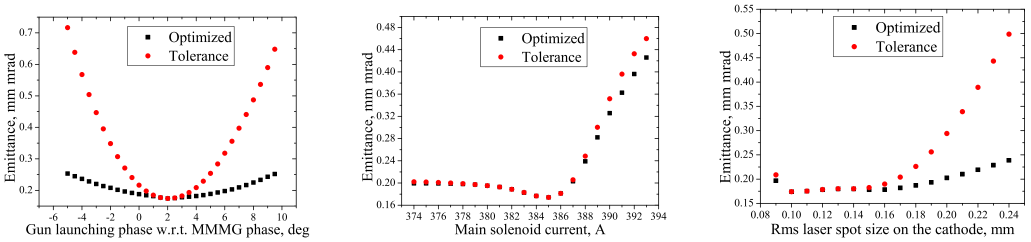

(a) Emittance dependence on the gun launching phase.

(b) Emittance dependence on the main solenoid current.

(c) Emittance dependence on the rms laser spot size on the cathode.

Figure 6.15: Emittance dependencies on different machine parameters for 100 pC electron beam charge, gun on-axis peak field of $E_g^p = 60.5\,MV/m$, fixed laser pulse length with FWHM of 21.5 ps and 2 ps rise/fall times and fixed booster on-axis peak field of $E_b^p = 20\,MV/m$.

launching phase this range is about 2.5 deg. The emittance dependence on the rms laser spot size on the cathode has a wide plateau part in the range of [0.1; 0.18] mm. The dependencies of the other parameters are presented in Fig. A.6 in Appendix A as well as in the previous cases. As we can see these dependencies have similar behavior as the corresponding dependencies for the simulations of the electron beam with 250 pC charge.

6.5 20 pC charge simulations

The minimum emittance value of $\varepsilon_n = 0.041\,\mathrm{mm\,mrad}$ was found for the electron beam with a charge of 20 pC at fixed gun on-axis peak field of $E_g^p = 60.5\,\mathrm{MV/m}$ and fixed laser pulse length with FWHM = 21.5 ps and 2 ps rise/fall times at the following machine parameters: main solenoid current $I_{main} = 376\,\mathrm{A}$, rms laser spot size on the cathode $\sigma_L = 0.035\,\mathrm{mm}$, CDS booster on-axis peak field $E_b^p = 0\,\mathrm{MV/m}$ and gun launching phase $\Phi_g = 2\,\mathrm{deg}$ with respect to MMMG phase. The resulting peak current is $I^p = 1\,\mathrm{A}$. The corresponding transverse trace space and transverse beam distributions are presented in Fig. 6.16. As we can see the minimum emittance value was found with a CDS booster switched off. As it was already mentioned this is not a practical case, further acceleration has to take place. Therefore, as well as in the 250 pC and 100 pC cases, additional simulations were done for a fixed booster on-axis peak field of $E_b^p = 20\,\mathrm{MV/m}$ and are presented in Chapter 6.5.2.

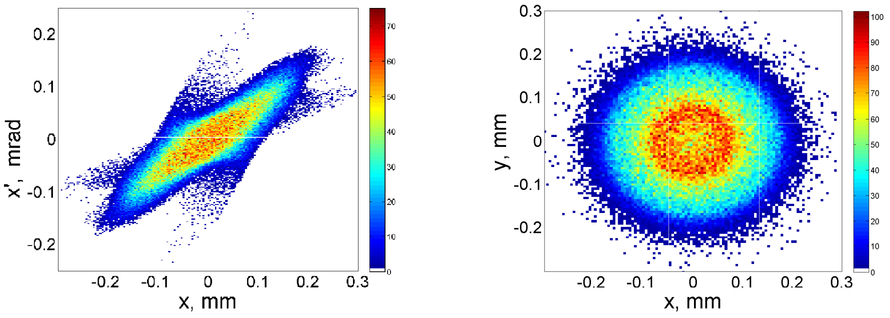

(a) Trace space.

(b) Distribution.

Figure 6.16: Simulated transverse trace space and transverse distribution of the electron beam with 20 pC charge delivering the minimum emittance value at fixed laser pulse length with FWHM of 21.5 ps and 2 ps rise/fall times and fixed gun on-axis peak field of $E_g^p = 60.5\,\mathrm{MV/m}$. Colorbars represent the intensity in arbitrary units. Electron beam momentum is about $\langle p_z \rangle = 6.7\,\mathrm{MeV/c}$.

6.5.1 Emittance dependencies on various machine parameters including varied booster on-axis peak field

As well as in the previous cases emittance dependencies on different machine parameters were studied at fixed laser pulse length with FWHM = 21.5 ps and 2 ps rise/fall times. Simulations of the emittance dependence on the length of the laser beam were performed additionally. The results of the simulations are presented in Fig. 6.17. As we can see the emittance dependencies on different machine parameters have similar behavior to results of 250 pC and 100 pC simulations. One can notice the further shift of the optimum booster on-axis peak field, main solenoid current, rms laser spot size and optimum laser pulse length to the smaller values while the optimum gun launching phase value is the same as in 100 pC case. Additionally, we have to notice that for rms laser spot sizes on the cathode $\sigma_{\mathrm{L}} < 0.035\,\mathrm{mm}$ it is not possible to extract desired charge due to space-charge limited emission. We can also notice that the emittance approaches its maximum for the booster on-axis peak field value of about $\mathrm{E}_{\mathrm{b}}^{\mathrm{p}} = 20\,\mathrm{MV/m}$ which is close to the normal operation point at PITZ and emittance growth at this point is more than 50 % compared to the minimum emittance value. Dependencies of other parameters are presented in Fig. A.7 and are similar to the corresponding dependencies for the simulations with 250 pC and 100 pC electron beam charges. The emittance dependence on the laser pulse length presented in Fig. 6.17e has a plateau part in a wide range of about [21; 32] ps. As we can see the usual laser pulse duration at PITZ of 21.5 ps is at the edge of this plateau region. Other dependencies related to this simulation are presented in Fig. A.8. As we can see there is almost no changes in the optimum booster on-axis peak field, gun launching phase and main solenoid current for the whole range of tested laser pulse lengths. The variation of the optimum laser spot size is also quite moderate and does not exceed 25 %. Calculating the optimum beam volume in the same manner as in the previous cases one gets the optimum charge density of $\rho_{\mathrm{Q}} = 0.803 \pm 0.039\,\mathrm{nC/(mm^2\,ps)}$.

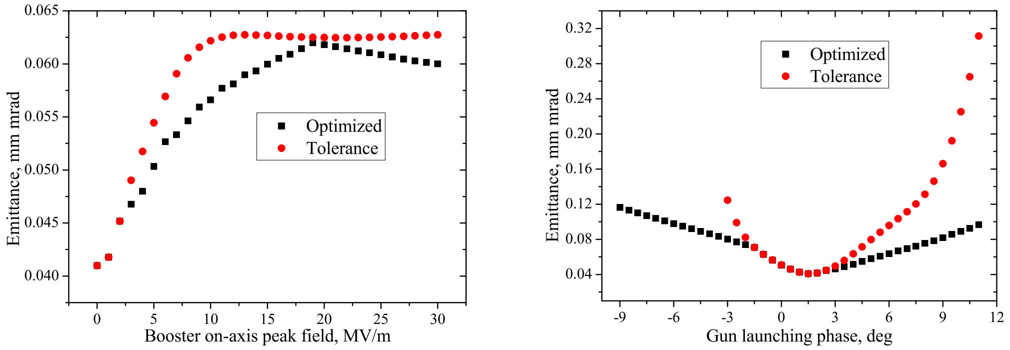

(a) Booster on-axis peak field.

(b) Gun launching phase.

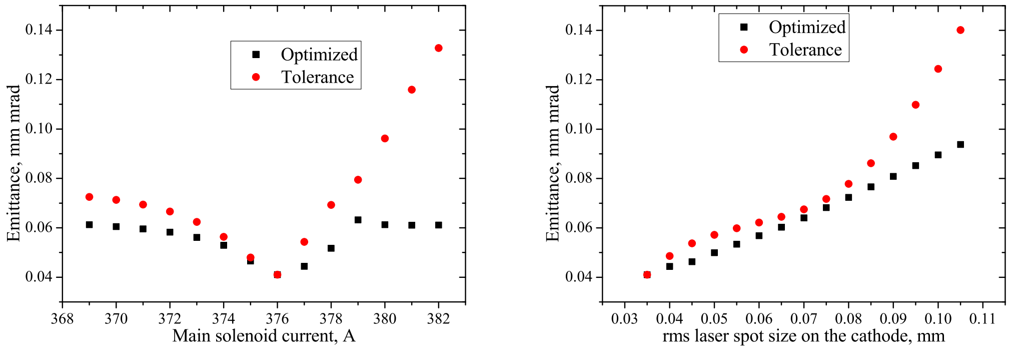

(c) Main solenoid current.

(d) Rms laser spot size on the cathode.

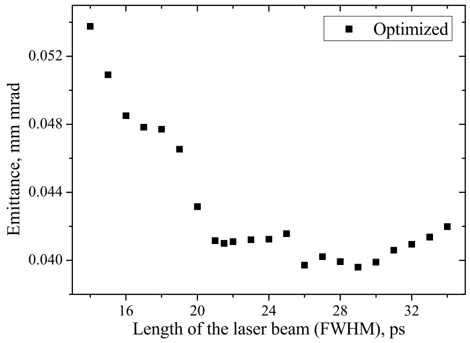

(e) Laser pulse length.

Figure 6.17: Emittance dependencies on different machine parameters for 20 pC electron beam charge, gun on-axis peak field of $E_g^p = 60.5\,\mathrm{MV/m}$, fixed laser pulse length (except last subfigure) with FWHM of 21.5 ps and 2 ps rise/fall times.

6.5.2 Emittance dependencies on various machine parameters at fixed booster on-axis peak field

As well as in the 250 pC and 100 pC cases additional simulations were done for a fixed booster on-axis peak field of 20 MV/m. The minimum emittance value of $\varepsilon_n = 0.062$ mm mrad was found at the following machine parameters: $\sigma_L = 0.035$ mm, $I_{main} = 380$ A, $\Phi_g = 1.5$ deg with respect to MMMG phase. As we can see the value of the optimum laser spot size on the cathode is not changed compared to the case when the booster is switched off. As well as in the corresponding simulations for 250 pC and 100 pC charges the gun on-axis peak field and laser pulse length were fixed to $E_g^p = 60.5$ MV/m and 21.5 ps including 2 ps rise/fall times, respectively. This yields the electron beam momenta after the gun and booster acceleration at MMMG phases of 6.7 MeV/c and 24.1 MeV/c, respectively. The electron peak current does not changes compared to the previously described simulations and is estimated as of $I^p = 1.0$ A. The corresponding transverse trace space and transverse beam distribution are presented in Fig. 6.18. Emittance dependencies on the gun launching phase, main solenoid current and rms laser spot size on the cathode were studied and results are presented in Fig. 6.19. As we can see the optimized and tolerance curves coincide in almost whole range of

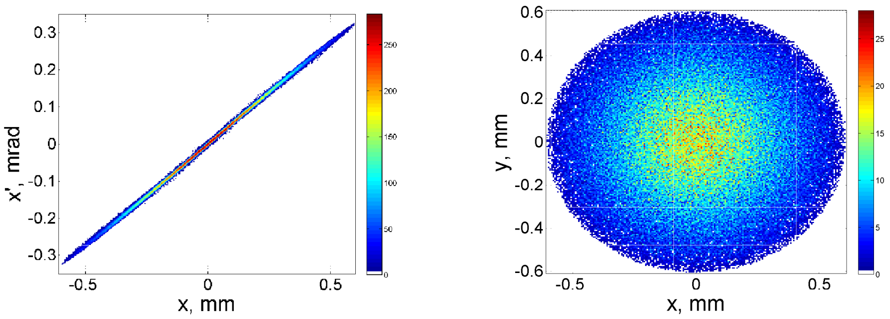

(a) Trace space. (b) Distribution.

Figure 6.18: Simulated transverse trace space and transverse distribution of the electron beam with 20 pC charge delivering the minimum emittance value at fixed laser pulse length with FWHM of 21.5 ps and 2 ps rise/fall times, fixed gun on-axis peak field of $E_g^p = 60.5$ MV/m and fixed booster on-axis peak field of $E_b^p = 20$ MV/m. Colorbars represent the intensity in arbitrary units. Electron beam momentum is about $\langle p_z \rangle = 24.1$ MeV/c.

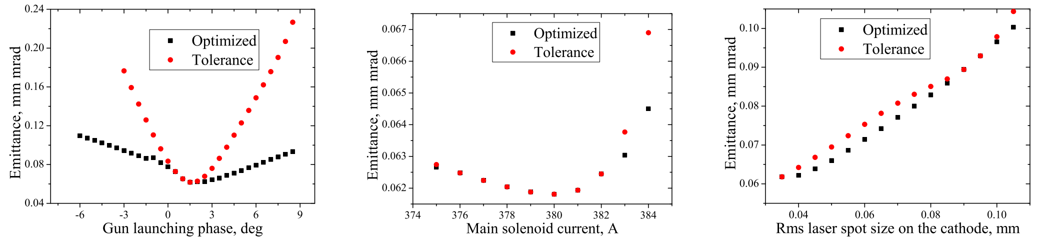

(a) Emittance dependence on the gun launching phase.

(b) Emittance dependence on the main solenoid current.

(c) Emittance dependence on the rms laser spot size on the cathode.

Figure 6.19: Emittance dependencies on different machine parameters for 20 pC electron beam charge, gun on-axis peak field of $E_g^p = 60.5\,MV/m$, fixed laser pulse length with FWHM of 21.5 ps and 2 ps rise/fall times and fixed booster on-axis peak field of $E_b^p = 20\,MV/m$.

the tested main solenoid currents. Both curves representing the emittance dependence on the rms laser spot size on the cathode in Fig. 6.19c have similar slope and quite small difference in the emittance values. The dependencies of other parameters are presented in Fig. A.9. Again we can see that the obtained dependencies are quite similar to the higher charge cases except the dependencies of the gun launching phase and rms laser spot size on the cathode on the main solenoid current which have different bending.

6.6 2 nC charge simulations

Coming back to the high charge operation the emittance dependencies for different machine parameters were also studied for electron beams with 2 nC charge. The minimum emittance value of $\varepsilon_n = 1.138\,mm\,mrad$ was found for fixed gun on-axis peak field of $E_g^p = 60.5\,MV/m$ and fixed laser pulse duration with $FWHM = 21.5\,ps$ including 2 ps rise/fall times. The other machine parameters delivering the minimum emittance value were found as follows: main solenoid current $I_{main} = 387\,A$, rms laser spot size on the cathode $\sigma_L = 0.59\,mm$, CDS booster on-axis peak field $E_b^p = 23\,MV/m$ and gun launching phase $\Phi_g = -1\,deg$ with respect to MMMG phase. The resulting peak current of the beam is about $I^p = 80.3\,A$. The corresponding transverse trace space and transverse beam distribution at the position of EMSY1 are shown in Fig. 6.20. One can notice that the minimum emittance value was

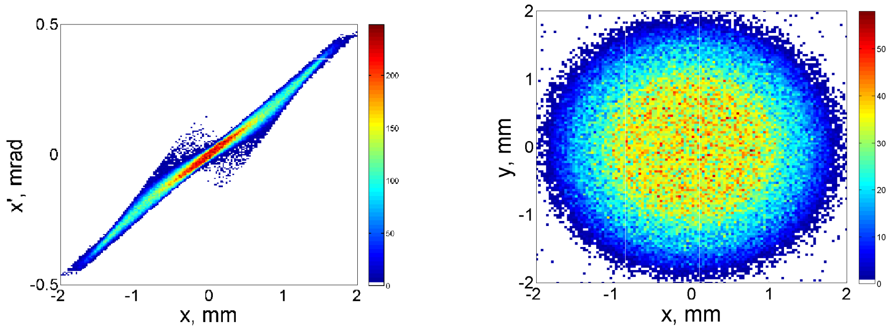

(a) Trace space. (b) Distribution.

Figure 6.20: Simulated transverse trace space and transverse distribution of the electron beam with 2 nC charge delivering the minimum emittance value at fixed laser pulse length with FWHM of 21.5 ps and 2 ps rise/fall times and fixed gun on-axis peak field of $\mathrm{E_g^p} = 60.5\,\mathrm{MV/m}$. Colorbars represent the intensity in arbitrary units. Electron beam momentum is about $\langle \mathrm{p_z} \rangle = 26.7\,\mathrm{MeV/c}$.

found at the booster on-axis peak field of $\mathrm{E_b^p} = 23\,\mathrm{MV/m}$ which corresponds to a final electron beam momentum after the gun and booster acceleration of about 26.7 MeV/c close to the maximum possible during the experiments. Emittance dependencies on different machine parameters are presented in Fig. 6.21. As we can see the emittance dependence on the booster accelerating peak field is quite similar to the 1 nC case and has a plateau part starting from about 17 MV/m. The optimum gun launching phase is shifted to negative direction from the MMMG phase which corresponds to more compressed beam. As can be seen from Fig. 6.21c emittance is strongly dependent on the main solenoid current: a deviation from the optimum value by $\Delta \mathrm{I} = 2\,\mathrm{A}$ increases the emittance by about 10%. Dependencies of other machine parameters are presented in Fig. A.10. As we can see they have similar dependencies as for the 1 nC case. The emittance dependence on the length of the laser beam is presented in Fig. 6.21e and shows the minimum emittance value of $\varepsilon_\mathrm{n} = 0.884\,\mathrm{mm\,mrad}$ at the laser pulse length with FWHM = 40 ps which is close to the 37 ps obtained in case of 1 nC charge. Dependencies of other parameters are presented in Fig. A.11. As we can see they are similar to the 1 nC case and the strong variation of the rms laser spot size on the cathode and booster on-axis peak field can be observed while

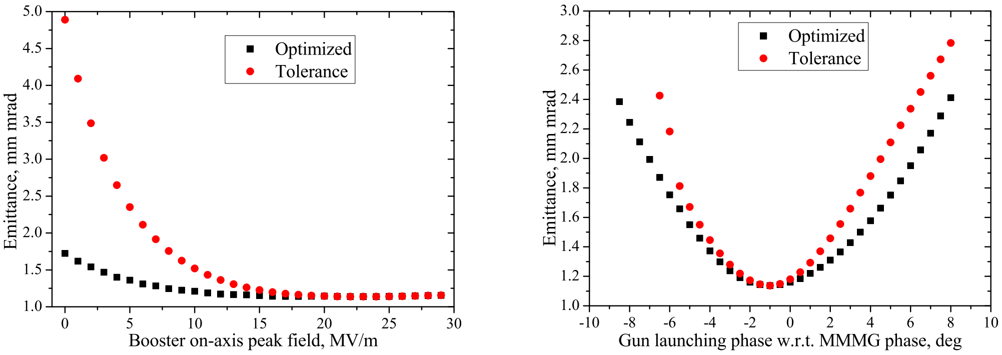

(a) Booster on-axis peak field.

(b) Gun launching phase.

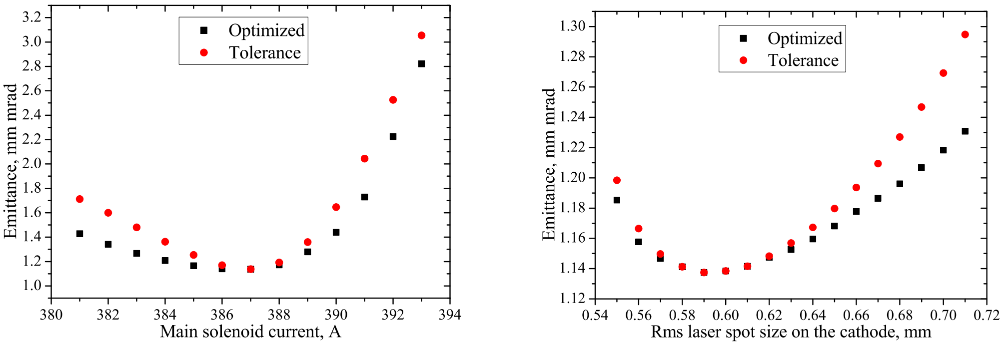

(c) Main solenoid current.

(d) Rms laser spot size on the cathode.

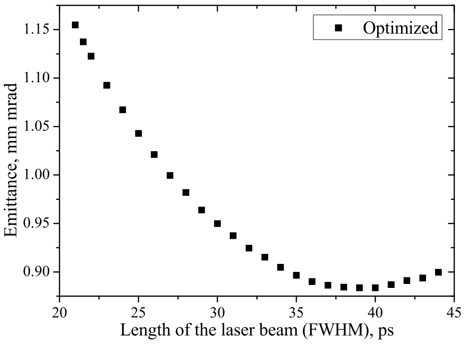

(e) Laser pulse length.

Figure 6.21: Emittance dependencies on different machine parameters for 2 nC electron beam charge, gun on-axis peak field of $E_g^p = 60.5\,\mathrm{MV/m}$, fixed laser pulse length (except last subfigure) with FWHM of 21.5 ps and 2 ps rise/fall times.

the optimum main solenoid current and the gun launching phase almost do not change in the whole range of the tested laser pulse lengths. The optimum beam volume calculated in the same manner as described above yields in terms of charge density to $\rho_{\mathrm{Q}} = 0.281 \pm 0.01\,\mathrm{nC}/(\mathrm{mm}^2\,\mathrm{ps})$

6.7 Summary

Summarized results of the emittance simulations for the electron beam with different charges together with results of the simulations for TESLA type booster cavity, previously used at PITZ, are presented in Fig. 6.22. As described in previous sections the minimum emittance values for the electron beam with a charge of 250 pC and lower were found at reduced CDS booster on-axis peak field values and are not of practical interest. Therefore, the data presented in Fig. 6.22 as results of the simulations with a CDS booster cavity correspond to a fixed CDS booster on-axis peak field of $\mathrm{E}_{\mathrm{b}}^{\mathrm{p}} = 20\,\mathrm{MV/m}$ for electron beams with a charge of $\leq 250\,\mathrm{pC}$. Emittance simulations with a TESLA type booster cavity were preformed based on the results presented in [43]. The TESLA booster on-axis peak field and laser pulse duration were fixed to $\mathrm{E}_{\mathrm{b}}^{\mathrm{p}} = 15\,\mathrm{MV/m}$ and 21.5 ps at FWHM, respectively. As well as in

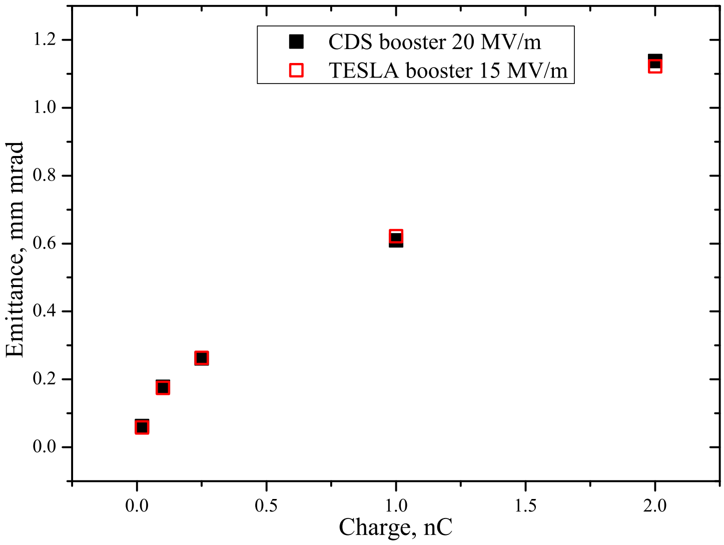

Figure 6.22: Emittance dependence on electron bunch charge for different types of the booster cavity.

simulations with a CDS type cavity, all the simulations were performed at TESLA booster launching phase fixed to MMMG phase. The remaining parameters, e.g. main solenoid current, gun launching phase and rms laser spot size on the cathode, were varied with the same step width as was used in simulations with CDS booster type cavity in order to obtain the minimum emittance values at the position of EMSY1 for each of the electron beam charges. As we can see from Fig. 6.22 the minimum emittance values at the position of EMSY1 for both types of booster cavity are about the same.

In addition to the minimum achievable emittance values for different electron beam charges with different types of the booster cavity, the emittance sensitivity to the different machine parameters is important. In order to study this effect the emittance growth on the detuning of different machine parameters from their optimum values was studied. The results of these investigations are presented in Fig. 6.23 for an electron beam with a charge of 1 nC and in Fig. A.12 for other charges. As we can see for an electron beam of 1 nC charge there is no big difference in emittance behavior for both types of booster cavities. Moreover the CDS booster is more sensitive to the deviation of such machine parameters like rms laser spot size on the cathode and gun launching phase. Sensitivity of the emittance to the detuning of the rms laser spot size on the cathode from its optimum value for the remaining beam charges is about the same for both types of booster cavity except 20 pC charge where the CDS booster shows significantly smaller emittance growth

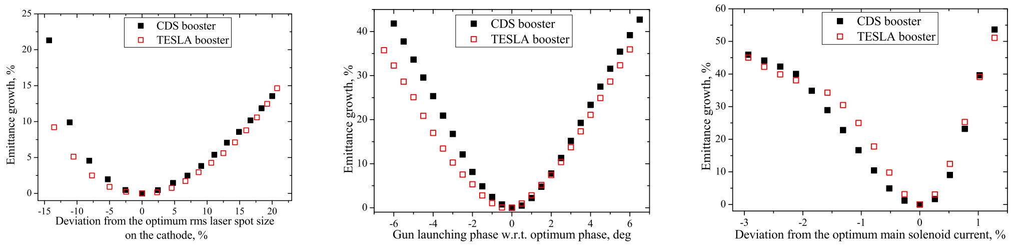

(a) Emittance dependence on the rms laser spot size on the cathode.

(b) Emittance dependence on the gun launching phase.

(c) Emittance dependence on the main solenoid current.

Figure 6.23: Emittance growth as a function of different machine parameters for different types of booster cavities and electron beam with a charge of 1 nC.

compared to the TESLA booster. For all presented electron beam charges except 20 pC, emittance growth caused by the detuning of the gun launching phase from its optimum value is less for the TESLA type booster. As we can see from Fig. 6.23 and A.12 the fastest emittance growth is caused by the detuning of the main solenoid current from its optimum value. Additionally, we have to notice that no clear preference can be given to a certain type of the booster cavity as for 20 pC, 250 pC and 1 nC electron beam charges the emittance growth caused by the detuning of the solenoid current is smaller or comparable for the CDS booster, while for 2 nC and 100 pC the emittance growth is slower at higher values of the main solenoid current from its optimum value for the TESLA type booster. For the values of the main solenoid current smaller than its optimum value, the CDS booster again shows better results than the TESLA one.

As it was shown in previous sections the momentum of the electron beam after the booster acceleration is about 25 MeV/c and 15 MeV/c for the CDS and TESLA boosters, respectively. Despite that the electron beam moves close to the speed of light the influence of the space-charge forces at these energies is significant, especially for high charges, that leads to increase of the emittance. Therefore the emittance conservation after the booster is an important parameter as the electron beam has to be delivered for such diagnostics device as the transverse deflecting cavity, tomography module and HEDA2 which are installed further downstream. In order to investigate the emittance conservation for different types of the booster cavities the electron beams with different charges, delivering the minimum emittance values which are presented in Fig. 6.22, were tracked up to 15 m from the cathode which is about the end of the tomography section. The results of these simulations for the electron beam with 1 nC charge are presented in Fig. 6.24. The results for electron beams with other charges are presented in Fig. A.13. As we can see the emittance is conserved better with the CDS booster for all the tested electron beam charges. Also we have to notice that the real emittance minimum for the simulations with a CDS booster depends on charge and moves downstream with a decreasing of the electron beam charge while for the TESLA booster the emittance minimum is located around the EMSY1 position for all simulated electron beam charges.

Summarizing the aforementioned statements we have to conclude that according to the simulations results, the CDS booster has a practical interest only for PITZ where the emittance conservation after the booster acceleration is important. Also the possibility of the CDS booster to accelerate up to 900

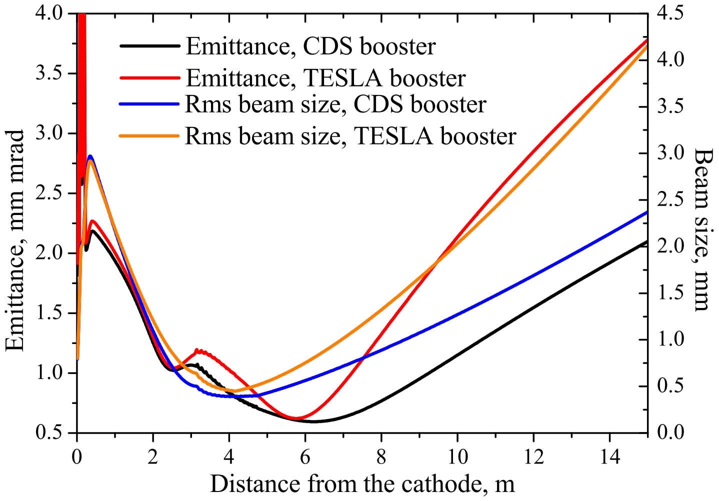

Figure 6.24: Emittance evolution along the PITZ beamline for different types of booster cavities and electron beam with a charge of 1 nC.

laser pulses is important for the low charge operation. Nevertheless, as shown in Chapter 5.2, for the emittance measurements with a charge of 20 pC or lower the capability of the optical readout system is quite low and has to be improved in order to obtain reliable data using slit scan measurement method. Of course we have to also notice that the CDS structure is much less sensitive to any perturbations like, for example, water fluctuations and the following detuning of the resonance condition than the TESLA type booster that implies its easier operation.

Despite that the superconducting TESLA cavities are used at FLASH and will be used at the future European XFEL, presented simulation data can be extrapolated on this facilities. Results of the simulations with the CDS booster of the emittance dependence on the booster on-axis peak field presented in Fig. 6.5a, 6.9a, 6.13a, 6.17a and Fig. 6.21a show that for electron beam with various charges emittance stays nearly constant or even slightly decreases after a certain value of the booster on-axis peak field (about $E_b^p = 20\,MV/m$). Taking into account that simulations with normal conducting TESLA booster yield similar emittance values and that electron beam at FLASH and the European XFEL is accelerated to significantly higher energies, similar emittance values as simulated for PITZ setup can be expected on these facilities (for FLASH it of course assumes exchange of the photocathode UV laser system and increasing of the operating gun on-axis peak fields up to 60.5 MV/m).

Chapter 7

Experimental results

This chapter is dedicated to the analysis of the experimental emittance data collected during the run period 2011 at PITZ. In the following sections emittance data analysis for electron beams with different charges are presented. The largest amount of measurement time was dedicated to studies of the transverse trace space of electron beams with 1 nC charge. For this electron beam charge the detailed studies of the emittance values on such machine parameters like rms laser spot size on the cathode, solenoid field strength, gun launching phase and booster accelerating gradient were performed. For the other charges mainly dependencies of the emittance on such parameters like rms laser spot size on the cathode and main solenoid current were performed. Hereinafter to the end of the chapter, the word ”emittance” is used for normalized transverse projected emittance calculated according to the Eq. 4.3 and Eq. 4.4.

7.1 Emittance measurements for 1 nC beam charge

Electron beams with a 1 nC charge have the highest interest in the experimental investigations at PITZ. Most of the run time is dedicated to the detailed investigations of the trace spaces of such beams as this beam charge is the nominal charge of the electron beams used at such facilities like FLASH and the European XFEL.

7.1.1 Emittance dependence on the rms laser spot size on the cathode

Emittance dependence on the rms laser spot size on the cathode was measured several times during the run period 2011. A flat-top laser temporal distribution with FWHM of 21.5 ps and 2 ps rise and fall times was used. An uniform transverse laser distribution of various diameter was used. The gun accelerating gradient was kept at the maximum possible at that time value of about 60 MV/m and gave an average, over the run, electron beam mean momentum after the gun acceleration of about 6.68 MeV/c at MMMG phase. The booster accelerating gradient was also kept at the maximum possible value and gave the final electron beam mean momentum after gun and booster acceleration of about 24.9 MeV/c for the MMMG phase in the booster (and gun). Several sets of measurements were done during the run period 2011. In the frame of each measurement set the machine conditions were tried to be kept the same. The measurement procedure was the following: for each BSA settings (see Chapter 2.1.2) the MMMG phase at the gun was defined using LEDA (see Chapter 2.4.2). Details about the momentum measurements with the help of spectrometer dipole magnets and determination of the MMMG phase can be found in [15]. The beam charge was set to 1 nC using the Low.ICT1 installed in the low energy section directly downstream the gun (see Chapter 2.4.1). The MMMG phase at the booster was defined using HEDA1 2.4.2. The beam charge was rechecked using the High1.ICT1 installed half a meter downstream the CDS booster (see Chapter 2.4.2). The laser transverse profile was recorded using the VC2 camera (see Chapter 2.1). The longitudinal laser shape was checked using the OSS (see Chapter 2.1). Emittance measurements for both transverse planes using the slit scan technique were performed in a given range of solenoid currents (see Chapter 4.1). The transverse projected emittance is then calculated using Eq. 4.4. The results for the first set of measurements named BSA:N1 are presented in Fig. 7.1

The empty squares in Fig. 7.1 and all the following figures in this chapter represent minimum measured emittance values obtained from the solenoid scan. The filled squares represent average emittance values from some amount (in most cases about 10) of statistical measurements at the main solenoid current delivering the minimum emittance value defined from the solenoid scan. Statistical errors $S(\varepsilon_{n,x})$, $S(\varepsilon_{n,y})$ are calculated for each of the transverse planes separately. Statistical error of the resulted emittance according

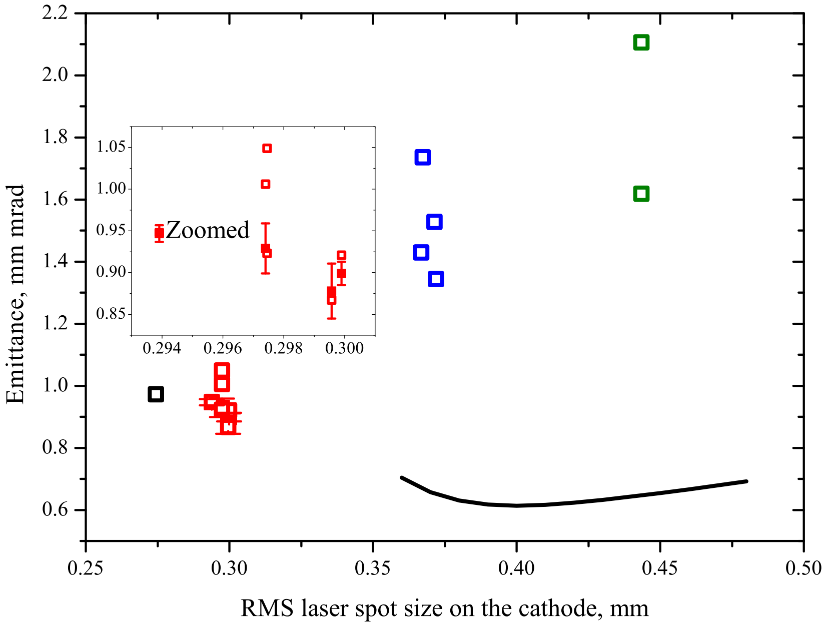

Figure 7.1: Emittance dependence on rms laser spot size on the cathode measured at the position of EMSY1. Colored squares represent measurement data, solid black line corresponds to simulation data. Set of measurements BSA:N1, see text.

to Eq. 4.4 is calculated using the error propagation by the following formula:

$$S(\varepsilon_{n,xy}) = \frac{\varepsilon_{n,xy}}{2}\sqrt{\left(\frac{S(\varepsilon_{n,x})}{\varepsilon_{n,x}}\right)^2 + \left(\frac{S(\varepsilon_{n,y})}{\varepsilon_{n,y}}\right)^2}. \tag{7.1}$$

As we can see from Fig. 1nC:BSA:N1 for each emittance measurement the rms laser spot size at the cathode has small variation around the desired value. The average rms laser spot size on the cathode with its standard deviation is estimated from the analysis of the laser transverse distributions recorded with the help of the VC2 camera.

This very first set of the measurements was performed at the beginning of the run period when the machine setup was not yet optimized. Some optimizations related to the improvement of the longitudinal shape of the laser beam and its transverse profile, as well as electron beam transport trough the beam line were performed between the different measurements presented in this set. The optimization of the electron beam trajectory through the beam line is necessary in order to transport the electron beam in such a way that it enters the booster on axis with zero angle with respect to the Z axis. Otherwise unwanted correlations between transverse momenta for different planes will be obtained during the booster acceleration that will cause increasing of the emittance. Significant discrepancy between the emittance values measured for the same rms laser spot size on the cathode in this set of measurements can be explained by these effects.

For this set of measurements the minimum emittance value of 0.867 mm mrad was measured for the rms laser spot size on the cathode of about 0.300 mm at $I_{main} = 393$ A during the solenoid scan. The gun and booster launching phases were set to the MMMG phases as it was expected to obtain the best emittance values at these phases according to the simulation results (see Chapter 6.2.2). 15 statistical measurements were done for the $I_{main} = 393$ A afterwards and gave the emittance value of 0.878 ± 0.033 mm mrad. As we can see there is a strong difference in the rms laser spot size on the cathode delivering minimum emittance value between experimental measurements and simulations. This difference may be caused by the enhanced charge emission from the cathode surface in the presence of an electric field during experimental measurements which was not taken into account during the simulations. This point will be discussed in more details at the end of this chapter (see Chapter 7.6).

The second set of the measurements named BSA:N2 was done after exchange of the pulse train oscillator of the UV laser system (see Chapter 2.1). The new oscillator brought better pointing stability of the laser beam and better intensity stability. Every time when the size of the BSA is changed, a so-called Beam Based Alignment (BBA) procedure is done in order to avoid unwanted correlations of the transverse electron beam momenta which distort the phase space of the electron beam. The aim of this procedure is to put the laser beam to the position on the photocathode at which the transverse components of the RF field are zero. A jitter of the laser beam on the cathode causes significant impact on the electron beam dynamics in the gun as it correlates to the transverse beam momenta and consequently spoils the emittance of the electron beam. A first effect comes from the pointing stability of the laser beam before the BSA. As with the BSA we cut only a fraction from the whole laser beam, and as the whole laser beam is not fully homogeneous, the quality of the cut beam varies with a jitter of the whole laser beam before the BSA. An example of the whole laser beam transverse distribution and a laser beam with a rms size of about 0.3 mm cut by the

BSA is presented in Fig. 7.2. The white spots over the full laser distribution are signatures of dust on the VC2 camera.

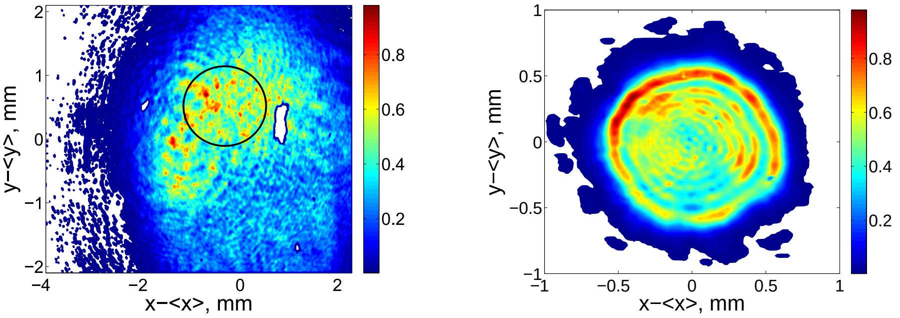

(a) Whole beam has limited homogeneous area on VC2. Black circle corresponds to the position of BSA with rms size of 0.3 mm.

(b) Rms laser spot size 0.3 mm cut by BSA. Difference in the distribution compared to the same area at full laser distribution is caused by interference effects.

Figure 7.2: Laser beam transverse profiles on the VC2, see text.

The jitter of the laser beam transported after the BSA towards the cathode is caused by turbulent airflows in the tunnel (laser beam is transported in air, not in vacuum). To reduce the influence of the airflows on the laser beam, metal beam pipes were installed around the laser beam path. In such a way with a new setup (new laser oscillator and improved laser beam transport system) a reduction of the emittance values was expected. The results of this measurement are presented in Fig. 7.3.

We can see that the minimum emittance value was found for the rms laser spot size on the cathode of about 0.3 mm as well as in the case of BSA:N1. In general, reduction of the emittance values can observed for all tested rms laser spot sizes on the cathode. Still the trend of the obtained curve has a poor agreement with the simulation results. The emittance for a rms laser spot sizes on the cathode of less than 0.3 mm could not be measured as the new pulse train oscillator of the laser system delivered less power of the final UV beam (see Chapter 2.1.1). This made it impossible to extract 1 nC charge for rms laser spot sizes on the cathode smaller than 0.3 mm. The lowest emittance value of 0.763 mm mrad was measured for the rms laser spot size on the cathode of about 0.3 mm at $I_{\mathrm{main}} = 393$ A during the solenoid scan. The gun and booster launching phases were set to MMMG phase as well as for

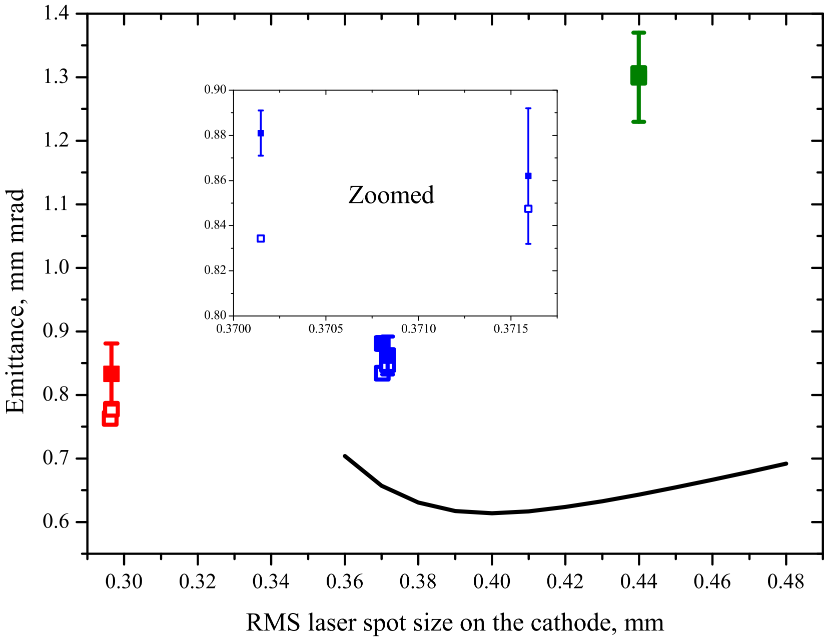

Figure 7.3: Emittance dependence on rms laser spot size on the cathode measured at the position of EMSY1. Colored squares represent measurement data, solid black line corresponds to the simulation data. Set of measurements BSA:N2, see text.

the previous set of measurements. Unfortunately, due to a lack of operational time no statistics was taken during this measurement for the main solenoid current delivering the minimum emittance value. Another measurement was done shortly afterwards and gave a slightly increased emittance value of 0.777 mm mrad at $\mathrm{I}_{\mathrm{main}} = 395\,\mathrm{A}$. 9 statistical measurements for this solenoid current gave the emittance value of 0.833 ± 0.048 mm mrad.

The third set of measurements named BSA:N3 was done after exchange of the $\mathrm{Cs_2Te}$ photocathode. The old cathode with codename 110.2, for which the first two sets of measurements were done, was in operation for about three months. With the third set of measurements the influence on the transverse phase spaces of the electron beam caused by the newly installed cathode with codename 11.3 was investigated. Before the cathode exchange, a quantum efficiency (QE) map of the cathode 110.2 was taken in order to compare it later on with a QE map of the new cathode which was taken soon after its installation into the gun. To perform these measurements the whole surface of the cathode plug is scanned using a laser beam with a small rms spot size of about 0.05 mm. The laser power is reduced so that a mirror charge of the extracted electron beam has no impact on the amount of the extracted electrons. In such a way the amount of extracted electrons are proportional to the laser intensity which is kept constant during the measurement and depends only of the surface properties of the photocathode. To exclude the influence of a possible difference in the surface quality of the in-vacuum mirror, which is used to deflect the laser beam to the photocathode (see Fig. 2.3), the position of the laser beam on it is kept constant during the scan. This is done by simultaneous changing of the orientation of the mirrors M5 and M6 (see Chapter 2.1.2). The QE maps measured for both cathodes are presented in Fig. 7.4. As we can see the QE maps for both photocathodes have similar distributions, but for the new one it is more homogeneous.

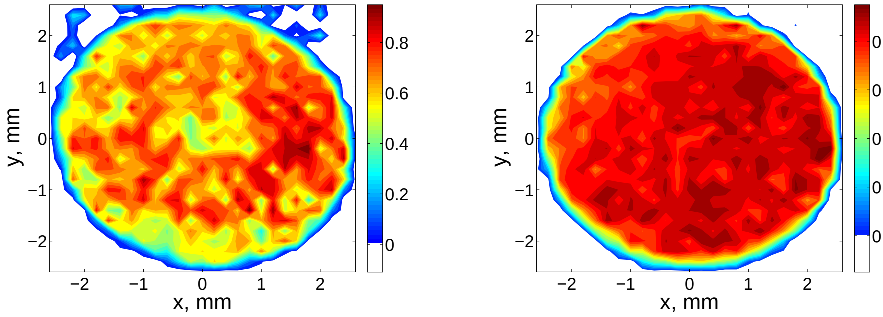

(a) Used cathode 110.2.

(b) Fresh cathode 11.3.

Figure 7.4: Quantum efficiency map measurements of used and newly installed photocathodes. Colorbars represent the intensity in arbitrary units.

The results of the emittance measurements for different rms laser spot sizes on the cathode obtained with the newly installed cathode (codename 11.3) together with corresponding simulations data are presented in Fig. 7.5.

As well as in the previous sets of measurements a minimum emittance value of 0.768 mm mrad obtained from the solenoid scan was found for the rms laser spot size on the cathode of about 0.3 mm far from the 0.4 mm predicted by the simulations. As it was mentioned above some more discussions about this discrepancy can be found at the end of this chapter. 10 statistical measurements taken at the main solenoid current of $I_{\text{main}} = 389\,\text{A}$ representing the minimum emittance value during the solenoid scan gave the

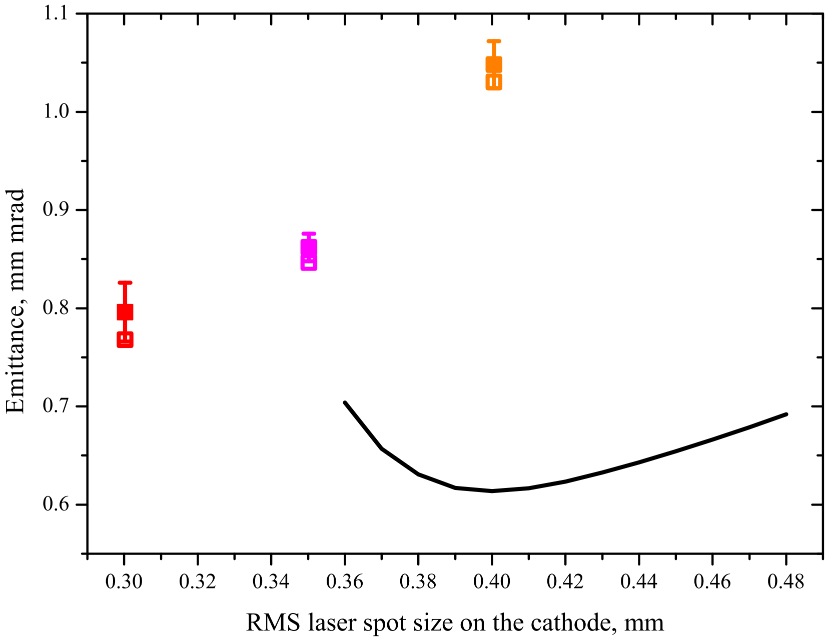

Figure 7.5: Emittance dependence on rms laser spot size on the cathode measured at the position of EMSY1. Colored squares represent measurement data, solid black line corresponds to the simulation data. Set of measurements BSA:N3, see text.

emittance value of 0.796 ± 0.030 mm mrad which is a bit lower than the emittance values obtained with the old cathode (codename 110.2) and more close to the simulations result. In addition just before cathode 110.2 exchange one dedicated emittance measurement was done for the rms laser spot size on the cathode of 0.3 mm. As a results of this measurement the emittance value of 0.777 mm mrad was obtained during the solenoid scan at $I_{main} = 395$ A. 9 statistical measurements at this solenoid current value yielded an emittance value of 0.833 ± 0.050 mm mrad. The laser transverse distributions used for the emittance measurements with both cathodes are presented in Fig. 7.6. In such a way the emittance values obtained with different cathodes are the same within the error bars. Moreover, taking into account that the laser beam used for emittance measurements with the newly installed cathode had a more homogeneous transverse profile, lower emittance values are expected for this cathode. Additionally, we have to notice that such comparison is valid while assuming that the quality of the different cathodes was the same

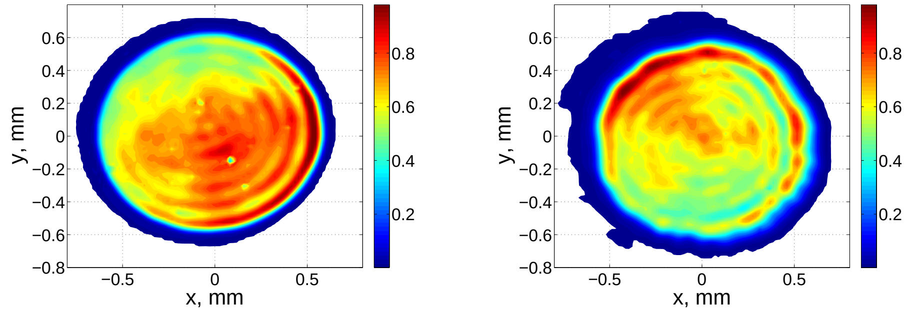

(a) Old cathode. $\sigma_{\mathrm{xy}} = 0.298\,\mathrm{mm}$.

(b) New cathode. $\sigma_{\mathrm{xy}} = 0.300\,\mathrm{mm}$.

Figure 7.6: Laser transverse distributions measured with the help of VC2 camera and used for emittance measurements with used and fresh cathodes.

after the their production which cannot be guarantied. To directly study the effect of the cathode aging one must perform the emittance measurement with a newly installed cathode and later repeat it with the same machine parameters after the intensive usage of the photocathode. This is not the practical case as PITZ is a test facility and a lot of machine parameters and components can be improved on a weekly basis.

Summarizing the emittance data obtained during the measurements the rms laser spot size on the cathode of 0.3 mm can be defined as optimum for the electron beam of 1 nC charge within the scanned step width of about 0.05 mm.

7.1.2 Emittance dependence on the gun launching phase

The emittance dependencies on the gun launching phase were studied for different rms laser spot sizes on the cathode. These studies were done as a part of the program on the emittance dependence on the rms laser spot size on the cathode which is described in the previous section. As well as for the measurements from the previous section the booster accelerating gradient was kept at the value which gave a final electron beam momentum of about 24.9 MeV/c for the MMMG phases in the CDS booster and gun. The measurement procedure is the same as described in Chapter 7.1.1. The emittance dependence on the gun launching phase for the rms laser spot size on the cathode of 0.275 mm is presented in Fig. 7.7 and corresponds to set of measurements BSA:N1 described in Chapter 7.1.1.

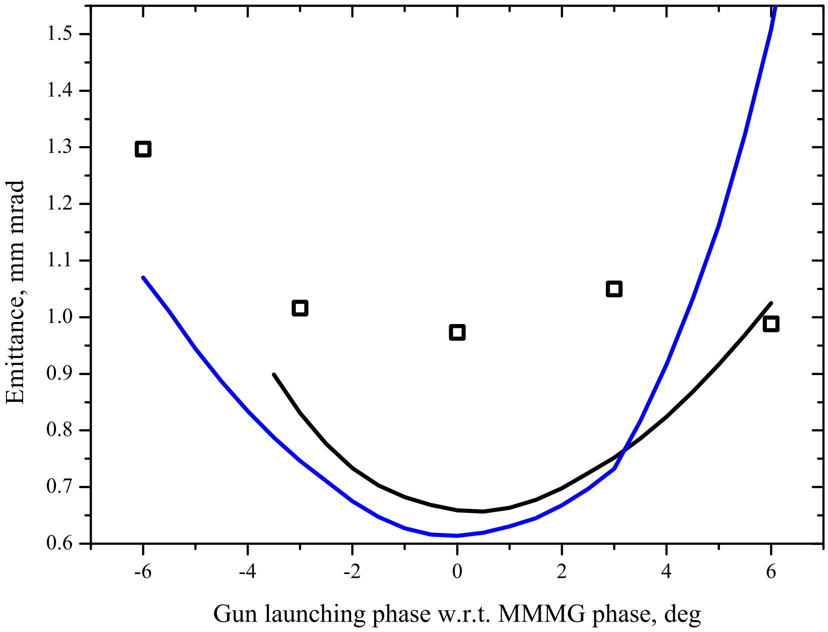

Figure 7.7: Emittance dependence on the gun launching phase at the position of EMSY1 for the rms laser spot size on the cathode of 0.275 mm. Black squares represent measurements data, colored solid lines - simulations data. Set of measurements Phi1:N1, see text.

The absolute minimum emittance value of 0.973 mm mrad was measured at the MMMG gun launching phase at $I_{\mathrm{main}} = 394$ A during the solenoid scan. No statistical measurements was taken for any of the tested gun launching phases. In general for this measurement the emittance values in the phase range $[-3; 6]$ deg are quite close to each other. The standard deviation between them is only 0.029 mm mrad that is equal to 2.9%. As it was discussed in previous section it is not possible to extract 1 nC charge for this rms laser spot size on the cathode during the simulations. Therefore the solid blue line in Fig. 7.7 represents the results of the simulation with the rms laser spot size on the cathode of 0.4 mm at which minimum emittance value was found. The solid black line in Fig. 7.7 represents the simulations with the rms laser spot size on the cathode of 0.37 mm which is about 8 % less than the optimum value, as well as the experimentally used 0.275 mm less than experimentally measured optimum value of 0.3 mm by about the same 8 %.

As we can see there is a significant discrepancy between the measured and simulated emittance values. In general it has to be considered that this measurement was done at the beginning of the run period when the machine settings were not yet optimized as it was mentioned earlier. Nevertheless the emittance dependence on the gun launching phase is significantly stronger in simulations than one obtained during experimental measurements.

For the rms laser spot size at the cathode of 0.3 mm three sets of emittance measurements for different gun launching phases corresponding to the measurement sets BSA:N1-BSA:N3 were done. The results of the first set of measurements are presented in Fig. 7.8. As well as on previous figures of such type the empty squares represent minimum measured emittance values obtained from the solenoid scan. The filled squares represent average emittance values from statistical measurements at the main solenoid current delivering the minimum emittance value defined from the solenoid scan.

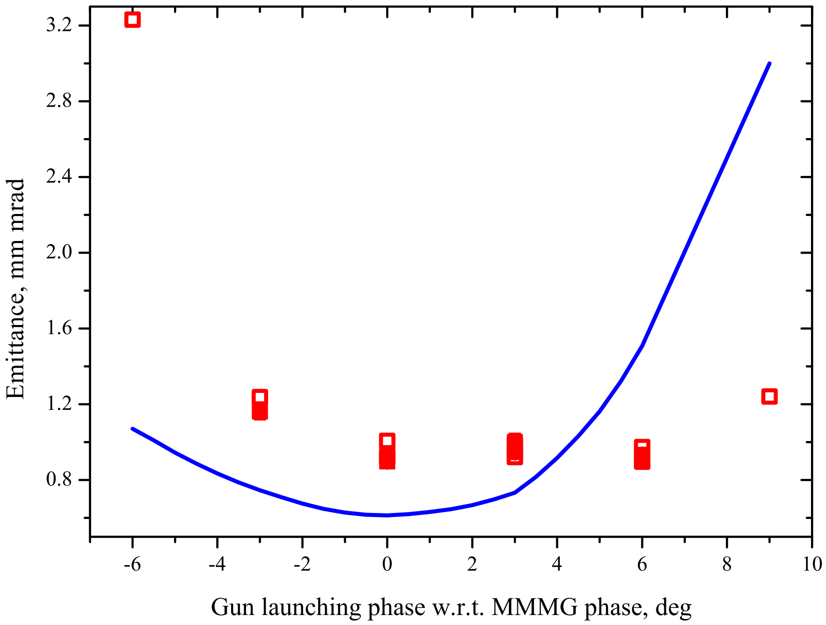

Figure 7.8: Emittance dependence on the gun launching phase at the position of EMSY1 for the rms laser spot size on the cathode of 0.3 mm. Red squares represent measurements data, error bars are hidden within the marker size. Blue solid line represents simulations data. Set of measurements Phi2:N1, see text.

The gun launching phase delivering the minimum emittance value cannot be well defined from this measurement. The absolute minimum emittance value of 0.896 mm mrad was found at the main solenoid current of $I_{\mathrm{main}} = 393\,\mathrm{A}$ during the solenoid scan at the gun launching phase of 6 deg for this set of measurements. 6 statistical measurements at this point gave the emittance value of 0.904 ± 0.022 mm mrad. As we can see in the phase range $[0; 6]$ deg the emittance values stay rather constant within the statistical error bars, while the gun launching phases -6, -3 and 9 deg give significantly higher emittance numbers. In such a way we can guess that the phase corresponding to the minimum emittance value is located in the phase range $[0; 6]$ deg. As well as in previous case it was not possible to extract 1 nC of charge for this rms laser pot size on the cathode during the simulations. Therefore, blue solid line in Fig. 7.8 represents the simulations with the rms laser spot size on the cathode of 0.4 mm which gives the minimum emittance value during the simulations, as well as the rms laser spot size on the cathode of 0.3 mm gave minimum emittance values during the measurements. We can see that here is a considerable difference between the measured and simulated values. Moreover, emittance growth faster in the negative direction of gun launching phase during the measurements while during the simulations emittance growth faster for positive phases.

The second set of measurements taken for the rms laser spot size on the cathode of 0.3 mm corresponding to BSA:N2 was performed after exchanging of the pulse train oscillator as it is described in Chapter 7.1.1. The results of this measurement are presented in Fig. 7.9. Due to a lack of operational time, the emittance was measured only for two gun phases of the highest interest: MMMG phase as a phase delivering the best emittance value according to the ASTRA simulations (see Chapter 6.2.2) and 6 deg as a phase delivering the best emittance value evaluated from the rough analysis of the experimental data since the beginning of the run period. The best emittance value of 0.661 ± 0.046 mm mrad for 1 nC electron beam charge during the whole run period was measured at the gun launching phase of 6 deg in the frame of this measurement and will be described in more details in Chapter 7.1.3. The blue solid line in Fig. 7.9 representing simulations results is the same as presented in Fig. 7.9. In this case we can see that discrepancy between the simulated and measured emittance values for the gun launching phase of 6 deg is stronger than in previous case.

The third set of measurements is presented in Fig. 7.10. The minimum emittance value of 0.778 ± 0.022 mm mrad was found at the gun launching

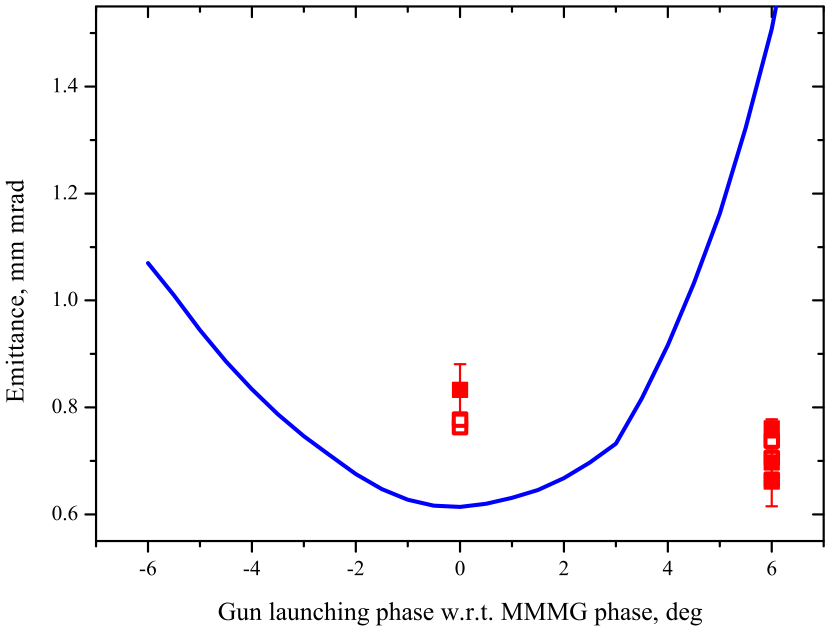

Figure 7.9: Emittance dependence on the gun launching phase at the position of EMSY1 for rms laser spot size on the cathode of 0.3 mm. Red squares represent measurements data, error bars for some points are hidden within the marker size. Blue solid line represents simulations data. Set of measurements Phi2:N2, see text.

phase of 3 deg with respect to the MMMG phase at $I_{main} = 391$ A within the 10 statistical measurements. For the MMMG gun launching phase an emittance value of 0.796 ± 0.030 mm mrad was measured at $I_{main} = 389$ A during the 10 statistical measurements. Emittance values for other gun launching phases are higher. In such a way the gun launching phase range of [0; 3] deg can be defined as providing the minimum emittance value. As well as in previous cases there is a considerable difference between the measurements data and simulations represented by blue solid line in Fig. 7.10.

The emittance dependencies on the gun launching phase for other rms laser spot sizes on the cathode were studied not so intensively as for the rms laser spot size on the cathode of 0.3 mm. The emittance dependence on the gun launching phase for the rms laser spot size on the cathode of 0.35 mm is presented in Fig. 7.11. As it was found during the studies of the emittance dependence on the gun launching phase for the rms laser spot

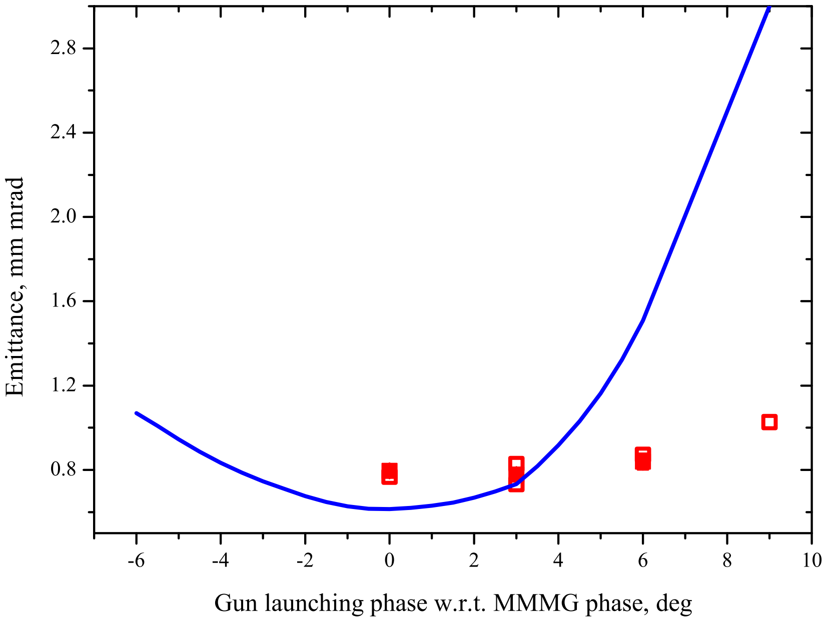

Figure 7.10: Emittance dependence on the gun launching phase at the position of EMSY1 for rms laser spot size on the cathode of 0.3 mm. Red squares represent measurements data, error bars are hidden within the marker size. Blue solid line represents simulations data. Set of measurements Phi2:N3, see text.

size on the cathode of 0.3 mm the minimum emittance value is located in a phase range of [0; 6] deg, only this range was probed during the experiments. The minimum emittance value of 0.804 ± 0.022 mm mrad was calculated out of 10 statistical measurements taken at a main solenoid current value of $I_{main} = 390$ A for the gun launching phase of 3 deg with respect to MMMG phase. The minimum emittance values for other gun launching phases were found also for $I_{main} = 390$ A out of 10 statistical measurements and only about 8% higher than for the optimum gun launching phase. In such a way taking into account systematical errors possible during the measurements it is not possible to define the gun launching phase delivering the minimum emittance from this measurement as well as in the previous measurements. Nevertheless we still can guess that it is located within the gun launching phase range of [0; 6] deg. For this rms laser spot size on the cathode it was still not possible to extract 1 nC charge in simulations. Therefore the blue solid line in Fig. 7.11

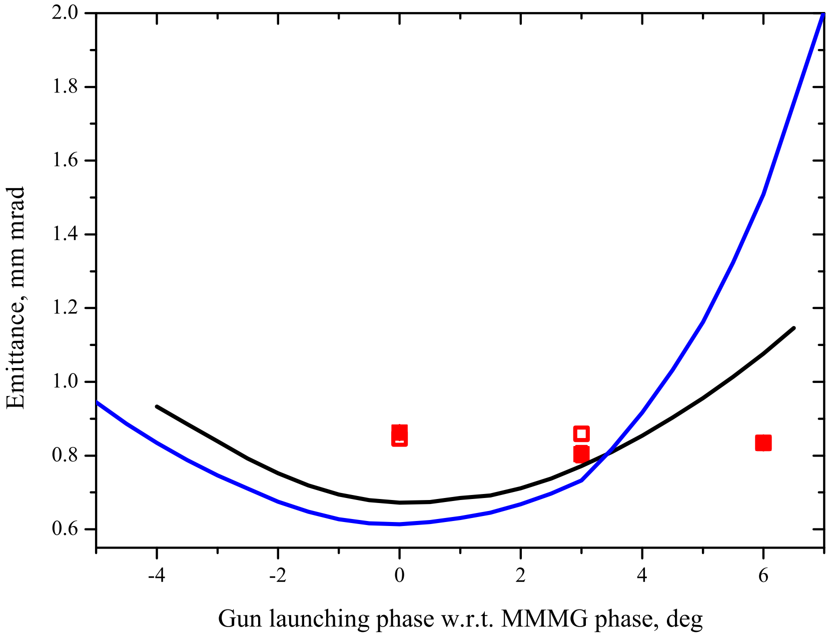

Figure 7.11: Emittance dependence on the gun launching phase at the position of EMSY1 for rms laser spot size on the cathode of 0.35 mm. Red squares represent measurements data, error bars are hidden within the marker size. Solid lines represent simulations data, see text.

represents the simulations for the rms laser spot size on the cathode of 0.4 mm as well as on previous figures. The solid black line in Fig. 7.11 represents the simulations with the rms laser spot size on the cathode of 0.47 mm which is about 17 % higher than the optimum value, as well as the experimentally used 0.35 mm higher than experimentally measured optimum value of 0.3 mm by about the same 17 %. As well as for other rms laser spot sizes on the cathode we can see fairly weak agreement between the simulations and measurements results and stronger dependence of the emittance on the gun launching phase during the simulations.

Emittance dependence on the gun launching phase for the rms laser spot size on the cathode of 0.375 mm is presented in Fig. 7.12. As it can be seen only three gun launching phases were tested for the minimum emittance value. The minimum emittance value of 0.754 mm mrad was measured during the solenoid scan for the gun launching phase of 6 deg with respect to MMMG phase at a main solenoid current value of $I_{main} = 390$ A. 9 statistical measurements taken at $I_{main} = 390\,A$ yield the emittance value of 0.766 ± 0.017 mm mrad. For the other tested gun launching phases the emittance values are more than 10 % higher. Unfortunately no measurements for higher gun launching phases were done. In such a way the gun launching phase of 6 deg with respect to MMMG phase is the most bright candidate to be the optimum phase for the rms laser spot size on the cathode of 0.375 mm. Two solid lines represent simulations data in Fig. 7.12. The red line corresponds to the simulations with the rms laser spot size on the cathode of 0.375 mm and is limited at the negative phase direction due to impossibility to extract desired charge for lower gun launching phase values. The black line in Fig. 7.12 represents the simulations with the rms laser spot size on the cathode of 0.5 mm which is 25 % higher than the optimum value of 0.4 mm, as well as the experimentally used 0.375 mm higher than experimentally measured optimum value of 0.3 mm by the same 25 %.

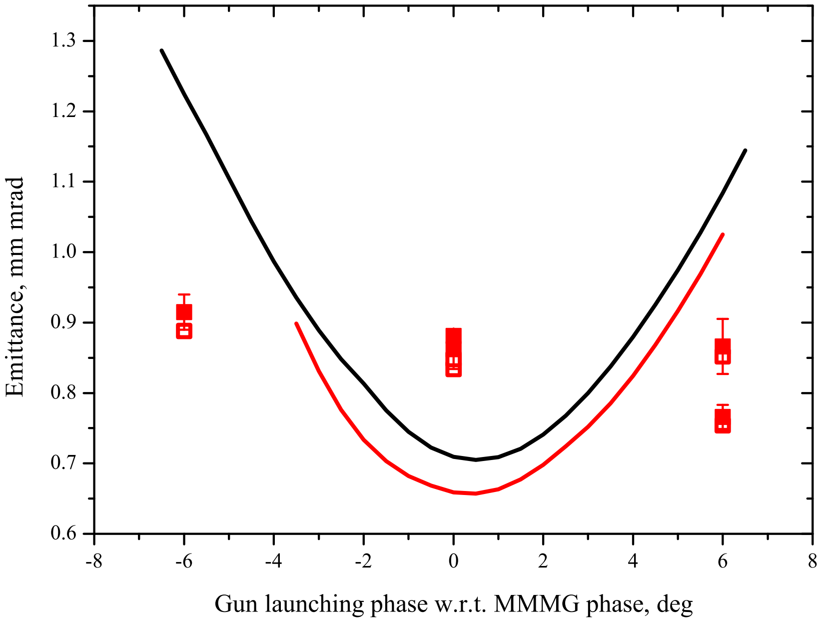

Figure 7.12: Emittance dependence on the gun launching phase at the position of EMSY1 for rms laser spot size on the cathode of 0.375 mm. Red squares represent measurements data, error bars for some points are hidden within the marker size. Solid lines represent simulations data, see text.

Summarizing the data about emittance dependencies on the gun launching phase obtained for different rms laser spot sizes on the cathode several conclusions can be made. The emittance dependencies on the gun launching phase is fairly weak for the tested range of rms laser spot sizes on the cathode and the gun launching phase range of $[0, 6]$ deg with respect to MMMG phase. Due to this weak dependence, the limited measurements time, systematical errors of the measured emittance values caused by detuning of such machine parameters like homogeneity of the laser transverse shape and distortions in the longitudinal laser shape as well as uncertainties in the determination of the optimum solenoid current, optimum booster launching phase and other parameters make it impossible to precisely define the optimum gun launching phase for any of the tested rms laser spot sizes on the cathode. Nevertheless for all the tested rms laser spot sizes on the cathode the phase range of $[0; 6]$ deg can be determined as delivering the optimum emittance values. Emittance dependencies on the gun launching phase for different rms laser spot sizes on the cathode obtained during the simulations have a fairly weak agreement with the measured ones.

7.1.3 Best emittance value measured for the electron beam of 1 nC charge during the whole run period

The minimum emittance value for 1 nC was measured in the frame of the studies of emittance dependence on the gun launching phase as it was mentioned in the previous section. The measurement was done for the rms laser spot size on the cathode of 0.299 mm, a flat-top temporal laser profile with FWHM of 21.5 ps and 2.3 / 2.6 ps rise/fall times, gun launching phase of 6 deg with respect to MMMG phase. Corresponding laser temporal and transverse distributions are presented in Fig. 7.13. The electron beam momentum after the gun was measured using LEDA. The electron beam momentum dependence on the gun launching phase during a rough scan with 50 frames taken for each gun setpoint phase is presented in Fig. 7.14a. From this data the setpoint phase of 6 deg which has arbitrary offset depending on the LLRF settings from the physical phase was determined as the MMMG phase. Additional 200 statistical measurements at the MMMG phase yield a mean electron beam momentum of 6.688 ± 0.002 MeV/c and a momentum spread of 18.997 ± 0.895 keV/c. At a gun phase of 6 deg with respect to the MMMG phase (and corresponds to the setpoint phase of 12 deg in Fig. 7.14a) a mean electron beam momentum of 6.674 ± 0.001 MeV/c and a momentum spread

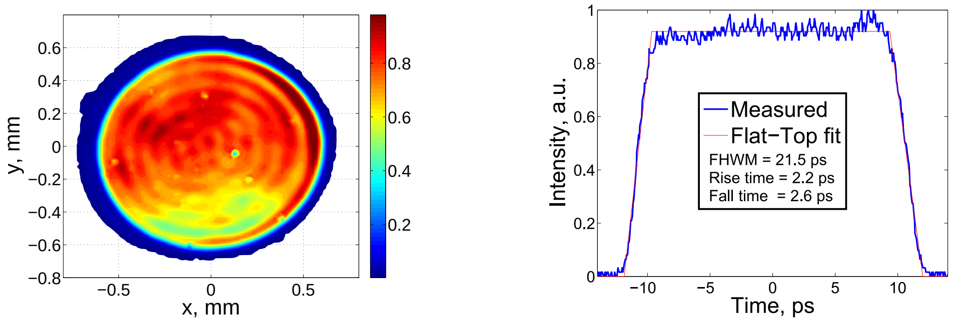

(a) Transverse laser distribution on VC2 camera. $\sigma_{\mathrm{x}} = 0.309\,\mathrm{mm}$, $\sigma_{\mathrm{y}} = 0.290\,\mathrm{mm}$.

(b) Temporal laser distribution fitted with a flat-top function.

Figure 7.13: Laser beam distributions used during the measurement resulted the best emittance value at the position of EMSY1 over whole run period for the electron beam with a charge of 1 nC.

of $40.209 \pm 1.080\,\mathrm{keV/c}$ was calculated from 200 statistical measurements. The momentum distributions at both gun launching phases are presented in Fig. 7.14b and Fig. 7.14c, respectively. The final electron beam momentum after the CDS booster acceleration was measured using HEDA1. The measured electron beam mean momentum and momentum spread dependencies on the booster launching phase are presented in Fig. 7.15a. From the collected data, with 50 frames taken at each booster phase, the booster setpoint phase of 152 deg was defined as the MMMG phase. Additional 200 statistical measurements at this phase yield the momentum distribution presented in Fig. 7.15b with a mean electron beam momentum of $24.669 \pm 0.004\,\mathrm{MeV/c}$ and a momentum spread of $68.645 \pm 3.245\,\mathrm{keV/c}$. The electron beam charge was measured using High1.ICT1 located 0.5 m downstream the CDS booster. The result of 100 statistical measurements is presented in Fig. 7.16 and yield the electron beam charge of $1.024 \pm 0.023\,\mathrm{nC}$.

The emittance value of 0.665 mm mrad was obtained from the solenoid scan at $\mathrm{I_{main}} = 396\,\mathrm{A}$ as it is shown in Fig. 7.17. 9 statistical measurements taken at this solenoid current are presented in Fig. 7.18 and gave an emittance value of 0.661 ± 0.046 mm mrad which is quite below the 0.9 mm mrad required by the European XFEL. As it was mentioned, during the simulations it is not possible to extract 1 nC with the nominal ASTRA setup. There-

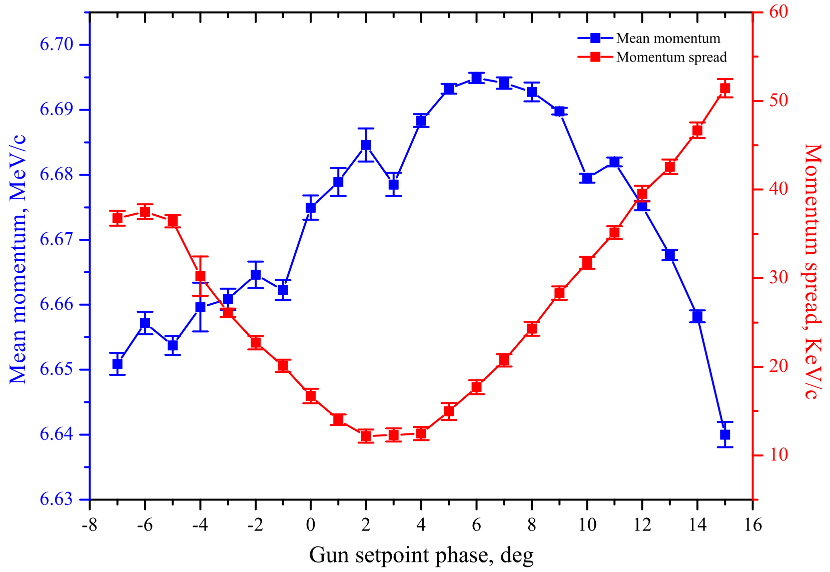

(a) Electron beam momentum scan in LEDA.

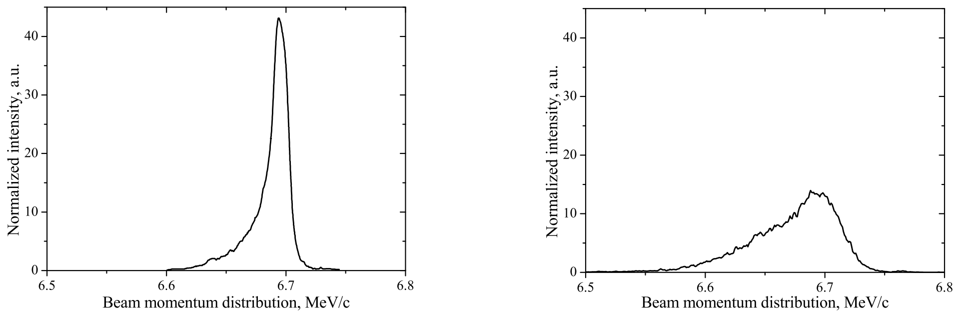

(b) Electron beam momentum distribution at the MMMG gun launching phase.

(c) Electron beam momentum distribution at the (MMMG+6) deg gun launching phase.

Figure 7.14: Electron beam momentum scan using LEDA.

fore, the results of the simulations at which minimum emittance value was found (rms laser spot size on the cathode of 0.4 mm, MMMG gun launching phase) are presented for comparison. Despite significant discrepancy between machine parameters delivering minimum emittance values obtained during the simulations and measured ones, emittance curves have relatively good agreement. Additionally, a part of discrepancy between the measured and simulated optimum main solenoid current values may be caused by a rela-

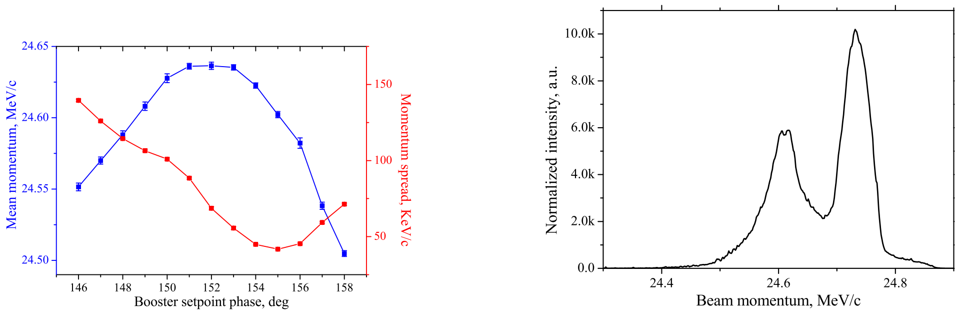

(a) Electron beam momentum scan changing the CDS booster phase.

(b) Electron beam momentum distribution at the MMMG phase in the CDS booster.

Figure 7.15: Electron beam momentum scan measured in HEDA1.

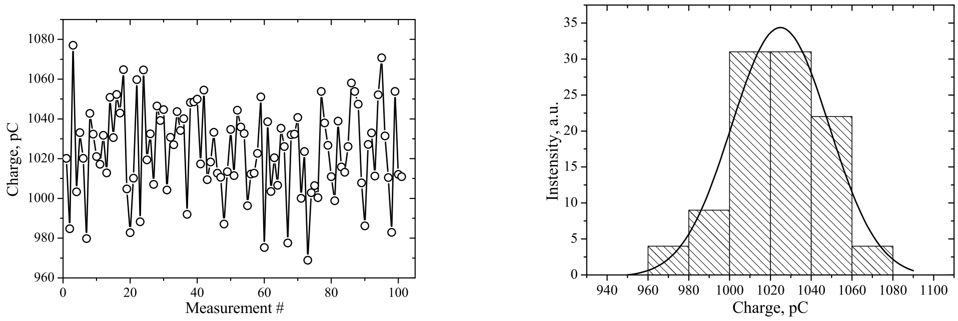

(a) Raw data.

(b) Charge distribution.

Figure 7.16: Charge measurement using High1.ICT1.

tively poor quality of the solenoid field profile measurements (more discussion about this discrepancy can be found at the end of this chapter).

An example of the trace spaces for the both transverse plains obtained from one of the statistical measurements and delivering $\varepsilon_{\mathrm{n,x}} = 0.727\,\mathrm{mm\,mrad}$ and $\varepsilon_{\mathrm{n,y}} = 0.608\,\mathrm{mm\,mrad}$ which gives $\varepsilon_{\mathrm{n,xy}} = 0.665\,\mathrm{mm\,mrad}$ together with the transverse electron beam profile at the position of EMSY1 is presented in Fig. 7.19.

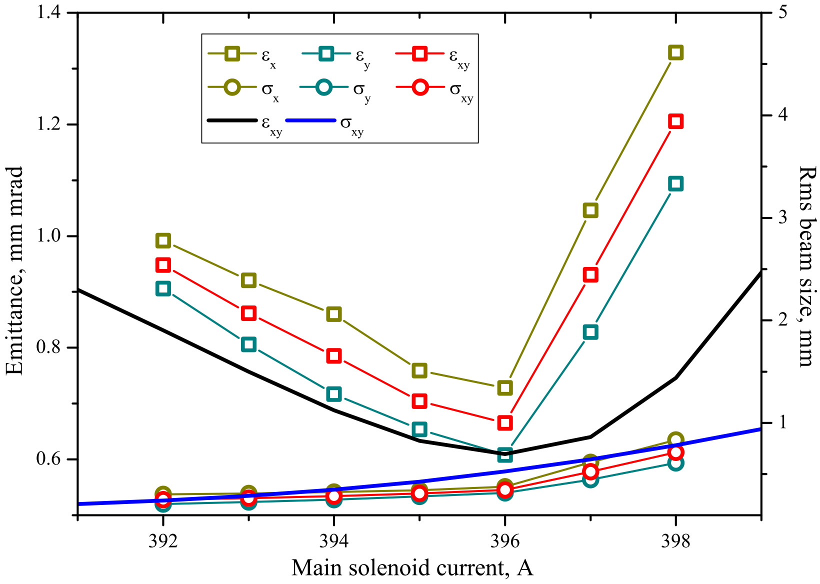

Figure 7.17: Measurement delivering the minimum emittance value over the whole run period for the electron beam with a charge of 1 nC at the position of EMSY1. Solenoid scan. Connected squares represent measurements data, solid lines represent simulations data. Abscissa axis for the simulation data is artificially shifted by +10 A for comparison, see text.

7.1.4 Emittance dependence on the booster accelerating gradient

The emittance dependence on the booster accelerating gradient is shown in Fig. 7.20. Each emittance measurement point in Fig. 7.20 was obtained as the mean value from statistical measurements at fixed main solenoid current defined as delivering the minimum emittance value during the solenoid scan. The value of the solenoid current at which the minimum emittance value was obtained is also shown for each CDS booster accelerating gradient and has a good qualitatively agreement with the simulation data (see Chapter 6.2.2). The same optimum solenoid current obtained for the two last points on the right side can be explained by a relatively small booster gradient change and that fact that the step during the solenoid scans was 1 A. Other machine parameters were set as follows. The gun launching phase was set to MMMG phase during this measurements. Also the CDS booster launching phase was

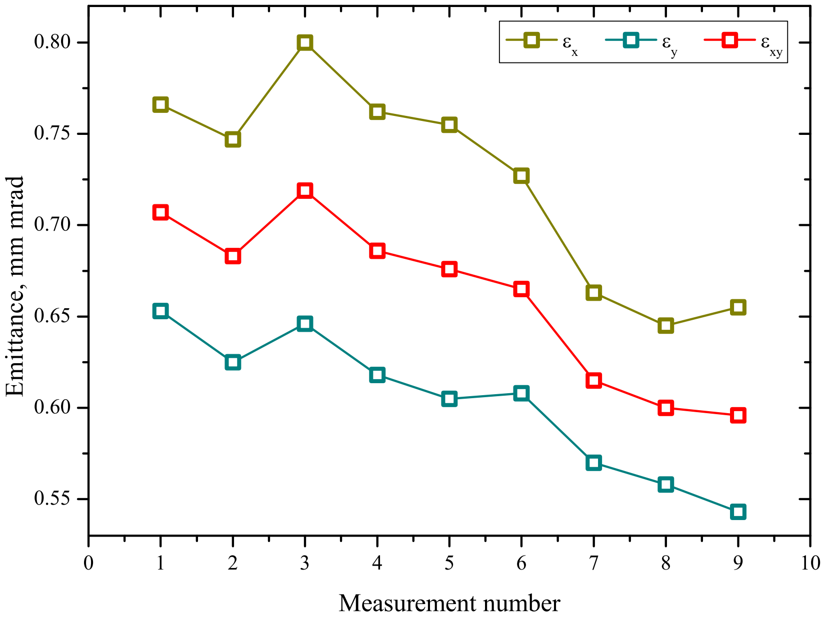

Figure 7.18: Measurement delivering the minimum emittance value over the whole run period for the electron beam with a charge of 1 nC at the position of EMSY1. Statistical measurement at $I_{\mathrm{main}} = 396\,\mathrm{A}$

.

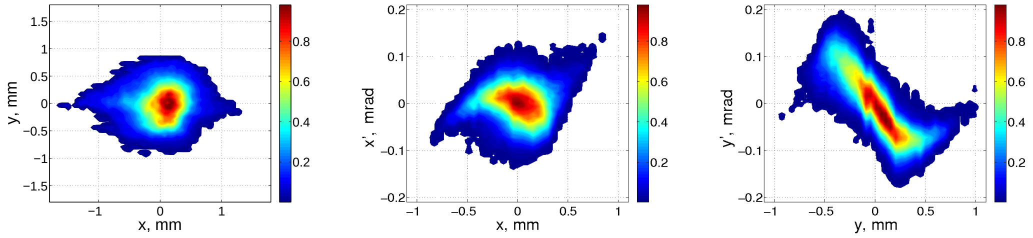

(a) Transverse distribution. $\sigma_{\mathrm{x}} = 0.387\,\mathrm{mm}$, $\sigma_{\mathrm{y}} = 0.316\,\mathrm{mm}$.

(b) X trace space. $\varepsilon_{\mathrm{n,x}} = 0.727\,\mathrm{mm\,mrad}$.

(c) Y trace space. $\varepsilon_{\mathrm{n,y}} = 0.608\,\mathrm{mm\,mrad}$.

Figure 7.19: Transverse electron beam profile and transverse trace spaces at the position of EMSY1 of one of the measurements delivering the minimum emittance value over the whole run period for the electron beam with a charge of 1 nC.

set to MMMG phase for all tested booster accelerating gradients. The rms laser spot size on the cathode of 0.3 mm was chosen as this is the laser beam size delivering the minimum emittance value for the highest available booster accelerating gradient as it was shown in Chapter 7.1.1. The minimum emittance value of 0.867 ± 0.030 mm mrad was found for the maximum achievable booster on-axis peak field of 21 MV/m corresponding to a final electron beam momentum of 24.9 MeV/c. There is a following relation between booster accelerating gradient and booster on-axis peak field: $\mathrm{E_b} = 0.541\,\mathrm{E_b^p}$, where $\mathrm{E_b}$ is a booster accelerating gradient, $\mathrm{E_b^p}$ is a booster on-axis peak field.

As it can be seen from Fig. 7.20 due to the existing limit in the power which can be forwarded to the booster it was not possible to reach the plateau part expected from the simulation results, represented by solid black line, after a certain value of the booster on-axis peak field. Nevertheless looking on the trend of the obtained emittance dependence on the booster accelerating gradient one can guess that the emittance value obtained for the highest available booster accelerating gradient is pretty close to the minimum value which could be obtained with even higher booster accelerating gradients. Moreover, measured emittance dependence on the booster accelerating gradient has a qualitatively good agreement with the simulation data.

7.1.5 Emittance evolution during the run period

The emittance evolution for electron beam of 1 nC charge during the run period was evaluated from the measured data for the machine parameters delivering the minimum emittance. As it was shown in previous sections the minimum emittance values were obtained for the rms laser spot size on the cathode of 0.3 mm, the gun launching phase range of [0; 6] deg and maximum achievable booster accelerating gradients. Only emittance values obtained during statistical measurements at fixed solenoid current defined during a solenoid scan are taken into account. The emittance data sample taken from the available data and satisfying the mentioned conditions is presented in Fig. 7.21. The time break of about one month from April to May in Fig. 7.21 corresponds to dedicated measurements with other charges. As it was already mentioned, the PTO of the laser system was exchanged at the same time together with an improvement of the laser beam line. The general improvements of the emittance values after this changes indicate a strong dependence of the emittance on the quality of the laser beam. Three latest emittance measurements presented in Fig. 7.21 show higher emittance

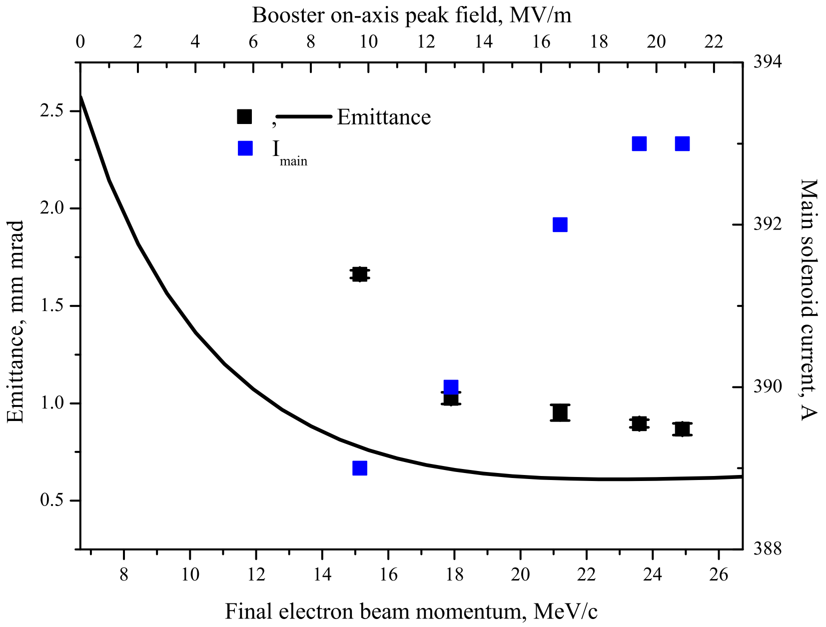

Figure 7.20: Emittance dependence on CDS booster accelerating gradient together with optimum main solenoid currents at the position of EMSY1. Colored squares represent measurement data. Solid black line represents simulations results, see text.

values due to a certain problems with a UV laser PTO and the pulse shaper settings which led to worse homogeneity of the laser transverse shape as well as a shorter laser pulse duration with a stronger modulations on a flat-top part.

7.2 Emittance measurements for 0.25 nC beam charge

As it was mentioned earlier the electron beams with 1 nC charge have the highest interest in the experimental investigations at PITZ. Most of the run time was dedicated to detailed investigations of the phase spaces of such beams as 1 nC charge is the nominal charge of the electron beam used at such facilities like FLASH and the European XFEL. Nevertheless investigations of the transverse phase spaces for other charges have an interest as for example

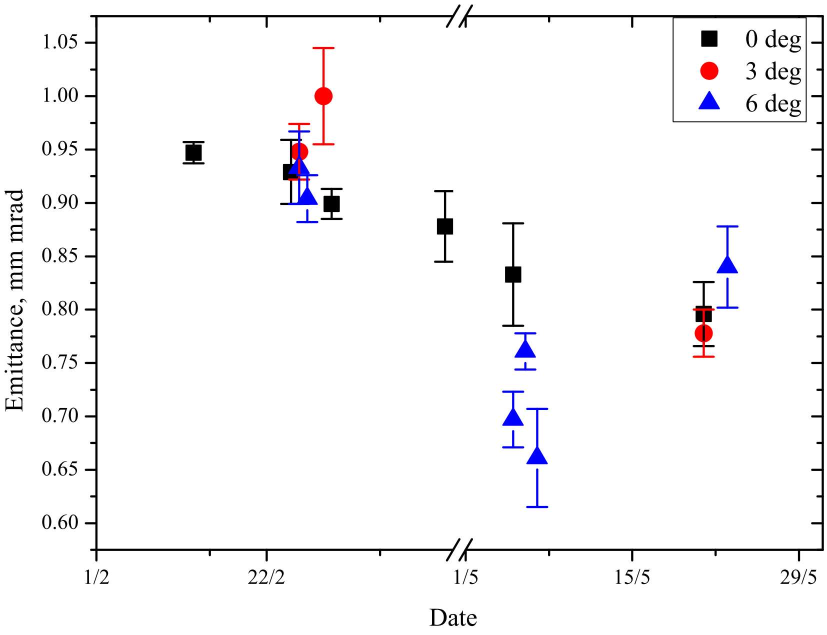

Figure 7.21: Emittance evolution during the run period for the electron beam with a charge of 1 nC at the position of EMSY1 and the rms laser spot size on the cathode of about 0.3 mm.

250 pC electron beam charge is the nominal charge for the operation of the LCLS. In such a way these investigations give the possibility to make a comparison between LCLS and PITZ.

During the investigations of the transverse trace spaces for 250 pC charge only the emittance dependence on the rms laser spot size on the cathode was studied. During these measurements the gun and CDS booster launching phases were fixed to MMMG phases, the CDS booster accelerating gradient was kept around the maximum that gave a final electron beam momentum of about 24.8 MeV/c. The laser pulse length was set to about 21.5 ps FWHM and 2 ps rise/fall times. The solenoid scans together with the statistical measurements at the optimum solenoid current were performed for each measured rms laser spot size at the cathode. The results of these measurements are presented in Fig. 7.22. The meaning of the filled and empty squares is the same as was described at the beginning of Chapter 7.1.1.

A relatively large spread of the emittance values measured for the rms laser spot size on the cathode of 0.125 mm and 0.2 mm is explained by the

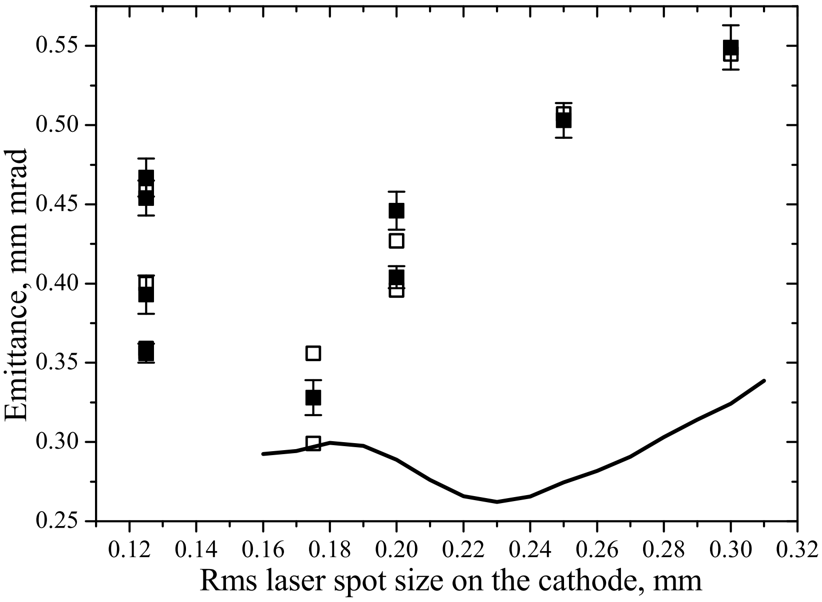

Figure 7.22: Emittance dependence on the rms laser spot size on the cathode for the electron beam with a charge of 250 pC at the position of EMSY1. Black squares represent measurements data. Solid black line represents simulations data, see text.

different electron beam transport. As we can see the proper transport of the electron beam through the beamline, especially through the CDS booster, has a significant influence on the emittance of the electron beam. The simulation of the electron beam with the charge of 1 nC, passing through the CDS booster with an angle of 1 deg with respect to the beamline axis and additionally displaced by 1 mm from the beamline axis, results in emittance value of $\varepsilon_{\mathrm{n}} = 0.85$ mm mrad. For the regular setup simulated emittance value is $\varepsilon_{\mathrm{n}} = 0.61$ mm mrad as shown in Chapter 6.2.

The minimum emittance value was found at the rms laser spot size on the cathode of 0.175 mm. The final electron beam momentum measurement gave a value of 25.07 ± 0.11 MeV/c. Corresponding simulations curve represented by solid black line has fairly weak agreement with the measurements data. There are no simulation data available for the rms laser spot sizes on the cathode of less than 0.16 mm as it is not possible to extract the desired charge with the nominal ASTRA settings. During the solenoid scan presented in Fig. 7.23 the minimum emittance value of 0.299 mm mrad was found at the main solenoid current of 393 A. As well as for the electron beam with 1 nC

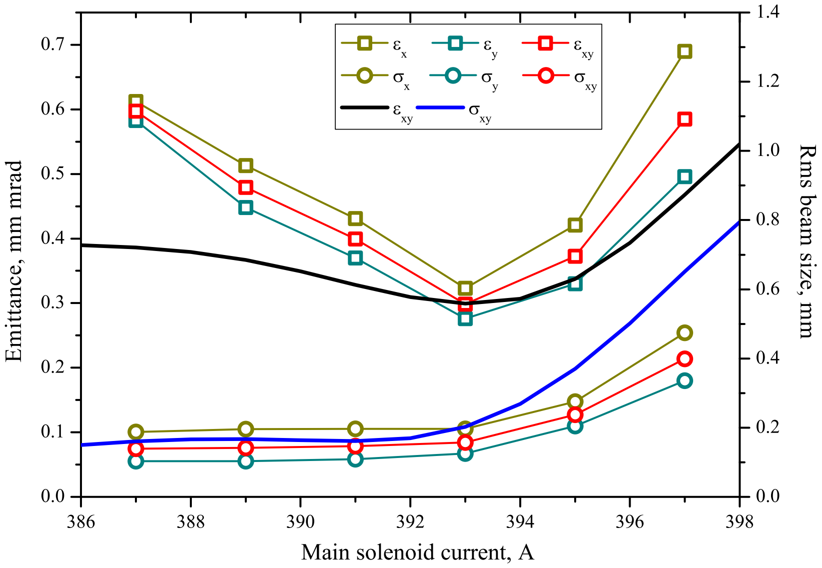

Figure 7.23: Solenoid scan at the position of EMSY1 for the electron beam with a charge of 250 pC and the rms laser spot size on the cathode of 0.175 mm. Connected squares represent measurements data, solid lines represent simulations data. Abscissa axis for the simulation data is artificially shifted by +8 A for comparison, see text.

charge there is a significant discrepancy between the optimum main solenoid current values obtained during the simulations and measurements. Nevertheless as it was already mentioned we cannot relay too much on the measured solenoid field profiles. Systematic linear discrepancy between measured and real solenoid field profiles is well possible. Therefore the abscissa axis for the simulation data is artificially shifted by +8 A in Fig. 7.23, so that emittance minima coincides, for comparison to measured data. After this procedure simulations curves show a quite good agreement with the measurement data.

15 statistical measurements were taken for the main solenoid current of 393 A and are presented in Fig. 7.24. The emittance value estimated out of these measurements is $\varepsilon_{\mathrm{n,xy}} = 0.328 \pm 0.011$ mm mrad. The resulting trace spaces for each transverse plane taken from one of the statistical measurements together with a transverse profile of the electron beam at the position of EMSY1 are presented in Fig. 7.25.

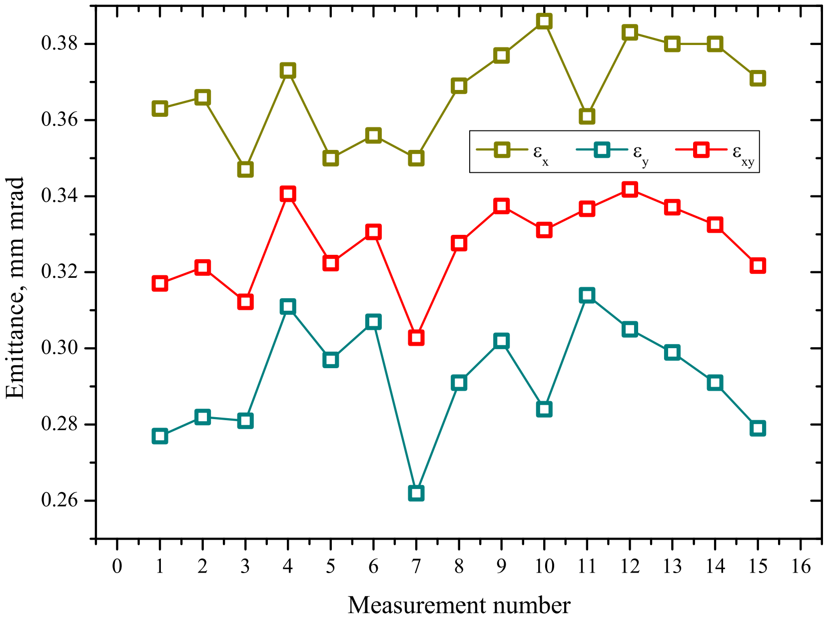

Figure 7.24: 15 statistical emittance measurements at the position of EMSY1 for the electron beam with a charge of 250 pC for the rms laser spot size on the cathode of 0.175 mm and the main solenoid current of 393 A.

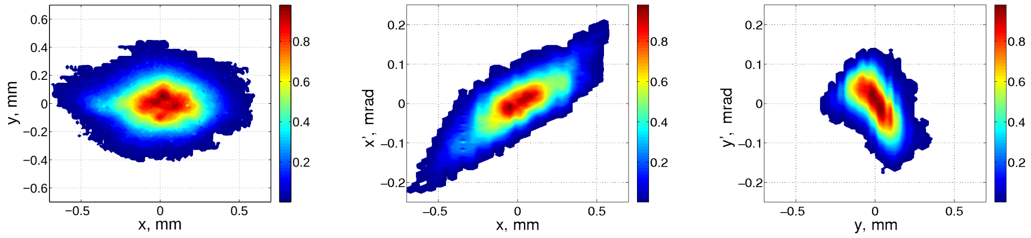

(a) Transverse distribution. $\sigma_x = 0.196$ mm, $\sigma_y = 0.126$ mm.

(b) X trace space. $\varepsilon_{n,x} = 0.369$ mm mrad.

(c) Y trace space. $\varepsilon_{n,y} = 0.291$ mm mrad.

Figure 7.25: Transverse electron beam profile and transverse trace spaces at the position of EMSY1 of one of the measurements delivering the minimum emittance value over the whole run period for the electron beam with a charge of 250 pC.

Comparison of the emittance values obtained at LCLS facility for the electron beam of 250 pC charge as well as for electron beams with other charges is given in Chapter 8.

7.3 Emittance measurements for 0.1 nC beam charge

As well as for the 250 pC case only the emittance dependence on the rms laser spot size on the cathode was studied for the electron beam with a charge of 100 pC. During the measurements the laser pulse length was fixed to about 21.5 ps FWHM and 2 ps rise/fall times, the gun and booster launching phases were set to MMMG phases. Gun and booster were operated at maximum available power that gave electron beam momenta of about 6.7 MeV/c and 25 MeV/c after the gun and CDS booster acceleration, respectively. The measured emittance dependence on the rms laser spot size on the cathode is presented in Fig. 7.26 together with the simulations results represented by black solid line. Still the agreement between the simulations and measurements data is relatively weak. As well as in previous figures of such type empty squares represent minimum emittance value obtained during the solenoid scan, filled squares correspond to statistical measurements at the main solenoid current delivering the minimum emittance.

The minimum emittance value of 0.218 mm mrad was found at the rms laser spot size on the cathode of about 0.125 mm and the main solenoid current of 394 A during the solenoid scan. The details of the solenoid scan during this measurement are presented in Fig. 7.27 together with the results of the corresponding simulations. As well as in case of 250 pC electron beam charge, in order to fit the measurements data, simulation curves were artificially shifted by +8 A. As we can see the simulated transverse electron beam sizes at the position of EMSY1, presented by solid blue line in Fig. 7.27, have a quite good agreement with the measured ones. The emittance curves have a good agreement in a range of solenoid current of [388; 398] A. For lower solenoid currents simulated emittance decreases in contrary to the measured one. Further 9 statistical measurements at the main solenoid current of 394 A gave an emittance value of 0.212 ± 0.006 mm mrad and are presented in Fig. 7.28. Examples of the X and Y trace spaces taken from one of the statistical measurement are shown in Fig. 7.29. As we can see for this measurement the emittance for the Y transverse plane is significantly larger than for X plane. This significant difference comes from larger rms electron beam

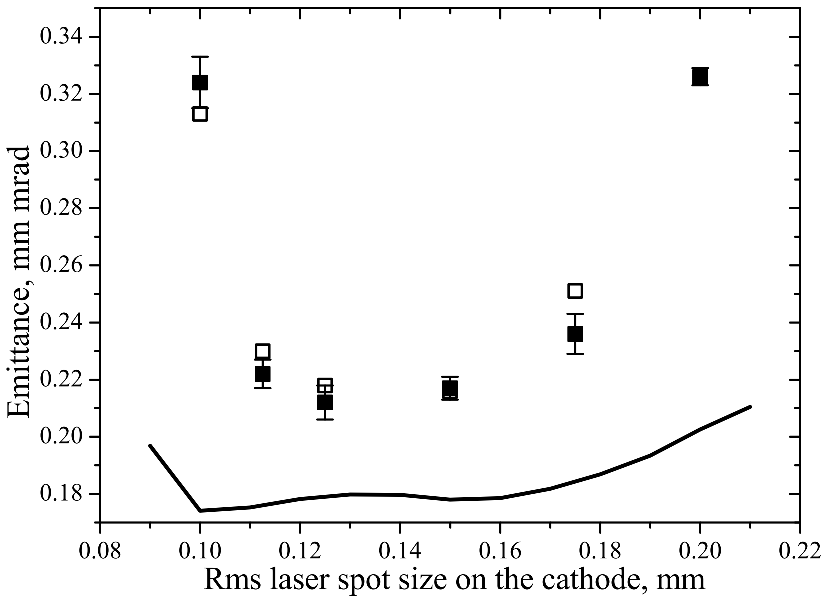

Figure 7.26: Emittance dependence on the rms laser spot size on the cathode for the electron beam with a charge of 100 pC at the position of EMSY1. Black squares represent measurements data. Solid black line represents simulations data, see text.

size and divergence in Y transverse plane. The imperfection in the transverse beam distribution may be caused by different effects such as transport of the electron beam close to the beamline elements, for example laser in-vacuum mirror, that may cause distortion of the beam due to mirror charge effects or bad transport through the CDS booster that may cause a dipole kick in one (or both) transverse planes. Therefore we can guess that with the proper electron beam transport through the beamline even lower emittance value can be achieved for this charge.

7.4 Emittance measurements for 0.02 nC beam charge

The emittance dependence on the rms laser spot size on the cathode was studied for the case of 20 pC electron beam charge and is presented in Fig. 7.30. For some points in this plot the statistical error bars are so small that they

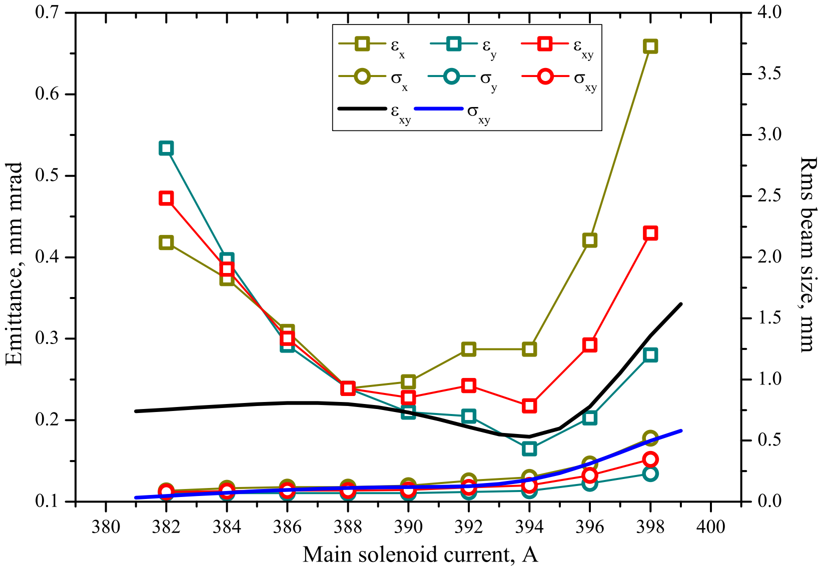

Figure 7.27: Solenoid scan at the position of EMSY1 for the electron beam with a charge of 100 pC and the rms laser spot size on the cathode of 0.125 mm. Connected squares represent measurements data, solid lines represent simulations data. Abscissa axis for the simulation data is artificially shifted by +8 A for comparison, see text.

are lying within the marker size. As well as in the previous case, the laser length was fixed to about 21.5 ps FWHM and 2 ps rise/fall times. The gun and booster launching phases were fixed to the MMMG phases. Due to a lower intensity than in the cases of higher electron beam charges it was necessary to use more laser pulses during these measurements in order to achieve a reasonable signal to noise ratio on the observation screen. This caused the necessity to increase the RF pulse length of the gun and the booster. Unfortunately the booster was not capable to operate at longer RF pulse length at full power (conditioning was not finished yet for longer RF pulse duration). This led to a slight decrease of the power in the booster that gave slightly reduced final electron beam momentum of 23.5 MeV/c in comparison to about 25 MeV/c for the emittance measurements with the other electron beam charges. We have to notice that taking into account the possible error of the emittance estimation due to the deviation of the different machine parameters from their optimum values (see Chapter 5.3) it is not possible to determine the optimum rms laser spot size on the cathode unambiguously

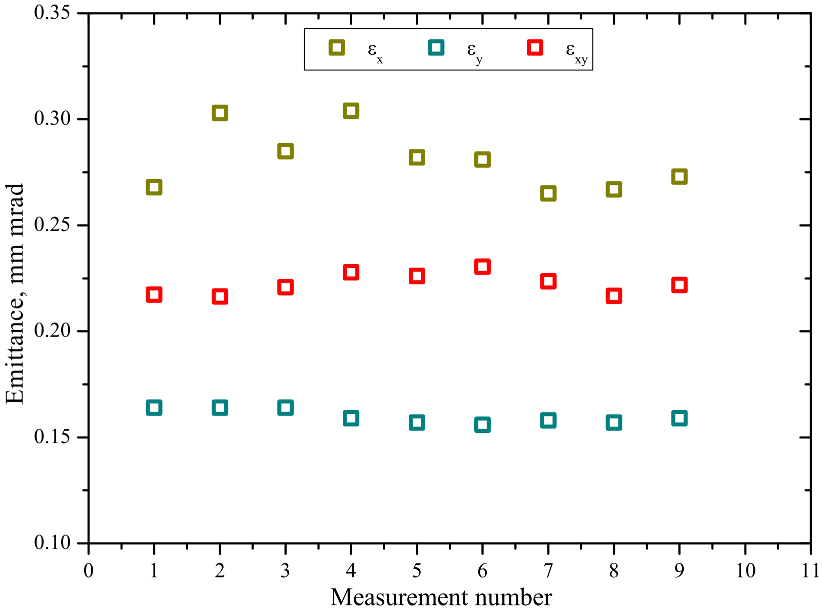

Figure 7.28: 9 statistical emittance measurements at the position of EMSY1 for the electron beam with a charge of 100 pC for the rms laser spot size on the cathode of 0.125 mm and the main solenoid current of 394 A.

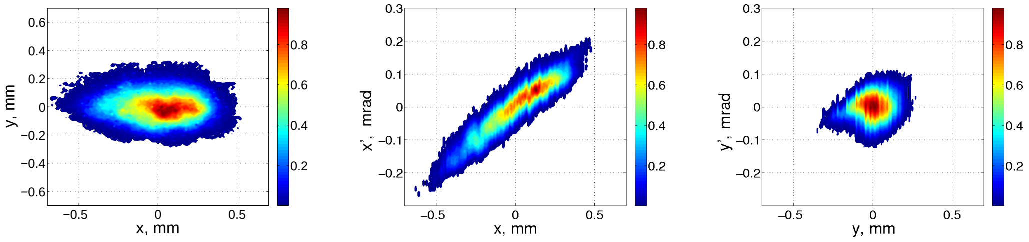

(a) Transverse distribution. $\sigma_{\mathrm{x}} = 0.197\,\mathrm{mm}$, $\sigma_{\mathrm{y}} = 0.09\,\mathrm{mm}$.

(b) X trace space. $\varepsilon_{\mathrm{n,x}} = 0.282\,\mathrm{mm\,mrad}$.

(c) Y trace space. $\varepsilon_{\mathrm{n,y}} = 0.157\,\mathrm{mm\,mrad}$.

Figure 7.29: Transverse electron beam profile and transverse trace spaces at the position of EMSY1 of one of the measurements delivering the minimum emittance value over the whole run period for the electron beam with a charge of 100 pC.

from the data presented in Fig. 7.30. Taking into account possible systematic errors described in Chapter 5 which are significant for the electron beams with 20 pC charge, there is a relatively good agreement between measured and simulated curves presented in Fig. 7.30 by solid black line. The meaning of the filled and empty squares is the same as was described at the beginning of Chapter 7.1.1.

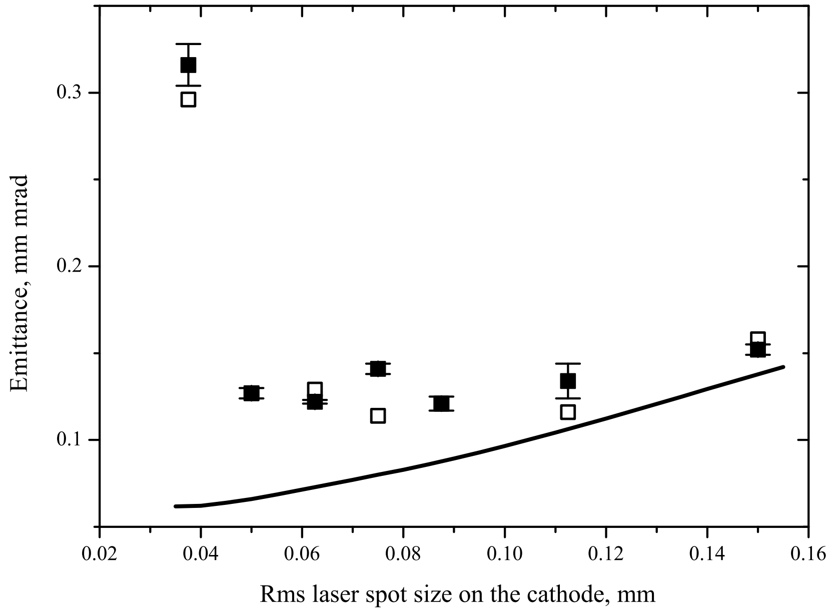

Figure 7.30: Emittance dependence on the rms laser spot size on the cathode for the electron beam with a charge of 20 pC at the position of EMSY1. Black squares represent measurements data. Solid black line represents simulations data, see text.

The minimum emittance value of 0.121 mm mrad was found at the rms laser spot size on the cathode of 0.088 mm and at the main solenoid current of 388 A during the solenoid scan. The details of the solenoid scan are presented in Fig. 7.31. Corresponding simulated emittance and rms electron beam size at the position of EMSY1 presented by black and blue solid lines, respectively, have a relatively good agreement with the measured ones. 10 statistical measurements performed for the main solenoid current of 388 A gave the emittance value of 0.121 ± 0.004 mm mrad and are presented in Fig. 7.32. An example of the trace spaces taken from one of the statistical measurement

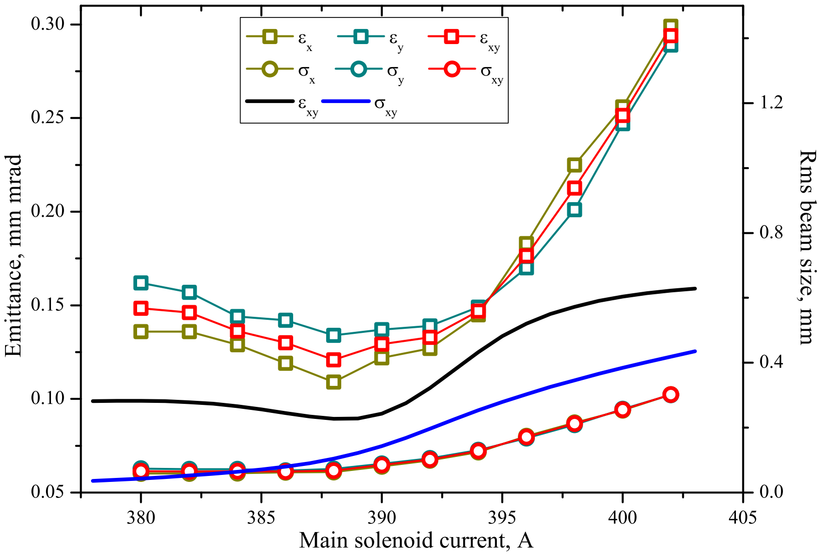

Figure 7.31: Solenoid scan at the position of EMSY1 for the electron beam with a charge of 20 pC and the rms laser spot size on the cathode of 0.088 mm. Connected squares represent measurements data, solid lines represent simulations data. Abscissa axis for the simulation data is artificially shifted by +8 A for comparison, see text.

together with the transverse distribution of the electron beam at the position of EMSY1 is presented in Fig. 7.33.

7.5 Emittance measurements for 2 nC beam charge

Emittance measurements with a 2 nC electron beam charge were performed for a fixed laser pulse length of 21.5 ps FWHM and 2 ps rise/fall times. The CDS booster launching phase was fixed to the MMMG phase during all the measurements. Emittance dependence on the rms laser spot size on the cathode was measured. The gun launching phase was fixed to the MMMG phase for all measurements except the measurement with an rms laser spot size on the cathode of 0.375 mm during which it was set to +6 deg with respect to MMMG phase as it was not possible to extract the desired charge at the MMMG phase for this laser spot size. The results of the measurements

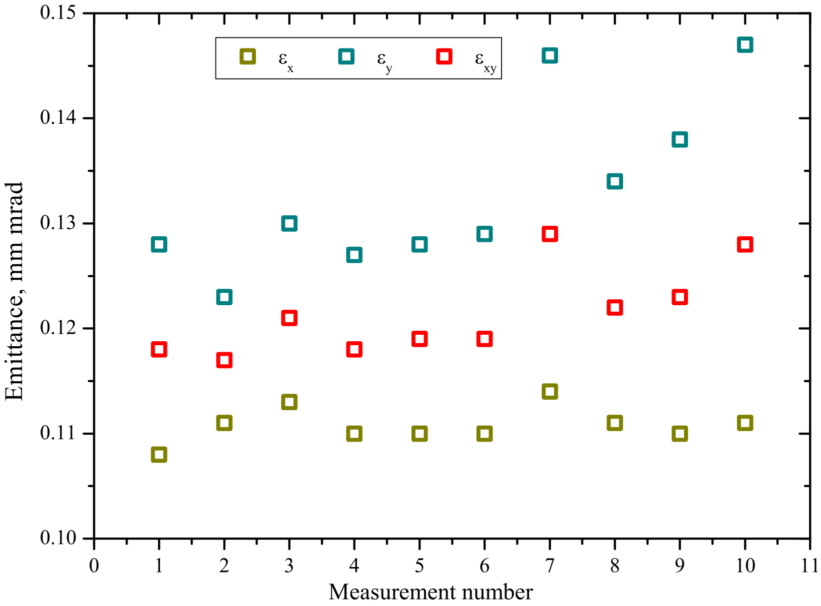

Figure 7.32: 10 statistical emittance measurements at the position of EMSY1 for the electron beam with a charge of 20 pC for the rms laser spot size on the cathode of 0.088 mm and the main solenoid current of 388 A.

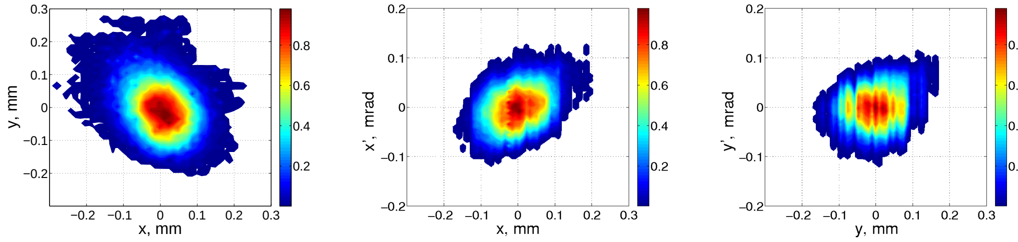

(a) Transverse distribution. $\sigma_x = 0.064$ mm, $\sigma_y = 0.075$ mm.

(b) X trace space. $\varepsilon_{n,x} = 0.11$ mm mrad.

(c) Y trace space. $\varepsilon_{n,y} = 0.13$ mm mrad.

Figure 7.33: Transverse electron beam profile and transverse trace spaces at the position of EMSY1 of one of the measurements delivering the minimum emittance value over the whole run period for the electron beam with a charge of 20 pC.

are presented in Fig. 7.34 together with the corresponding simulation curve. Simulation curve, represented by solid black line in Fig. 7.34, was obtained for the MMMG gun launching phase. As we can see there is significant discrepancy between the rms laser spot size on the cathode delivering minimum emittance values in measurements and simulations. The simulation curve is limited at the rms laser spot size on the cathode of 0.55 mm as for lower sizes it is not possible to extract the desired charge.

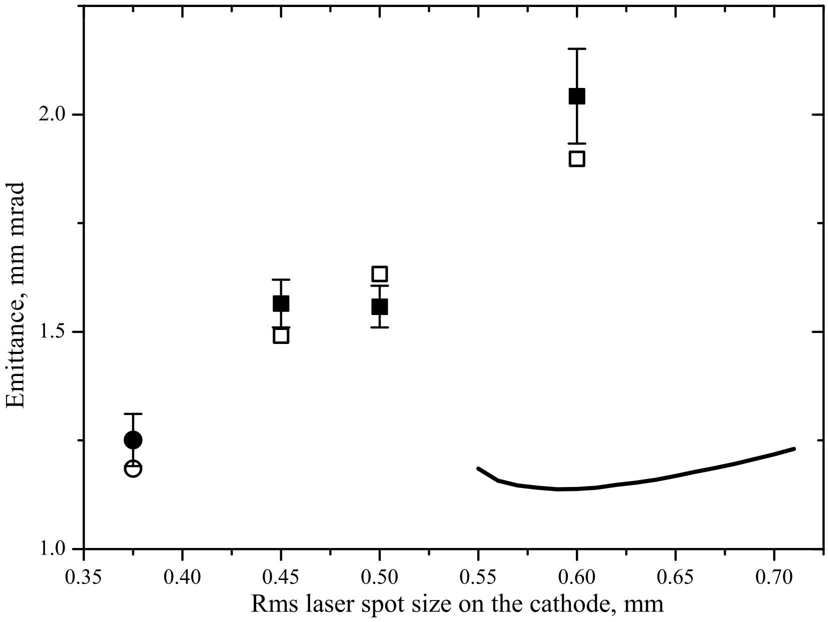

Figure 7.34: Emittance dependence on the rms laser spot size on the cathode for the electron beam with a charge of 2 nC at the position of EMSY1. Black squares represent measurements data for gun launching phase set to MMMG phase. Black circles represent measurement with the gun launching phase set to MMMG + 6 deg phase. Solid black line represents simulations data, see text.

The minimum emittance value of 1.185 mm mrad was found at the rms laser spot size on the cathode of 0.375 mm during the solenoid scan at the main solenoid current of 395 A and presented in Fig. 7.35 together with corresponding simulations data represented by solid lines. As it was not possible to extract desired charge for the rms laser spot size on the cathode of 0.375 mm during the simulations, rms laser spot size of 0.59 mm is used for comparison as the value delivering the minimum emittance among the simulation data. As we can see there is a quite good agreement of the minimum measured and predicted by simulations emittance values represented by black solid line in Fig. 7.35. Nevertheless, emittance growth predicted by simulations is lower than experimentally measured. Moreover, the rms electron beam sizes at the position of EMSY1, obtained from simulations and represented by solid blue line in Fig. 7.35, is significantly higher than the measured ones. 9 statistical measurements taken for the rms laser spot size on the cathode of 0.375 mm at the main solenoid current of 395 A yield the emittance value of 1.25 ± 0.06 mm mrad and are presented in Fig. 7.36. An example of the trace spaces taken from one of the statistical measurement for the rms laser spot size on the cathode of 0.375 mm together with the transverse distribution of the electron beam at the position of EMSY1 is presented in Fig. 7.37.

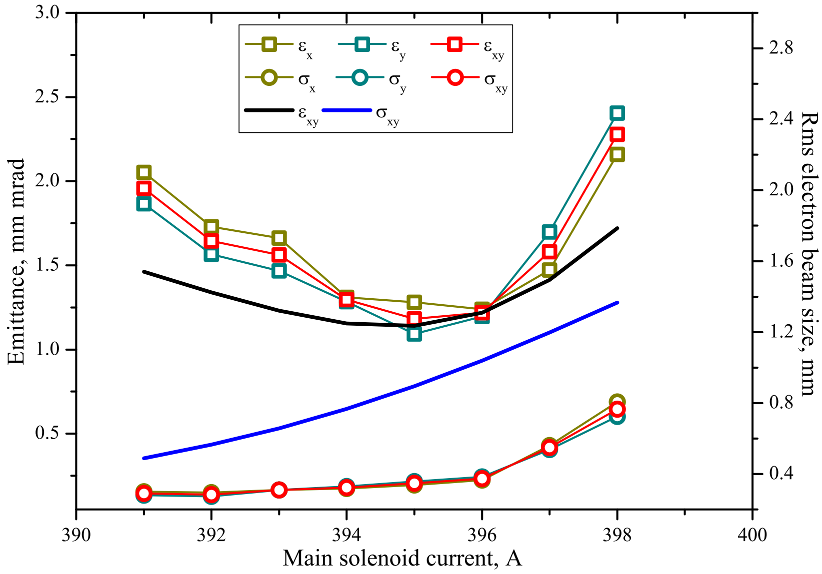

Figure 7.35: Solenoid scan at the position of EMSY1 for the electron beam with a charge of 2 nC and the rms laser spot size on the cathode of 0.375 mm. Connected squares represent measurements data, solid lines represent simulations data. Abscissa axis for the simulation data is artificially shifted by +8 A for comparison, see text.

Among the measurements which were done for the MMMG gun launching phase the minimum emittance value of 1.633 mm mrad was found at the rms laser spot size on the cathode of 0.5 mm and at the main solenoid current of 394 A during the solenoid scan. At this value of the main solenoid current

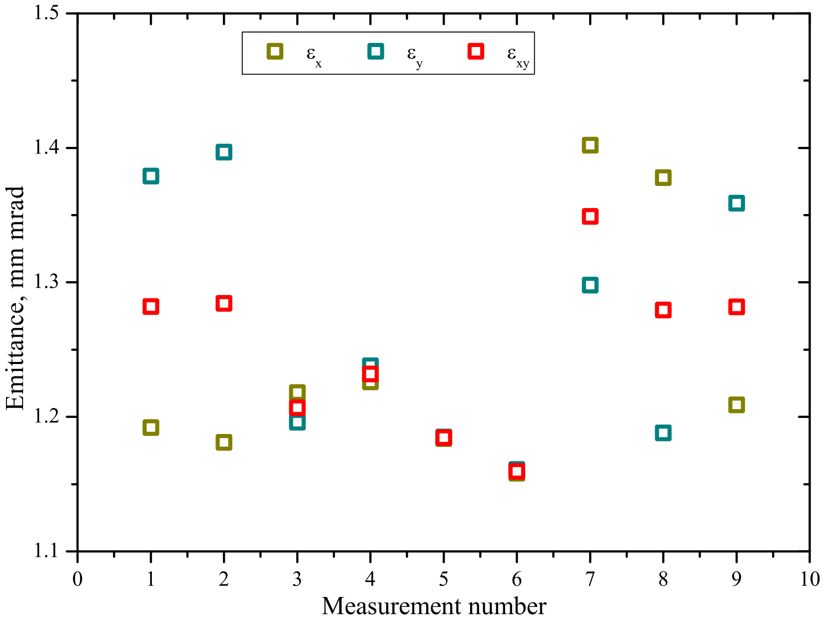

Figure 7.36: 9 statistical emittance measurements at the position of EMSY1 for the electron beam with a charge of 2 nC for the rms laser spot size on the cathode of 0.375 mm and the main solenoid current of 395 A.

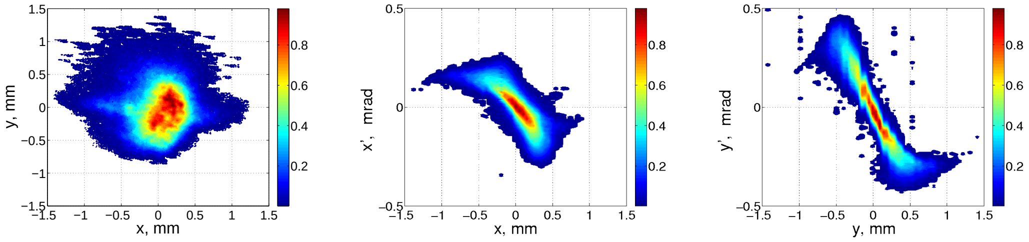

(a) Transverse distribution. $\sigma_x = 0.323$ mm, $\sigma_y = 0.345$ mm.

(b) X trace space. $\varepsilon_{n,x} = 1.18$ mm mrad.

(c) Y trace space. $\varepsilon_{n,y} = 1.34$ mm mrad.

Figure 7.37: Transverse electron beam profile and transverse trace spaces at the position of EMSY1 of one of the measurements delivering the minimum emittance value over the whole run period for the electron beam with a charge of 2 nC.

the emittance value of 1.56 ± 0.05 mm mrad was obtained from 9 statistical measurements.

7.6 Summary

Emittance data obtained for electron beams with different charges are summarized and presented in Fig. 7.38 together with emittance measurement results for a TESLA type booster [43]. As one can see the systematic reduction of the emittance values for different electron beam charges was achieved with the upgraded PITZ setup including the exchange of the booster type from TESLA to CDS, improvement of the low level RF system of the gun and exchange of the pulse train oscillator of the UV laser system together with upgrade of the laser beam line. Only statistical errors are included to the data presented in Fig. 7.38. Selecting the minimum emittance values obtained with the CDS booster for different charges from these data and adding the systematic errors caused by the finite size of the camera pixels and its discrete signal structure as well as the systematic error caused by the deviation of the machine parameters from their optimum values as described in Chapter 5, one gets quite good agreement of the experimentally measured emittance values to the simulations presented in Fig. 7.39. As all experimental measurements were done for a booster on-axis peak field of about 20 MV/m, the simulation data presented in Fig. 7.39 represent not the absolute minimum emittance values for the electron beam charges of 20, 100 and 250 pC which were found at the booster on-axis peak fields of $\mathrm{E}_\mathrm{b}^\mathrm{p} \leq 7\,\mathrm{MV/m}$, but the results of the simulations with the fixed booster on-axis peak field of $\mathrm{E}_\mathrm{b}^\mathrm{p} = 20\,\mathrm{MV/m}$ presented in Chapters 6.5.2, 6.4.2 and 6.3.2.

Despite the quite good agreement of experimentally measured and simulated emittance one has to notice that the machine parameters at which the minimum emittance values were found differ quite strongly. All the machine parameters at which minimum emittance values were obtained during the measurements and simulations for different electron beam charges are summarized in Table 7.1 together with emittance numbers for comparison. For the experimentally measured emittance values statistical and systematical errors are shown at the last column of Table 7.1 as a first and second terms, respectively. Statistical errors are calculated as described in Chapter 7.1.1. Systematical errors are calculated as described in Chapter 5. As we can see for all electron beam charges there is a significant difference between optimum measured and simulated main solenoid currents of about $\Delta\mathrm{I}_\mathrm{main} = [8; 10]\,\mathrm{A}$.

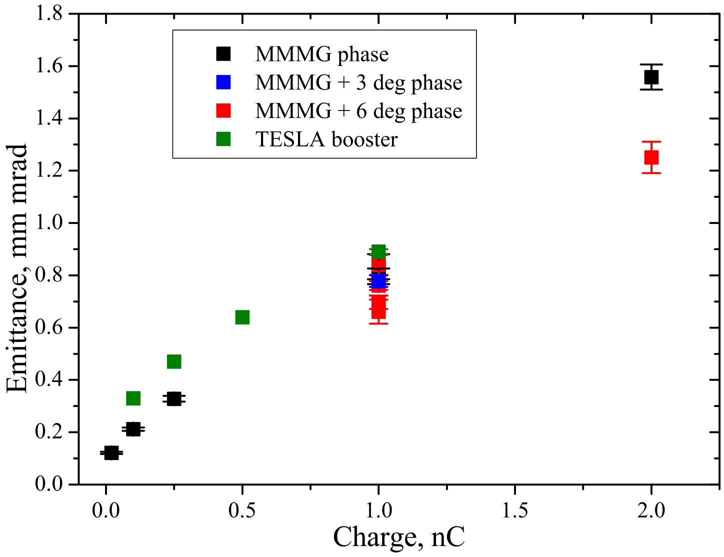

Figure 7.38: Emittance dependence on electron beam charge at the position of EMSY1 for different type of booster cavities. Error bars represent statistical errors.

	Simulations				
Q, nC	σ_L, mm	I_{main}, A	Φ_{gun}, deg	$\varepsilon_{n,xy}$, mm mrad	$\Delta\varepsilon_{n,xy}$, mm mrad
2	0.59	387	-1	1.138	
1	0.4	386	0	0.61	
0.25	0.23	385	1.5	0.262	
0.1	0.1	385	2	0.174	
0.02	0.035	380	1.5	0.061	
	Measurements				
2	0.375	395	6	1.251	±0.060 – 0.093
1	0.3	396	6	0.661	±0.046 – 0.09
0.25	0.175	393	0	0.328	±0.011 – 0.037
0.1	0.113	394	0	0.212	±0.006 – 0.019
0.02	0.088	388	0	0.121	±0.004 – 0.083

Table 7.1: Simulated and measured emittance values and corresponding main machine parameters for different electron beam charges. At the last column the first term represents statistical error, second - systematical error, see text.

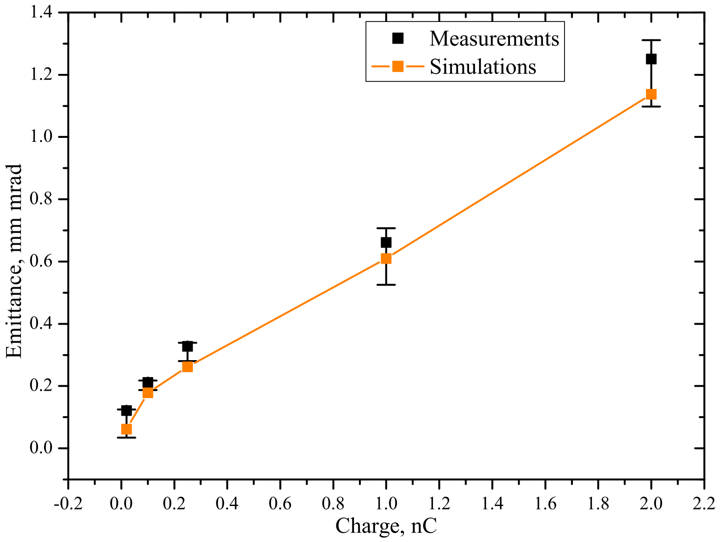

Figure 7.39: Minimum emittance values obtained with the CDS booster at the position of EMSY1, selected from data presented in Fig. 7.38, as a function of the electron beam charge. Error bars represent statistical and systematic errors.

It can be partially explained by the measurement precision of the solenoid field. For the electron beam with a charge of 2 and 1 nC one can see the significant difference of $\Delta\Phi_{\mathrm{gun}} = 6$ deg between simulated and measured gun launching phases. One has to take into account that for electron beams with a charge of 250 pC and lower all the emittance measurements were done only at MMMG gun launching phase. For all tested charges we can see the systematic decrease of the experimentally obtained optimum rms laser spot size on the cathode by more than 30 % as compared to simulations. Moreover, due to mirror charge effects at the cathode, with the settings used during the simulations it is not possible to extract 2 nC for the rms laser spot size on the cathode of $\sigma_{\mathrm{L}} = 0.375$ mm, as well as 1 nC for the rms laser spot size on the cathode of $\sigma_{\mathrm{L}} = 0.3$ mm. The aforementioned effect as well as the difference between experimental and simulation values in other parameters may be explained by the Schottky-like effect which describes the lowering of the work function or electron affinity in the material at the presence of an electric field. This leads to an increased electron emission from the cathode surface [44]. The increase of the emitted charge in the ASTRA code is taken into account by the following formula $Q_{emit} = Q_0 + S_1\sqrt{E_c} + S_2E_c$ as described in [36]. Here Q_0 is the charge of the initial distribution, E_c is the sum of the longitudinal space-charge and RF fields at the cathode center, S_1 and S_2 are constants describing the field dependent emission process.

In order to investigate the influence of the Schottky-like effect on the emission process several experiments were performed at PITZ as described in [45]. As it was shown, it is not possible to extract 1 nC for the rms laser spot size on the cathode of $\sigma_L = 0.3$ mm at any combination of Q_0, S_1 and S_2. In order to extract the desired charge it is necessary to increase σ_L by 0.02 mm which is a first sign of disagreement of the proposed model to the experimental results. The minimum emittance value of $\varepsilon_{n,xy} = 1.1$ mm mrad was found at the MMMG gun launching phase, booster on axis peak field of $E_b^p = 19$ MV/m and main solenoid current of $I_{main} = 382$ A. As we can see the discrepancy between experimentally measured and simulated optimum main solenoid currents is even stronger in this case. Moreover the obtained trace space presented in Fig. 7.40 has "wings" which were not observed during experimental measurements. In such a way we have to conclude that the model of the enhanced field emission used by ASTRA does not describe the real emission process well, the understanding of the emission process is quite important and needs further investigations.

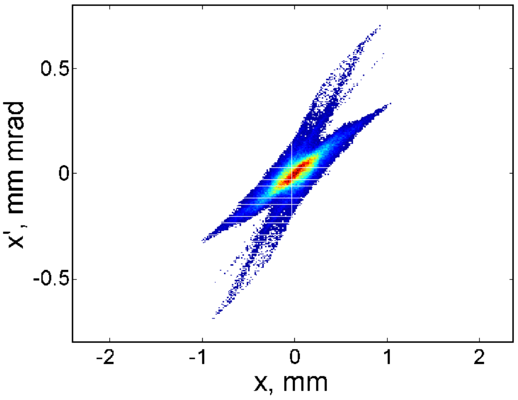

Figure 7.40: Transverse trace space at the position of EMSY1 obtained from simulations taking into account enhanced charge emission in the presence of an electric field, see text.

During the FEL lasing process particles distributed in the outermost phase space region might stay out of the amplifier bandwidth and hence only the core of the distribution takes part in the FEL lasing process. Therefore the emittance of the phase space core which contains only of a certain fraction of the particles and assumes to correspond to the lasing part of the beam is of practical interest. This so-called core emittance usually calculated from the fraction of the phase space distribution inside the equidensity contour which corresponds to a certain fraction of the whole charge [8]. Calculated from the simulation and measurement data core emittance for the electron beam with a charge of 1 nC is presented in Fig. 7.41. As we can see, by removing of 10 % from the outermost part of the measured trace space, significant emittance reduction from $\varepsilon_{\mathrm{n}} = 0.665$ mm mrad to $\varepsilon_{\mathrm{n}}^{90\%} = 0.51$ mm mrad is achieved. For the simulation case emittance reduces faster, also cutting 10 % of the charge reduces emittance from $\varepsilon_{\mathrm{n}} = 0.61$ mm mrad to $\varepsilon_{\mathrm{n}} = 0.35$ mm mrad. In such a way assuming that 10 % of the charge located in the outermost trace space region does not take place in the lasing process, further improvement of the

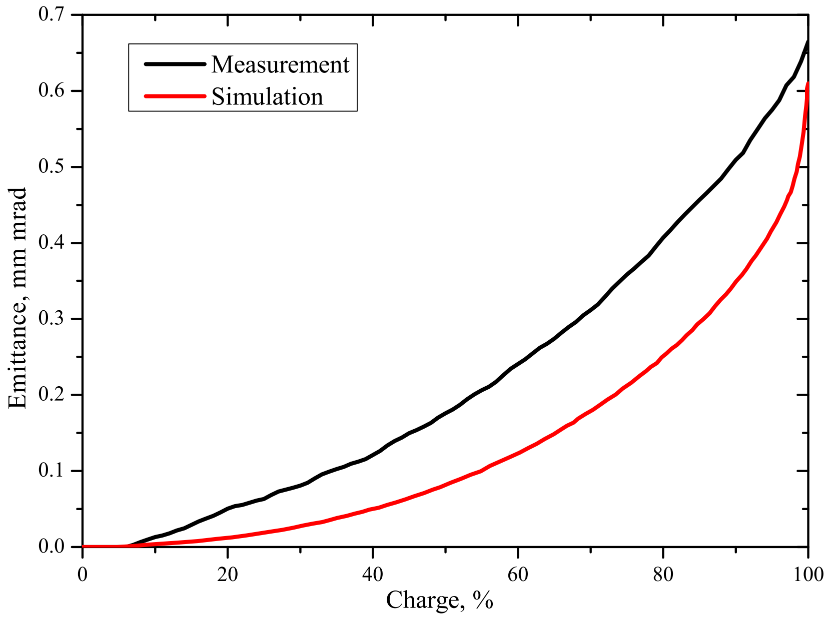

Figure 7.41: Simulated and measured core emittance for the electron beam of 1 nC charge. Trace spaces from which presented data were obtained are presented in Fig. 6.1 and Fig. 7.19 for the simulation and measurement, respectively.

FEL parameters is expected.

Core emittances for electron beams with other charges are presented in Fig. B.1. As we can see all of them behave similarly to the case of electron beam with 1 nC charge. With a reduction of amount of charge as described above, the emittance reduces slower in measurements as compared to simulations for all electron beam charges. For the electron beam of 20 pC charge large systematic overestimation of the emittance during the measurements has to be taken into account as described in Chapter 5.2.

Comparison of the obtained at PITZ emittance values for electron beams with different charges to emittance obtained at such FEL facilities like LCLS, SACLA and SPARC is presented in the following Chapter 8.

Chapter 8

Summary and outlook

Emittance studies for several electron beam charges were performed with the gun cavity to be used at such free electron lasers like FLASH and the European X-FEL. Detailed dependencies of the emittance on the different machine parameters were simulated with the help of the particle tracking code ASTRA. The single slit scan technique was used to perform the experimental emittance measurements. A significant part of the thesis is dedicated to emittance studies in simulations for a wide range of the machine parameters. Only a fraction of the presented results obtained during the simulations was covered with experimental measurements due to a lack of operational time. Both, the simulations and measurement, are concentrated mainly on the electron beam emittance studies with a charge of 1 nC which is the nominal charge for the operation of FLASH and the European X-FEL.

The minimum emittance value of about 0.61 mm mrad was obtained for the electron beam with a charge of 1 nC during the simulations. This value was obtained for the fixed gun on-axis peak field of 60.5 MV/m and fixed laser length of 21.5 ps FWHM and 2 ps rise/fall times. Other machine parameters like rms laser spot size on the cathode, gun launching phase, main solenoid current and CDS booster on-axis peak field were tuned in order to minimize the emittance at the position of EMSY1 located 5.74 m downstream the cathode. The emittance dependence on gun on-axis peak field studied in simulations yields the emittance value of about 1.05 mm mrad for gun on-axis peak field of $\mathrm{E_g^p} = 45\,\mathrm{MV/m}$, which corresponds to the maximum currently available field at FLASH facility, using the PITZ-like UV laser system with the laser pulse length of 21.5 ps at FWHM and 2 ps rise/fall times. In such a way with a possible upgrade of the UV laser system of FLASH from the current one which produces longitudinally Gaussian pulses with a FWHM of about 15.3 ps to a PITZ-like UV laser system the emittance reduction by about 25 % is awaited. By additional upgrade of the FLASH gun RF system to a PITZ type, maximum on-axis peak field in the gun can be increased up to $\mathrm{E}_{\mathrm{g}}^{\mathrm{p}} = 60.5\,\mathrm{MV/m}$ that will lead to further reduction of the emittance by about 40 %. In total with aforementioned upgrades of the FLASH facility the emittance reduction by a factor of 2.33 is expected.

The methodical studies of the emittance dependencies on different machine parameters in simulations open a possibility to predict the behavior of other machine parameters while changing a certain parameter. As it was shown by the deviation of a certain parameter from its optimum value the other parameters change their optimum values not significantly and the emittance growth is moderate. The systematic error caused by the deviation of the machine parameters from their optimum values, taking into account the experimental uncertainties in their determination, does not exceed 13% for the whole range of the studied electron beam charges (2 nC, 1 nC, 0.25 nC, 0.1 nC and 0.02 nC). The other sources of the systematic errors like a finite width of the slit opening, space-charge forces and finite size of the camera pixel are studied and their total contribution does not exceed 10% for all the charges except from 20 pC. For the electron beam with a charge of 20 pC the systematic overestimation by more than a factor of two is expected due to a limited resolution of the optical readout system and properties of the camera used for the image taking. As for the electron beam with this charge the divergence and the transverse size of the beam at the position of EMSY1 are quite small, the modification of the original distribution according to the camera nature cause a severe calculation errors. A redesign of the current optical readout system is necessary in order to minimize the systematic errors caused by the finite size of the camera pixel and its discrete signal nature on the emittance estimation for the electron beams with a charge of 20 pC or lower.

Upgrades of the low level RF gun system, photocathode UV laser system and exchange of the old type TESLA cavity to the CDS cavity brought a significant reduction of the experimentally measured emittance from about $1.27^{+0.02}_{-0.07} \pm 0.15$ mm mrad [8] to less than 0.9 mm mrad for the electron beam with 1 nC charge. We have to take into account that these upgrades, except photocathode laser system, were performed almost at the same time and therefore it is not possible to unambiguously define if the CDS booster provides better emittance values than TESLA one. According to results of the simulations presented in Chapter 6.7, minimum achievable emittance values for the electron beams with different charges are comparable for both types of the booster and therefore are awaited on the future European XFEL facility as well (some more discussion about transition of the data obtained at PITZ setup to FLASH and the European XFEL can be found in Chapter 6.7).

Emittance values of less than 0.9 mm mrad for electron beams with 1 nC charge were measured regularly after the improvement of the stability of the UV photocathode laser system that indicates good stability of the other machine parameters like cavities phases, main solenoid current and cavity fields amplitudes. The absolute minimum emittance value of $0.661 \pm 0.046 - 0.09$ mm mrad was measured for the electron beam with a charge of 1 nC during the whole run period and has a good agreement with predicted by simulations emittance value of 0.61 mm mrad. Emittance values measured for electron beams with other charges are presented in Table 7.1 and in Fig. 7.39 and have a good agreement to the emittance values predicted by simulations as well.

Despite the good agreement between the measured and simulated emittance values for electron beams with different charges, machine parameters, at which they were found, are significantly different during the simulations as compared to measurements. The main solenoid current at which minimum emittance values were found for the electron beams with all charges except from 1 nC is by 8 A higher in the simulations as compared to measurements. For the electron beam of 1 nC charge this difference is 10 A. This discrepancy may be partially caused by precision of the solenoid magnetic field measurement results of which were used as an input for the simulations. Discrepancies between simulated and measured optimum rms laser spot sizes and gun launching phases for electron beams with different charges are caused by the enhanced charge emission in the presence of the electric field as discussed in Chapter 7.6. With a model included to ASTRA code, which was used for simulations, it is not possible to extract 1 nC, for any combination of the model parameters, for the rms laser spot size of 0.3 mm which was determined as the optimum rms laser spot size from the measurements data. The smallest rms laser spot size of 0.32 mm at which it is possible to extract 1 nC taking into account enhanced charge emission in the presence of the electric field during ASTRA simulations yields to the emittance value of $\varepsilon_{\mathrm{n,xy}} = 1.1$ mm mrad still at the MMMG phase. Moreover the obtained transverse trace space has a "wings" not observed during the experimental measurements. Therefore the aforementioned model describes the real photoelectron emission process not well enough and further investigations of the photoemission process are necessary.

As the electron beam length after injector at FEL facilities will be modified by further acceleration and beam compression systems, brightness $\mathrm{B_n}$ defined by Eq. 1.5 is not appropriate to compare the quality of the beams at this point. In order to compare the quality of the electron beams after injector Eq. 1.5 modified as follows can be used:

$$qB_n = \frac{2Q}{\varepsilon_n^2} \tag{8.1}$$

where Q is the charge of the electron beam and $\mathrm{qB_n}$ is the so-called charge brightness. Comparison between emittance values and charge brightness of the electron beams with various charges after injector obtained at PITZ and other facilities, e.g. LCLS [46, 47], SACLA [3, 48] and SPARC [49] is presented in Fig. 8.1. As we can see from Fig. 8.1 emittance values measured at PITZ are significantly lower than emittance measured at other facilities for electron beams with a charge of > 250 pC. For the electron beam charges ≤ 250 pC emittance measured at PITZ is comparable to LCLS facility and still significantly lower than measured at SACLA. Charge brightness of the electron beams with different charges also shows better values as compared to other facilities. Additionally, we have to notice that such facilities like LCLS and SACLA can accelerate a single electron bunch with the repetition rate of 120 and 10 Hz (see Chapter 1), respectively. As it was mentioned,

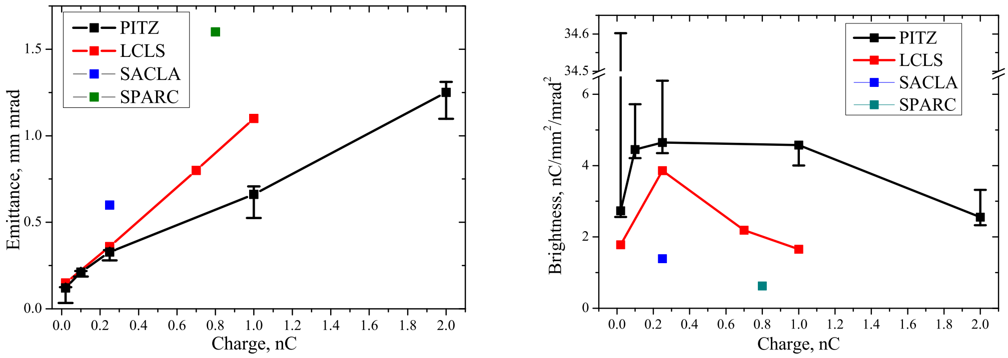

(a) Electron beam emittance.

(b) Electron beam brightness.

Figure 8.1: Electron beam emittance and brightness at the injector exit measured at different FEL facilities, see text.

up to 650 electron bunches can be produced with repetition rate of 10 Hz at PITZ. And the European XFEL will produce even more, by factor of about 4.5, bunches (see Chapter 2.1). In such a way the average brightness of the electron beam at the European XFEL is expected to be up to several orders higher than the brightness of aforementioned facilities.

Outlook

Additionally to the transverse projected emittance measurements of the electron beam, the recently installed transverse deflecting cavity will open the possibility of the time resolved emittance measurements with high resolution (down to 0.3ps) in the nearest future.

Emittance measurements along the PITZ beamline were not possible due to different reasons. Such measurements are necessary in order to compare them to the simulation data presented in this work. Such comparison will help to better understand the electron beam dynamics along the beamline.

The difference of the optimum machine parameters at which minimum emittance values were found during the simulations and experiments needs further investigation. Photoelectron emission model used in ASTRA simulation code, which was used in the frame of this work, has to be reviewed. Simulations with newest versions of other particle tracking codes, e.g. PARMELA [50], GPT [51] etc., are required as well.

Emittance measurements of the electron beam after the beam compression system which will be installed at PITZ in the nearest future are required as well as the corresponding simulations.

As it was shown in the frame of these work, upgrade of the photocathode UV laser and gun RF system at FLASH may reduce the emittance by a factor of more than 2 for the 1 nC electron beam charge operation.

Emittance measurements results presented in the frame of this work and the experiences with the beam transport at the LCLS facility prompted a revision of the electron beam parameters and charge scope as presented in recent European XFEL Post-TDR description [52].

Appendices

Appendix A

Additional figures for simulations

A number of figures related to the results of the emittance studies presented in Chapter 6 using the ASTRA code are collected here.

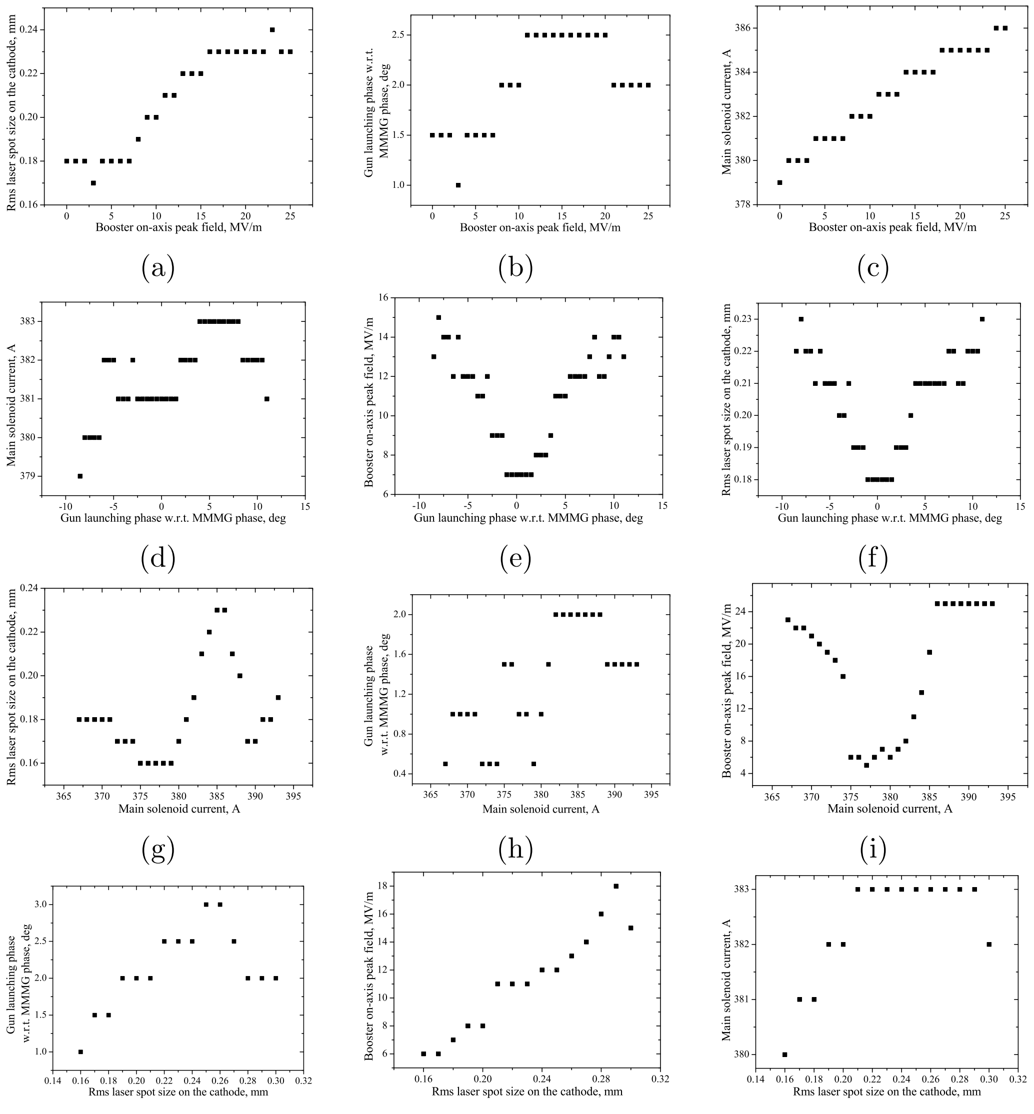

(a) (b) (c)

(d) (e) (f)

(g) (h) (i)

(j) (k) (l)

Figure A.1: Dependencies of different parameters on a certain machine parameter delivering the minimum emittance value. Each triplet of plots corresponds to a certain plot from Fig. 6.9.

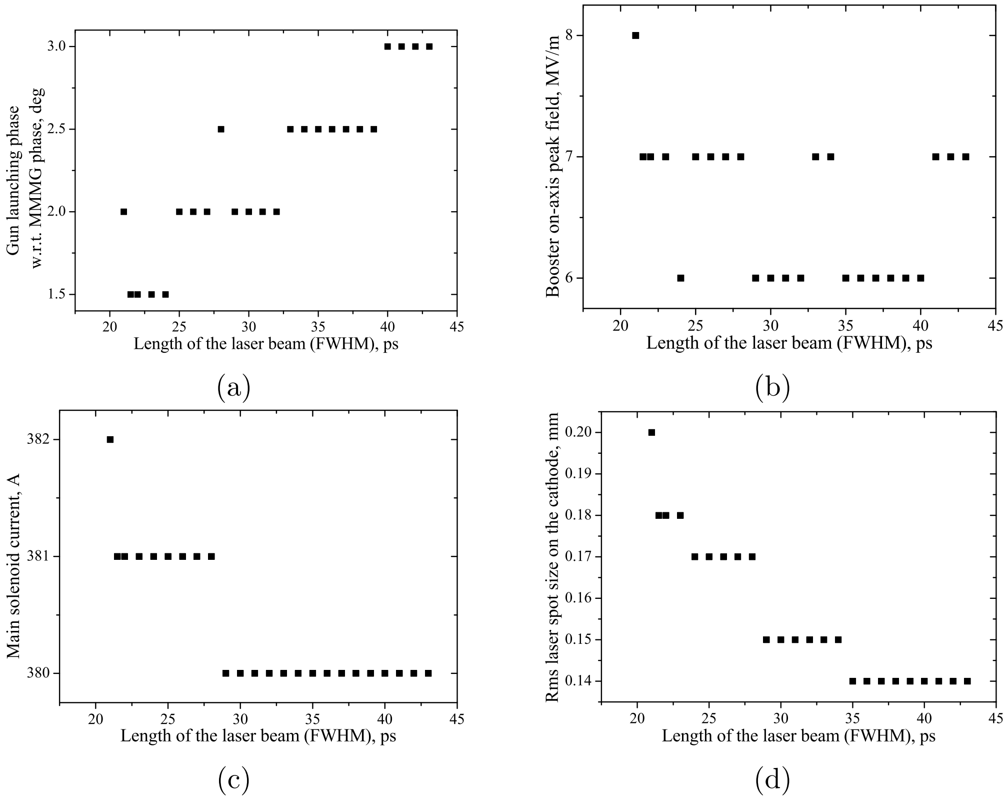

(a) (b)

(c) (d)

Figure A.2: Rms laser spot size, gun launching phase, main solenoid current and booster on-axis peak field, at which minimum emittance values were found, dependencies on the laser pulse length. Electron beam with a charge of 250 pC.

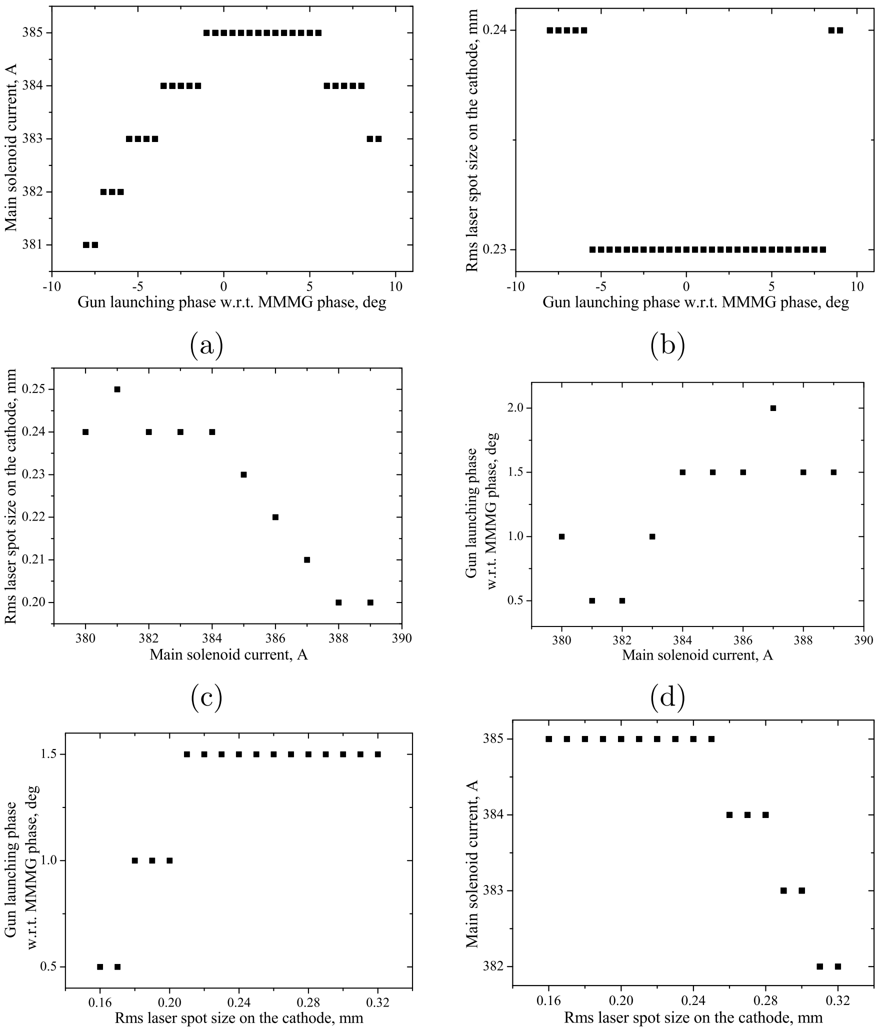

(a) (b)

(c) (d)

(e) (f)

Figure A.3: Dependencies of different parameters on a certain machine parameter delivering the minimum emittance value for the fixed booster on-axis peak field of $E_b^p = 20\,\mathrm{MV/m}$. Each doublet of plots corresponds to a certain plot from Fig. 6.11.

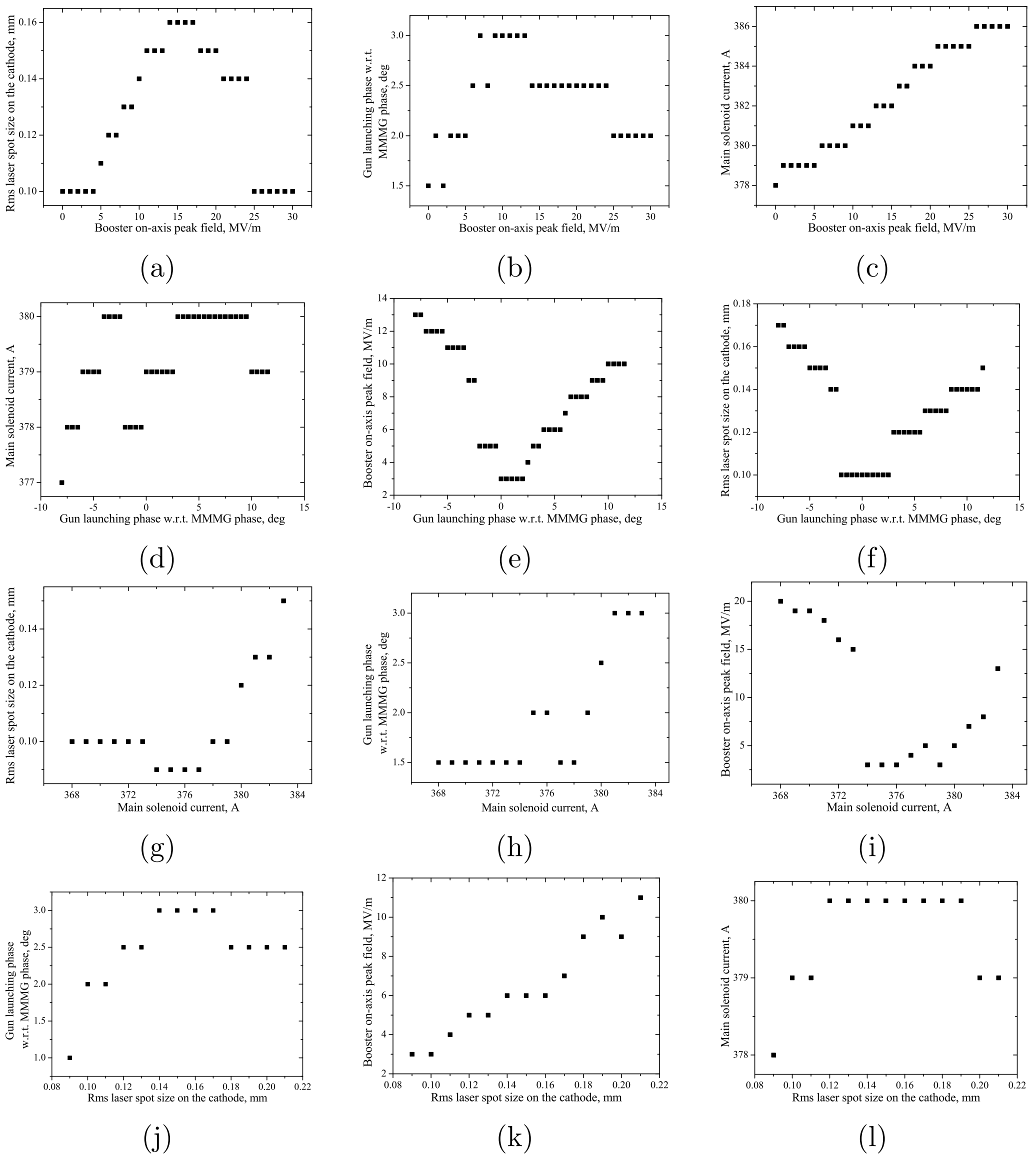

Figure A.4: Dependencies of different parameters on a certain machine parameter delivering the minimum emittance value. Each triplet of plots corresponds to a certain plot from Fig. 6.13.

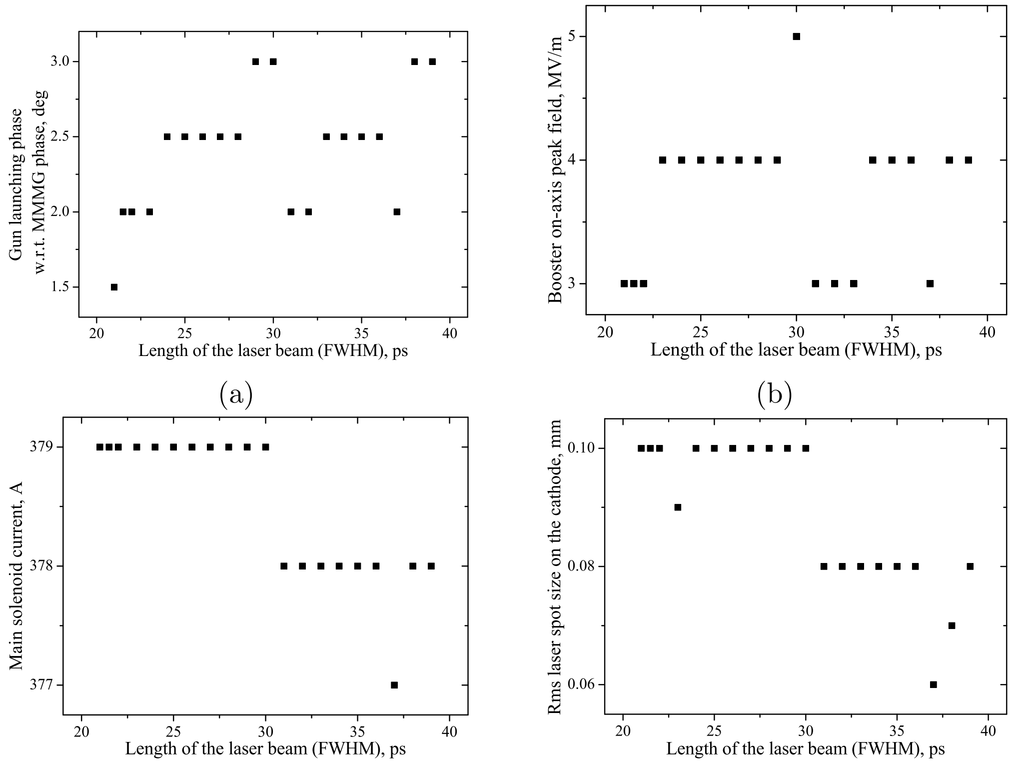

(a) (b)

(c) (d)

Figure A.5: Rms laser spot size, gun launching phase, main solenoid current and booster on-axis peak field, at which minimum emittance values were found, dependencies on the laser pulse length. Electron beam with a charge of 100 pC.

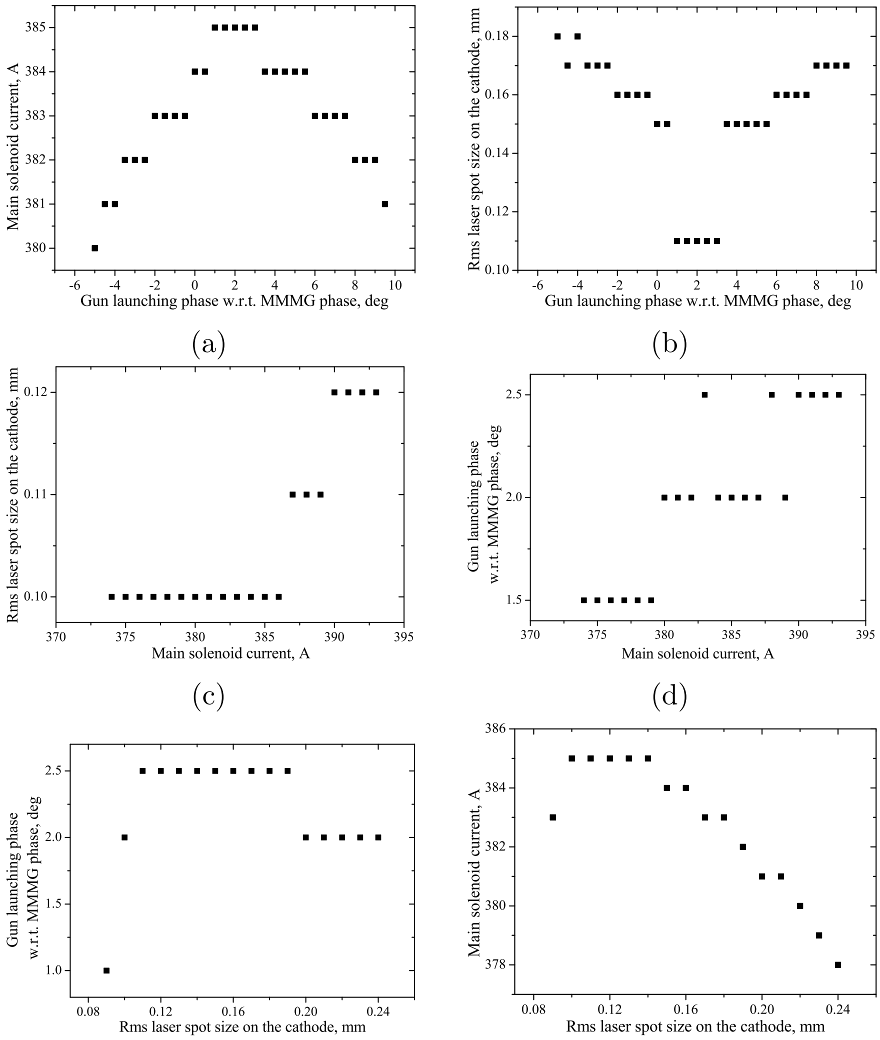

(a) (b)

(c) (d)

(e) (f)

Figure A.6: Dependencies of different parameters on a certain machine parameter delivering the minimum emittance value for the fixed booster on-axis peak field of $E_b^p = 20\,\mathrm{MV/m}$. Each doublet of plots corresponds to a certain plot from Fig. 6.15.

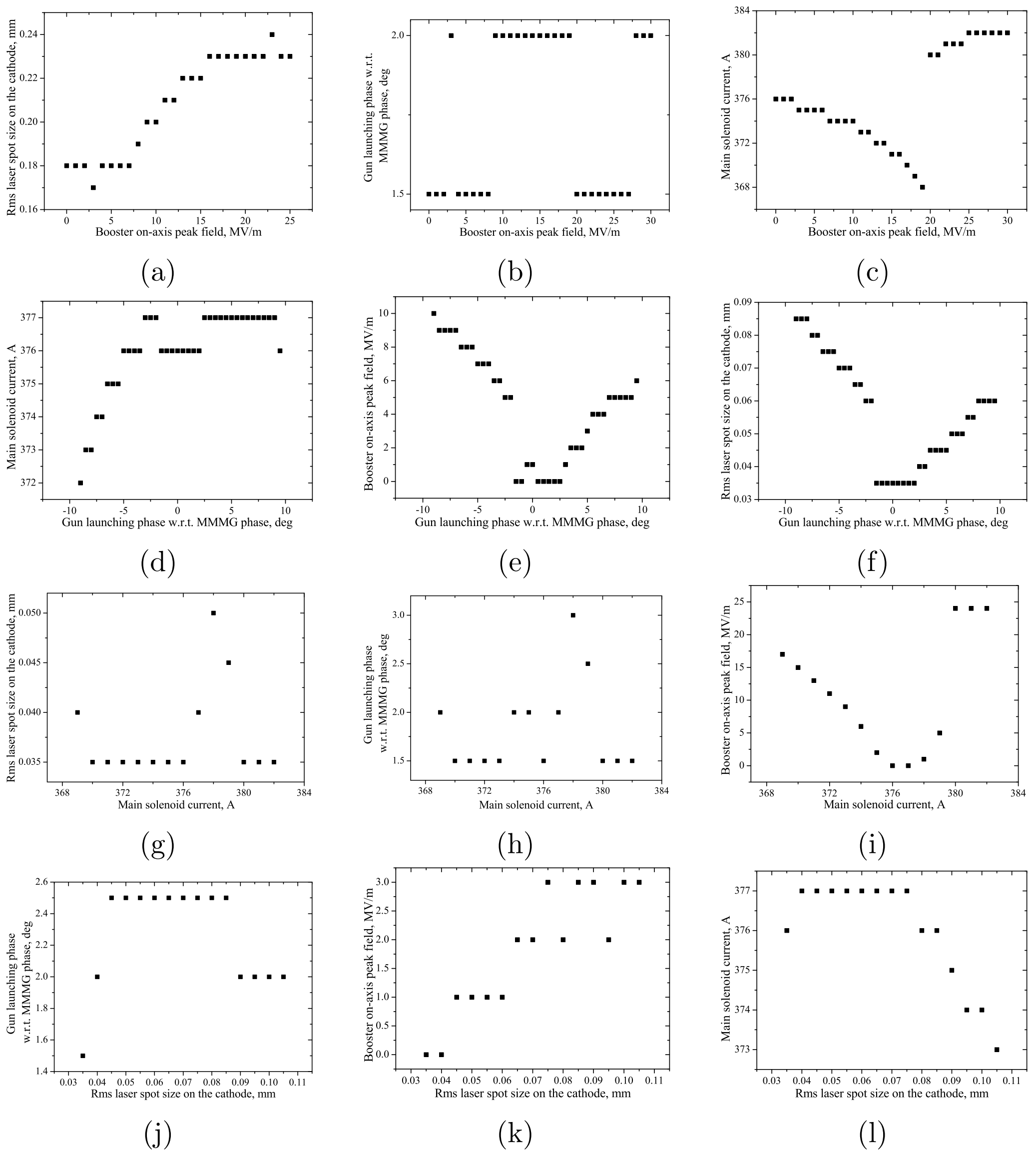

(a) (b) (c)

(d) (e) (f)

(g) (h) (i)

(j) (k) (l)

Figure A.7: Dependencies of different parameters on a certain machine parameter delivering the minimum emittance value. Each triplet of plots corresponds to a certain plot from Fig. 6.17.

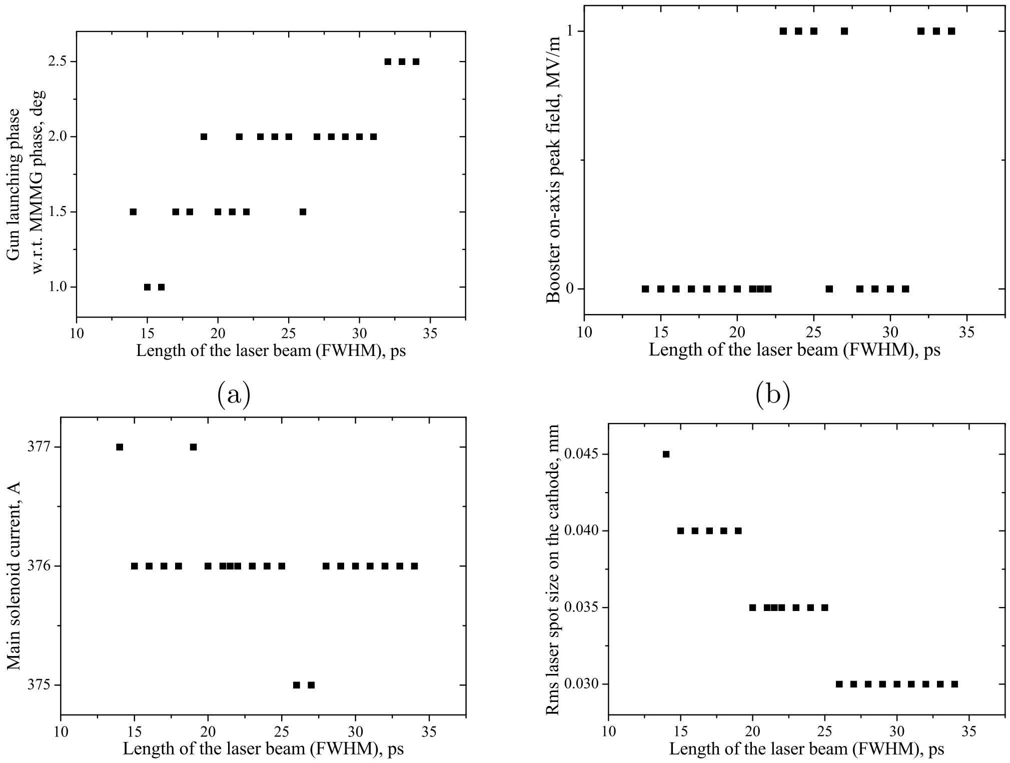

(a) (b)

(c) (d)

Figure A.8: Rms laser spot size, gun launching phase, main solenoid current and booster on-axis peak field, at which minimum emittance values were found, dependencies on the laser pulse length. Electron beam with a charge of 20 pC.

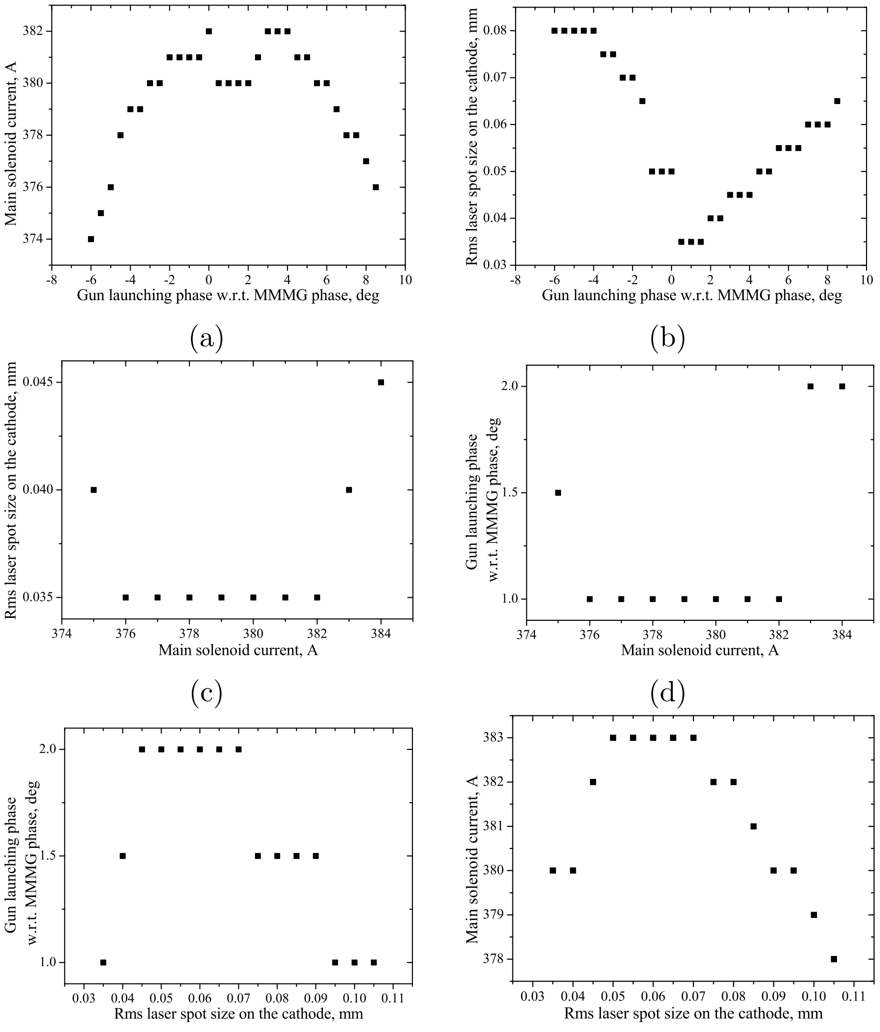

(a) (b)

(c) (d)

(e) (f)

Figure A.9: Dependencies of different parameters on a certain parameter delivering the minimum emittance value for the fixed booster on-axis peak field of $E_b^p = 20\,MV/m$. Each doublet of plots corresponds to a certain plot from Fig. 6.19.

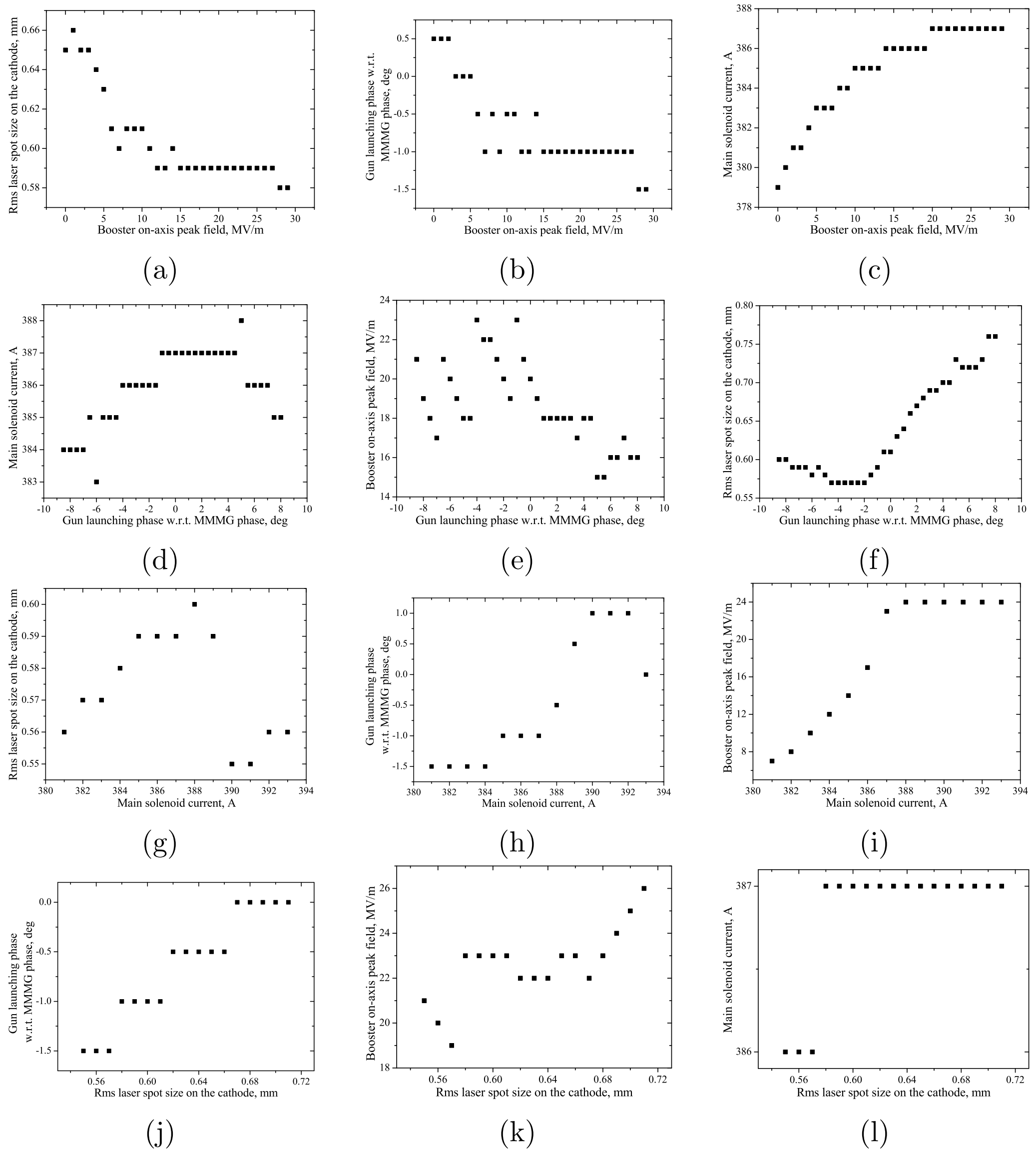

(a) (b) (c)

(d) (e) (f)

(g) (h) (i)

(j) (k) (l)

Figure A.10: Dependencies of different parameters on a certain parameter delivering the minimum emittance value. Each triplet of plots corresponds to a certain plot from Fig. 6.21.

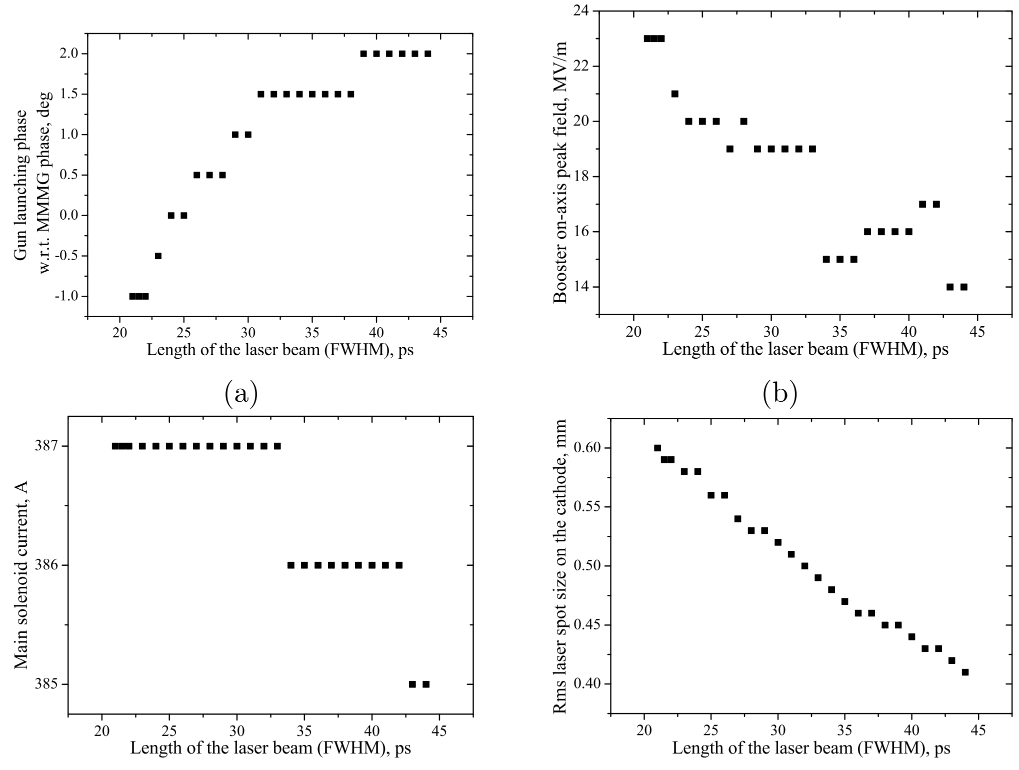

(a) (b)

(c) (d)

Figure A.11: Rms laser spot size, gun launching phase, main solenoid current and booster on-axis peak field, at which minimum emittance values were found, dependencies on the laser pulse length. Electron beam with a charge of 20 pC.

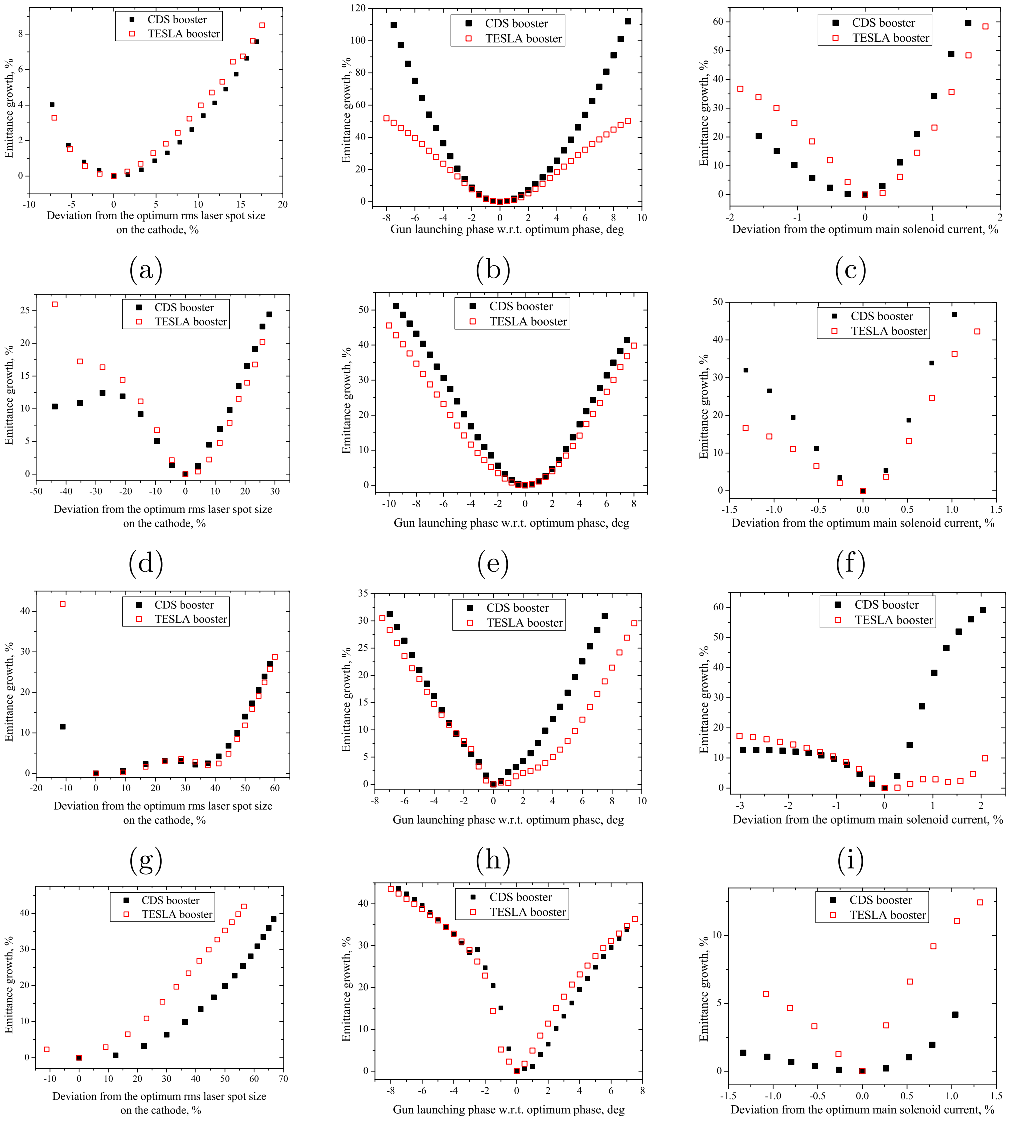

(a) (b) (c)

(d) (e) (f)

(g) (h) (i)

(j) (k) (l)

Figure A.12: Emittance growth as a function of different machine parameters for different types of booster cavities and electron beams with different charges. Each triplet from the top corresponds to electron beams with a charge of 2 nC, 250 pC, 100 pC and 20 pC, respectively.

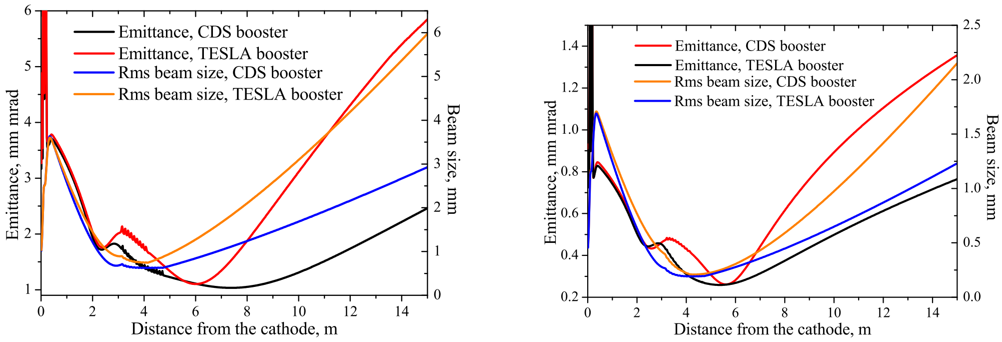

(a) 2 nC.　　(b) 250 pC.

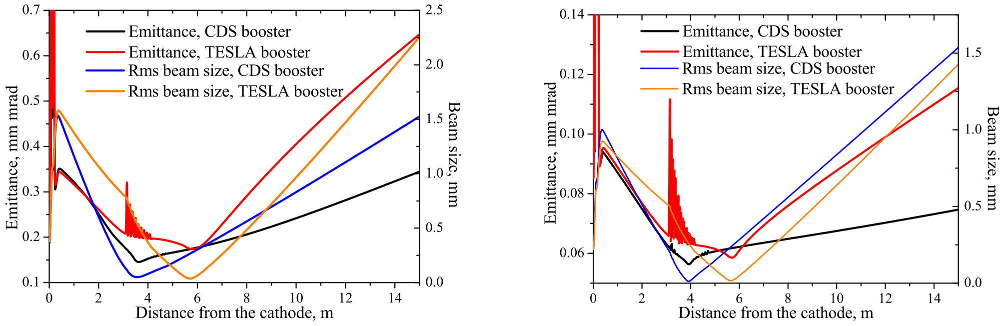

(c) 100 pC.　　(d) 20 pC.

Figure A.13: Emittance evolution along the PITZ beamline for different types of booster cavities and electron beams with different charges.

Appendix B

Core emittance for electron beams with different charges

In the following Fig. B.1 measured and simulated core emittances for electron beams with different charges are presented. For more details see Chapter 7.6

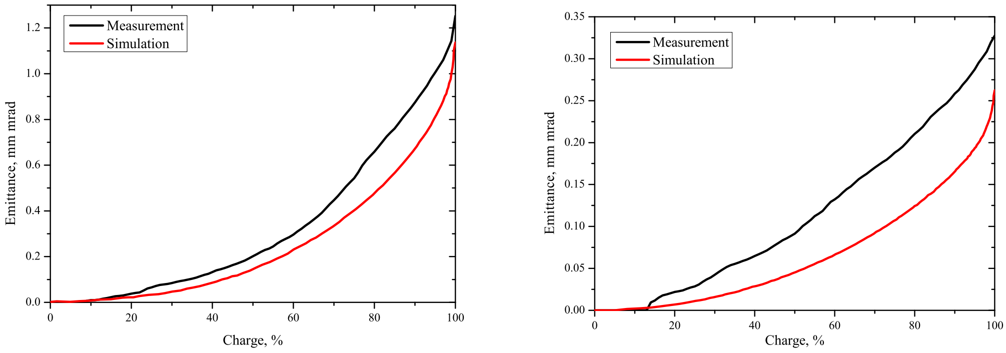

(a) 2 nC. (b) 250 pC.

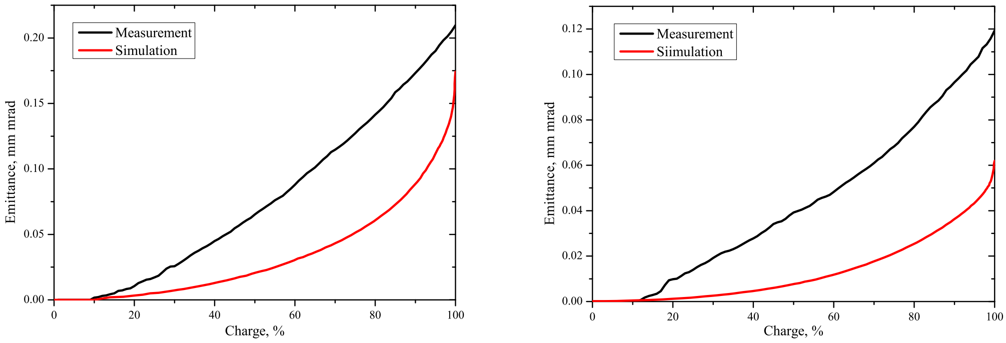

(c) 100 pC. (d) 20 pC.

Figure B.1: Measured and simulated core emittance for electron beams with different charges.

Bibliography

[1] J. M. J. Madey, *Free electron lasers and other advanced sources of light: Scientific Research Opportunities.* National Academy Press, Washington, D.C., 1994.

[2] P. Emma, R. Akre, J. Arthur, R. Bionta, C. Bostedt, J. Bozek, A. Brachmann, P. Bucksbaum, R. Coffee, F. J. Decker, Y. Ding, D. Dowell, S. Edstrom, A. Fisher, J. Frisch, S. Gilevich, J. Hastings, G. Hays, P. Hering, Z. Huang, R. Iverson, H. Loos, M. Messerschmidt, A. Miahnahri, S. Moeller, H. D. Nuhn, G. Pile, D. Ratner, J. Rzepiela, D. Schultz, T. Smith, P. Stefan, H. Tompkins, J. Turner, J. Welch, W. White, J. Wu, G. Yocky, and J. Galayda, "First lasing and operation of an Ångstrom-wavelength free-electron laser," *Nature Photonics*, vol. 4, no. 9, pp. 641–647, 2010.

[3] H. Tanaka, "The SPRING-8 angstrom compact free electron laser (SACLA)," in *Proceedings of IPAC2012, New Orleans, Louisiana, USA*, pp. 2006 – 2010, 2012.

[4] P. Schmüser, M. Dohlus, and J. Rossbach, *Ultraviolet and Soft X-Ray Free-Electron Lasers: Introduction to Physical Principles, Experimental Results, Technological Challenges.* Springer Tracts in Modern Physics, Springer, 1st ed., 2008.

[5] J. Rossbach, E. Saldin, E. Schneidmiller, and M. Yurkov, "Interdependence of parameters of an X-ray FEL," *Nuclear Instruments and Methods in Physics Research Section A: Accelerators, Spectrometers, Detectors and Associated Equipment*, vol. 374, no. 3, pp. 401 – 407, 1996.

[6] V. Miltchev, *Investigations on the transverse phase space at a photo injector for minimized emittance.* PhD thesis, Humboldt-Universität zu Berlin, 2006.

[7] A. Oppelt, K. Abrahamyan, G. Asova, J. Bähr, G. Dimitrov, U. Gensch, H.-J. Grabosch, J. Han, S. Khodyachykh, M. Krasilnikov, S. Liu, V. Miltchev, B. Petrosyan, S. Riemann, L. Staykov, F. Stephan, M. Hartrott, E. Jaeschke, D. Krämer, D. Lipka, F. Marhauser, D. Richter, K. Flöttmann, S. Schreiber, T. Garvey, L. Catani, E. Chiadroni, A. Cianchi, L. Palumbo, D. Alesini, M. Boscolo, G. Pirro, M. Ferrario, D. Filippetto, C. Vicario, P. Michelato, L. Monaco, C. Pagani, D. Sertore, V. Boccone, N. Pavel, V. Paramonov, I. Tsakov, G. Klemz, W. Sandner, I. Will, W. Ackermann, W. Müller, S. Schnepp, T. Weiland, J. Rönsch, and J. Rossbach, "Status and first results from the upgraded PITZ facility," in *Proceedings of FEL2005, Stanford, USA*, 2005.

[8] L. Staykov, *Characterization of the transverse phase space at the photo-injector test facility in DESY, Zeuthen site.* PhD thesis, Universität Hamburg, 2012.

[9] M. Hänel, *Experimental investigations on the influence of the photocathode laser pulse parameters on the electron bunch quality in an RF - photoelectron source.* PhD thesis, Universität Hamburg, 2010.

[10] I. Will, G. Koss, and I. Templin, "The upgraded photocathode laser of the TESLA Test Facility," *Nuclear Instruments and Methods in Physics Research Section A: Accelerators, Spectrometers, Detectors and Associated Equipment*, vol. 541, no. 3, pp. 467 – 477, 2005.

[11] P. Piot, M. Ferrario, K. Flöttmann, B. Grigoryan, and T. Limberg, "Conceptual design of the xfel photoinjector," tech. rep., Dt. Elektronen-Synchrotron DESY, MHF-SL Group, 2001.

[12] I. Will and G. Klemz, "Generation of flat-top picosecond pulses by coherent pulse stacking in a multicrystal birefringent filter," *Optics Express*, vol. 16, pp. 14922–14937, Sep 2008.

[13] http://jp.hamamatsu.com. Hamamatsu Photonics C5680 streak camera.

[14] R. Boyd, *Nonlinear optics.* Electronics & Electrical, Academic Press, 2003.

[15] J. Rönsch, *Investigations on the electron bunch distribution in the longitudinal phase space at a laser driven RF electron source for the European X-FEL.* PhD thesis, Universität Hamburg, 2009.

[16] http://www.thalesgroup.com. THALES 10 MW multibeam klystron TH1801-MBK.

[17] http://www.toshiba-tetd.co.jp/eng/electron/e_kly.htm. Toshiba E3736 10 MW multibeam klystron.

[18] M. Krasilnikov, G. Asova, H.-J. Grabosch, M. Gross, L. Hakobyan, I. Isaev, Y. Ivanisenko, M. Khojoyan, G. Klemz, W. Koehler, M. Mahgoub, D. Malyutin, M. Nozdrin, A. Oppelt, M. Otevrel, B. Petrosyan, S. Rimjaem, A. Shapovalov, F. Stephan, G. Vashchenko, S. Weidinger, R. Wenndorff, M. Hoffmann, H. Schlarb, I. Templin, I. Will, and D.Richter, "High brightness photo injector upgrade and experimental optimization at PITZ," in *Proceedings of IPAC2011, San Sebastian, Spain*, pp. 3152 – 3154, 2011.

[19] I. Isaev, G.Asova, H. Grabosch, M. Gross, L. Hakobyan, Y. Ivanisenko, M. Khojoyan, G. Klemz, W. Koehler, M. Krasilnikov, M. Mahgoub, D. Malyutin, A. Oppelt, M. Otevrel, B. Petrosyan, S. Rimjaem, A. Shapovalov, F. Stephan, G. Vashchenko, S. Weidinger, R. Wenndorff, M. Hoffmann, H. Schlarb, I. Templin, I. Will, and D. Richter, "RF photo gun stability measurement at PITZ," in *Proceedings of IPAC2011, San Sebastian, Spain*, pp. 442 – 444, 2011.

[20] P. Michelato, C. Gesmundo, and D. Sertore, "High quantum efficiency photocathode preparation system for TTF injector II," tech. rep., Dt. Elektronen-Synchrotron DESY, MHF-SL Group, 1999.

[21] http://www.bergoz.com. ICT-178-2-XXX-X.

[22] Y. Ivanisenko, *Investigation of Slice Emittance Using an Energy-chirped Electron Beam in a Dispersive Section for Photo Injector Characterization at PITZ.* PhD thesis, Universität Hamburg, 2012.

[23] D. Malyutin, M. Krassilnikov, J. Meissner, F. Stephan, G. Vashchenko, K. Kusoljariyakul, and S. Rimjaem, "Commissioning of new diagnostic devices at PITZ," in *Proceedings of RUPAC2012, Saint-Petersburg, Russia*, 2012.

[24] V. Ginzburg and V. Tsytovich, *Transition radiation and transition scattering.* Adam Hilger series on plasma physics, A. Hilger, 1990.

[25] G. Asova, *Tomography of the electron beam transverse phase space at PITZ.* PhD thesis, INRNE, Bulgarian Academy of Sciences, Sofia, 2011.

[26] W. E. Spicer, "Photoemissive, Photoconductive, and Optical Absorption Studies of Alkali-Antimony Compounds," *Phys. Rev.*, vol. 112, pp. 114–122, Oct 1958.

[27] C. N. Berglund and W. E. Spicer, "Photoemission Studies of Copper and Silver: Theory," *Phys. Rev.*, vol. 136, pp. A1030–A1044, Nov 1964.

[28] A. Sommer and W. Spicer, *Photoelectronic materials and devices.* Van Nostrand, Princeton, NJ, 1965.

[29] R. A. Powell, W. E. Spicer, G. B. Fisher, and P. Gregory, "Photoemission studies of cesium telluride," *Physical Review B*, vol. 8, pp. 3987–3995, Oct 1973.

[30] M. Reiser, *Theory and design of charged particle beams.* Wiley series in beam physics and accelerator technology, Wiley, 1994.

[31] P. Lapostolle, "Possible emittance increase through filamentation due to space charge in continuous beams," *IEEE Transactions on Nuclear Science*, vol. 18, no. 3, pp. 1101–1104, 1971.

[32] F. J. Sacherer, "Rms envelope equations with space charge," *IEEE Transactions on Nuclear Science*, vol. 18, no. 3, pp. 1105–1107, 1971.

[33] B. Carlsten, "New photoelectric injector design for the Los Alamos National Laboratory XUV FEL accelerator," *Nuclear Instruments and Methods in Physics Research Section A: Accelerators, Spectrometers, Detectors and Associated Equipment*, vol. 285, no. 12, pp. 313 – 319, 1989.

[34] K.-J. Kim, "Rf and space-charge effects in laser-driven rf electron guns," *Nuclear Instruments and Methods in Physics Research Section A: Accelerators, Spectrometers, Detectors and Associated Equipment*, vol. 275, no. 2, pp. 201 – 218, 1989.

[35] M. Krasilnikov, F. Stephan, G. Asova, H.-J. Grabosch, M. Groß, L. Hakobyan, I. Isaev, Y. Ivanisenko, L. Jachmann, M. Khojoyan, G. Klemz, W. Köhler, M. Mahgoub, D. Malyutin, M. Nozdrin, A. Oppelt, M. Otevrel, B. Petrosyan, S. Rimjaem, A. Shapovalov, G. Vashchenko, S. Weidinger, R. Wenndorff, K. Flöttmann, M. Hoffmann, S. Lederer, H. Schlarb, S. Schreiber, I. Templin, I. Will, V. Paramonov, and D. Richter, "Experimentally minimized beam emittance from an L-band photoinjector," *Physical Review Special Topics - Accelerators and Beams*, vol. 15, p. 100701, Oct 2012.

[36] http://www.desy.de/∼mpyflo. A Space charge TRacking Algorithm (ASTRA).

[37] V. Miltchev, "Construction and commissioning of a Transverse Emittance Measurement System for the Photoinjector Test facility at DESY Zeuthen," Master's thesis, Humboldt-Universität zu Berlin, 2002.

[38] F. Stephan, I. Bohnet, J. Bähr, U. Gensch, H. J. Grabosch, D. Lipka, A. Oppelt, R. Bakker, E. Jaeschke, D. Krämer, M. Hartrott, Z. Li, J. P. Carneiro, K. Flöttmann, P. Piot, J. Rossbach, S. Schreiber, V. Dzhordzhadze, P. Michelato, C. Pagani, D. Sertore, V. Miltchev, I. Tsakov, A. Liero, H. Redlin, W. Sandner, R. Schumann, I. Will, R. Cee, M. Krassilnikov, S. Setzer, T. Weiland, K. Abrahamyan, and B. Petrosian, "First measurements at the Photo Injector Test Facility at DESY Zeuthen," in *Proceedings of EPAC2002, Paris, France*, 2002.

[39] http://www.alliedvisiontec.com/emea/products/cameras/gigabit-ethernet/prosilica-gc/gc1350.html. Prosilica GC-1350 CCD camera.

[40] M. Altarelli, R. Brinkmann, M. Chergui, W. Decking, B. Dobson, *et al.*, "XFEL: The European X-Ray Free-Electron Laser. Technical design report," tech. rep., 2006.

[41] S. Schreiber, M. Gross, C. Grün, O. Hensler, G. Klemz, K. Klose, G. Koss, S. Schulz, T. Schulz, M. Staack, I. Will, I. Templin, and H. Willert, "Upgrades of the photoinjector laser system at FLASH," in *Proceedings of FEL2012, Nara, Japan*, 2012.

[42] https://portal.slac.stanford.edu/sites/lcls_public. Linac Coherent Light Source (LCLS).

[43] S. Rimjaem, F. Stephan, M. Krasilnikov, W. Ackermann, G. Asova, J. Bähr, E. Gjonaj, H. Grabosch, L. Hakobyan, M. Hänel, Y. Ivanisenko, M. Khojoyan, G. Klemz, S. Lederer, M. Mahgoub, P. Michelato, L. Monaco, M. Nozdrin, B. O'Shea, M. Otevrel, B. Petrosyan, D. Richter, J. Rönsch-Schulenburg, D. Sertore, S. Schreiber, S. Schnepp, A. Shapovalov, R. Spesyvtsev, L. Staykov, G. Vashchenko, T. Weiland, and I. Will, "Optimizations of transverse projected emittance at the photo-injector test facility at DESY, location Zeuthen," *Nuclear Instruments and Methods in Physics Research Section A: Accelerators, Spectrometers, Detectors and Associated Equipment*, vol. 671, no. 0, pp. 62 – 75, 2012.

[44] W. Schottky, "Über kalte und warme Elektronenentladungen," *Zeitschrift für Physik*, vol. 14, pp. 63 – 106, 1923.

[45] J. Li, G. Asova, I. Isaev, M. Gross, L. Hakobyan, Y. Ivanisenko, M. Khojoyan, G. Klemz, G. Kourkafas, M. Krasilnikov, K. Kusoljariyakul, M. Mahgoub, D. Malyutin, B. Marchetti, A. Oppelt, B. Petrosyan, S. Rimjaem, A. Shapovalov, F. Stephan, G. Vashchenko, G. Feng, L. Shang, and D. Richter, "Emission studies of photocathode rf gun at PITZ," in *Proceedings of ICAP2012, Rostock-Warnemünde, Germany*, 2012.

[46] J. Frisch, R. Akre, J. Arthur, C. Bostedt, J. Bozek, A. Brachmann, P. Bucksbaum, R. Coffee, F.-J. Decker, Y. Ding, D. Dowell, S. Edstrom, P. Emma, A. Fisher, J. Galayda, A. Gilevich, J. Hastings, G. Hays, P. Hering, Z. Huang, R. Iverson, H. Loos, M. Messerschmidt, A. Miahnahri, S. Moeller, H.-D. Nuhn, D. Ratner, J. Rzepiela, D. Schultz, T. Smith, H. Tompkins, J. Turner, J. Welch, J. Wu, G. Yocky, R. Bionta, and G. Pile, "Operation and upgrades of the LCLS," in *Proceedings of LINAC2010, Tsukuba, Japan*, 2010.

[47] P. Emma, A. Brachmann, and D. Dowell, "Beam brightness measurements in the LCLS injector," in *Mini-workshop on compact X-ray FELs using high-brightness beams*, 2010.

[48] K. Togawa, "Low-emittance Electron Gun for X-ray Free Electron Laser at SPring-8," *Journal of the Vacuum Society of Japan*, vol. 55, pp. 73–77, 2012.

[49] M. Ferrario, D. Alesini, M. Bellaveglia, S. Bertolucci, R. Boni, M. Boscolo, M. Castellano, A. Clozza, L. Cultrera, G. Pirro, A. Drago, A. Esposito, D. Filippetto, V. Fusco, A. Gallo, G. Gatti, A. Ghigo, M. Incurvati, C. Ligi, M. Migliorati, A. Mostacci, E. Pace, L. Palumbo, L. Pellegrino, R. Ricci, C. Sanelli, M. Serio, F. Sgamma, B. Spataro, F. Tazzioli, S. Tomassini, C. Vaccarezza, M. Vescovi, C. Vicario, A. Bacci, S. Cialdi, A. Rossi, L. Serafini, L. Catani, E. Chiadroni, A. Cianchi, A. Cook, M. Dunning, P. Frigola, J. Rosenzweig, L. Giannessi, M. Quattromini, C. Ronsivalle, P. Musumeci, and M. Petrarca, "Experimental results with the SPARC emittance-meter," in *Proceedings of PAC2007, Albuquerque, New Mexico, USA*, 2007.

[50] L. Young and J. Billen, "The particle tracking code PARMELA," in *Proceedings of PAC2003, Portland, Oregon, USA*, 2003.

[51] M. de Loos and S. van der Geer, "General Particle Tracer: A new 3D code for accelerator and beamline design," in *Proceedings of EPAC96, Sitges, Spain*, 1996.

[52] W. Decking and T. Limberg, "European XFEL Post-TDR Description," tech. rep., European XFEL, 2013.

Acknowledgements

I would like to express my sincerest gratitude to all people who have contributed to the success of this work:

- **Prof. Dr. J. Roßbach and Dr. F. Stephan** for supervising this work.
- **Prof. Dr. J. Roßbach, Dr. F. Stephan, Dr. M. Krasilnikov, Dr. M. Groß, Dr. M. Otevrel and Dr. B. Marchetti** for thoroughly proofreading of my thesis, for their useful comments, suggestions and advices.
- **Dr. G. Asova, Dr. Y. Ivanisenko** for the helpful discussions of the issues related to this work.
- **shift staff, technical staff and IT department of DESY in Zeuthen** for doing their best for the experiments.
- **my family, Nikita and Maryna Vashchenko**, who supported me strongly during the time of performing this thesis.